SÃO PAULO STATE UNIVERTITY (UNESP)
SCHOOL OF ENGINEERING, ILHA SOLTEIRA
DEPARTMENT OF PHYSICS AND CHEMISTRY
POSTGRADUATION PROGRAM IN MATERIALS SCIENCE

MARCO ANTONIO DE MELLO TEIXEIRA

Influence of crystallization temperature on physical and chemical properties of $BiFeO_3$ thin films

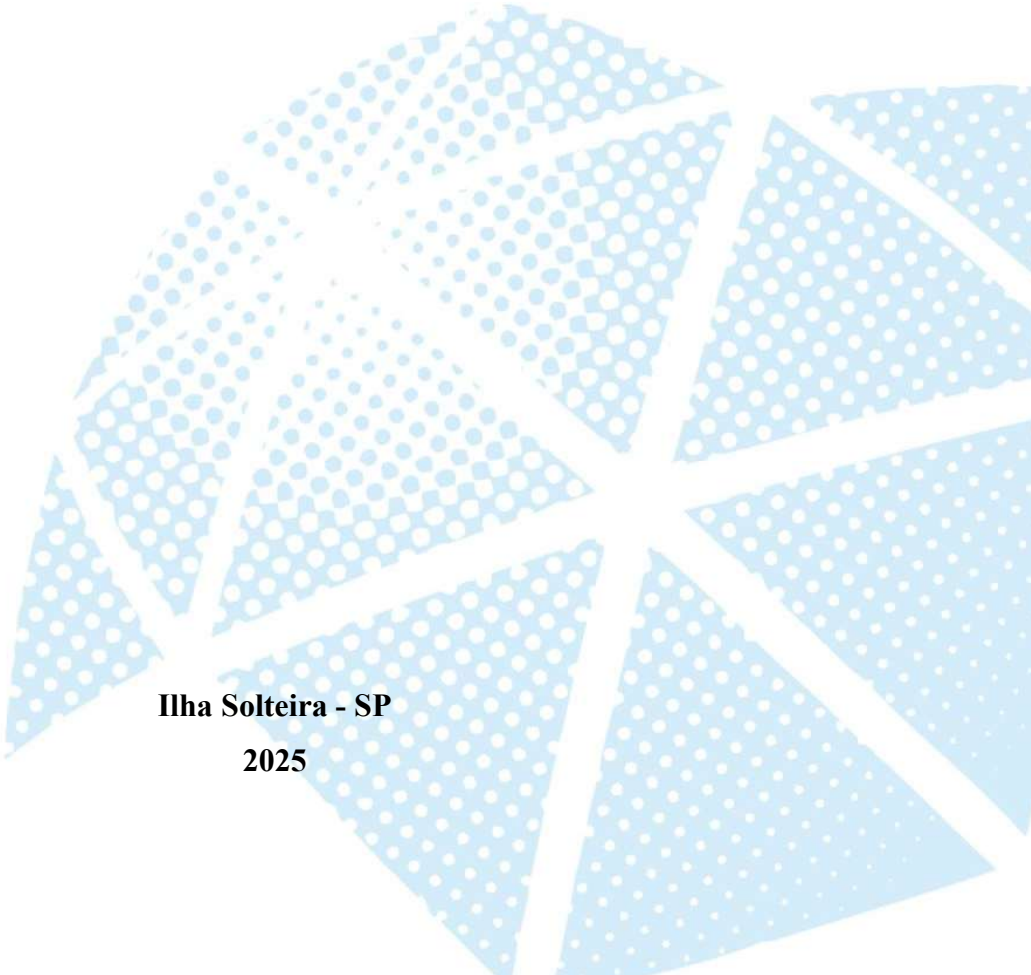

Ilha Solteira - SP
2025

Marco Antonio de Mello Teixeira

Influence of crystallization temperature on physical and chemical properties of $BiFeO_3$ thin films

Dissertation submitted to the Postgraduation Program in Materials Science of São Paulo University (UNESP) School of Engineering, Ilha Solteira, as a partial requirement to obtain Master Degree in Materials Science.
Concentration area: Physics of Condensed Matter.

Supervisor: Prof. Dr. Eudes Borges de Araújo

Ilha Solteira - SP
2025

FICHA CATALOGRÁFICA
Desenvolvido pelo Serviço Técnico de Biblioteca e Documentação

T266i

Teixeira, Marco Antono de Mello.
Influence of crystallization temperature on physical and chemical properties of BIFeO3 thin films / Marco Antono de Mello Teixeira. -- Ilha Solteira: [s.n.], 2024
99 f. : il.

Dissertação (mestrado) - Universidade Estadual Paulista. Faculdade de Engenharia de Ilha Solteira. Área de conhecimento: Física da Matéria Condensada, 2025

Orientador: Eudes Borges de Araújo

Inclui bibliografia

1. Ferrita de bismuto. 2. Temperatura de cristalização. 3. Defeitos. 4. Filmes finos.

Amanda Sertori dos Santos
Bibliotecária - CRB/8-9061
Seção Técnica de Referência, Atendimento ao Usuário e Documentação
Diretoria Técnica de Biblioteca e Documentação

UNIVERSIDADE ESTADUAL PAULISTA

Câmpus de Ilha Solteira

CERTIFICADO DE APROVAÇÃO

TÍTULO DA DISSERTAÇÃO: Influence of crystallization temperature on physical and chemical properties of BiFeO3 thin films

AUTOR: MARCO ANTONIO DE MELLO TEIXEIRA
ORIENTADOR: EUDES BORGES DE ARAUJO

Aprovado como parte das exigências para obtenção do Título de Mestre em Ciência dos Materiais, área: Física da Matéria Condensada pela Comissão Examinadora:

Prof. Dr. EUDES BORGES DE ARAUJO (Participaçao Presencial)
Departamento de Fisica e Quimica / Faculdade de Engenharia de Ilha Solteira - UNESP

gov.br Documento assinado digitalmente
ANTONIO SERGIO BEZERRA SOMBRA
Data: 25/02/2025 12:48:28-0300
Verifique em https://validar.iti.gov.br

Prof. Dr. ANTONIO SERGIO BEZERRA SOMBRA (Participaçao Virtual)
Departamento de Física / Universidade Federal do Ceará - UFC

Vladimir Shvartsman
Digital unterschrieben von Vladimir Shvartsman
Datum: 2025.02.25 20:03:23 +01'00'

Prof. Dr. VLADIMIR SHVARTSMAN (Participaçao Virtual)
Institute for Materials Science / University of Duisburg-Essen (Alemanha)

Ilha Solteira, 25 de fevereiro de 2025

CamScanner

Relevância cientifico-social

A ferrita de bismuto tem sido considerada nos últimos 60 anos um material promissor para novos dispositivos eletrônicos e microeletrônicos, células solares, sensores e atuadores, processamento de fotocatálise, etc. A persistência e resiliência da comunidade científica ao longo dos anos no estudo deste material é um reflexo de quão importante é ser integrado na aplicação tecnológica para manter e melhorar o padrão de vida da humanidade moderna. Para desvendar nossa relevância e impactos sobre o científico, social, ambiental etc., baseamos nossa pesquisa nos ODS (Objetivos de Desenvolvimento Sustentável) das Nações Unidas.

A meta número 7 declara "Garantir acesso à energia acessível, confiável, sustentável e moderna para todos"; meta número 9 "Construir infraestrutura resiliente, promover industrialização inclusiva e sustentável e fomentar inovação"; e meta número 13 "Tomar medidas urgentes para combater as mudanças climáticas e seu impacto regulando as emissões e promovendo desenvolvimentos em energia renovável" [1].

Durante este manuscrito, discutimos sobre as propriedades elétricas e ópticas do $BiFeO_3$ e, devido a essas propriedades, a meta número 7 é a meta que mais se encaixa em nosso trabalho. A tecnologia fotovoltaica, em células solares que convertem energia solar em eletricidade, é talvez a energia mais ecológica em comparação às outras: hidrelétrica, nuclear, carvão, gás natural etc. No entanto, a energia solar corresponde a apenas 1% da geração global de eletricidade. No contexto da sustentabilidade, considerando o cenário mundial atual, é sem dúvida necessário que a humanidade se concentre e aprimore a geração, fonte e conversão de energia por meio da tecnologia fotovoltaica.

A última afirmação requer fomentar a inovação e a integração da tecnologia renovável na infraestrutura moderna. Para executar essas ações é de suma importância compreender a física fundamental por trás do material do candidato e do protagonista, entender suas questões de aplicação prática e incentivar ideias para resolver ou contornar obstáculos, o que nos levará ao objetivo número 9. Então, uma vez cooperando e alcançando os objetivos 7 e 9, obviamente em qualquer estágio, levará ao objetivo 13.

Scientific-social relevance

Bismuth ferrite has been considered over the last 60 years a promising material to new electronic and microelectronic devices, solar cells, sensor and actuator, photocatalysis processing, among others. The persistence and resilience of scientific community throughout years in studying this material is a reflex of how much important it is to be integrated in technological application to keep and improve the standard of living of modern humanity. To unravel our relevance and impacts over the scientific, social, environmental etc, we based our research on the SDGs (Sustainable Development Goals) of the United Nations.

The goal number 7 declares "Ensure access to affordable, reliable, sustainable and modern energy for all"; goal number 9 "Build resilient infrastructure, promote inclusive and sustainable industrialization, and foster innovation"; and goal number 13 "Take urgent action to combat climate change and its impact by regulating emissions and promoting developments in renewable energy" [1].

During this manuscript, we have discussed several times about the electric and optical properties of $BiFeO_3$ and, due to these properties, goal number 7 is the goal that mostly fits in our work. The photovoltaic technology, in solar cells which converts solar energy into electricity, is perhaps the most eco-friendly energy in comparison to the others: hydroelectric, nuclear, coal, natural gas etc. However, solar energy corresponds only 1% of global electricity generation. In context of sustainability considering the current world scenario, it is undoubtedly necessary of humanity focus and enhance the generation, source and conversion of energy through photovoltaic technology.

The last affirmation requires foster innovation and integration of renewable technology in modern infrastructure. Aiming to execute these actions is of utmost importance comprehend and fundamental physics behind the candidate and protagonist material, understand its practical application issues and encourage ideas to resolve or circumvent obstacles, on what take us to goal number 9. So, once cooperating and achieving goals 7 and 9, obviously at any stage, will lead to goal 13.

Acknowledgements

I would like to begin by expressing my heartfelt gratitude to my advisor, Prof. Dr. Eudes Borges de Araújo, for his invaluable guidance, teachings, and patience throughout the research development process.

I extend my thanks to Prof. Dr. Fernando B. Minussi, Prof. Dr. Saulo P. dos Reis and Me. Sobhan M. Fathabad for their insightful discussions on the research, data, and physical interpretations, as well as for sharing their academic expertise with me.

To my colleagues in the Postgraduate Program, Prof. Me. Edimar A. S. Duran, Alfonso E. P. Arrieta, Me. André C. Paula (Superconductivity and Advanced Materials Group, GSMA), Me. Luis F. M. Cesar (Glass and Ceramics Group), Taísa M. H. Nagano, Profa. Rafaela C. O. Santos (Ferroelectrics Group), and Prof. Gabriel M. C. Meira (Atomisa and Strongly Correlated Systems Group, SCSG): your friendship, academic discussions, and support have been instrumental in my growth. You made the environment both intellectually stimulating and welcoming during these two years.

To my friends at UNESP and beyond—Vinicius C. M. de Carvalho, Heloisa Mazzer (Civil Engineering), and João O. B. Taino (Agricultural Engineering)—thank you for your companionship and encouragement.

I am deeply grateful to my family: Antônio M. C. Teixeira (father), Claudileni L. Mello (mother), and Eliana P. Pinhata.

To the esteemed collaborators of the Ferroelectric Group—Prof. Dr. Vladimir Shvartsman (Universität Duisburg-Essen, Germany), Prof. Dr. José A. Eiras (Federal University of São Carlos), Dr. Andrei Kholkin (University of Aveiro, Portugal), and Prof. Dr. Vladimir Ya Shur (Ural Federal University, Russia)—your experimental and intellectual contributions were pivotal to this work.

A special thanks to the employees and staff of the Department of Physics and Chemistry, particularly Élton J. Souza, for his dedication in conducting characterizations such as Scanning Electron Microscopy and Atomic Force Microscopy.

Finally, I express my gratitude to the funding agencies CAPES and CNPq for their financial support, as well as to São Paulo State University (UNESP).

"Nothing in life is to be feared, it is only to be understood. Now is the time to understand more, so that we may fear less." - (Marie Curie)

RESUMO

O objetivo deste estudo é estabelecer protocolos de síntese para filmes finos de ferrita de bismuto, com foco particular na temperatura de cristalização, e avaliar a influência destes protocolos nas propriedades finais dos filmes. Foi identificada uma correlação direta entre as temperaturas de cristalização selecionadas e a formação de vários tipos e concentrações de defeitos, que, por sua vez, modulam essas propriedades. Nossos resultados indicam que, dentro da faixa de temperatura estudada, 600 °C é a temperatura de cristalização ideal para obter filmes com defeitos minimizados e propriedades funcionais aprimoradas. A amostra cristalizada nessa temperatura exibiu uma redução significativa nos defeitos pontuais - livres e complexos - e fases secundárias, levando a um desempenho superior em comparação com as outras amostras. Especificamente, esta amostra demonstrou os menores valores de condutividade elétrica e corrente de fuga, o maior aumento percentual na condutividade elétrica e corrente sob iluminação de luz verde, e os maiores valores de polarização elétrica.

Keywords: Ferrita de Bismuto, Temperatura de Cristalização, Defeitos, Filmes Finos.

ABSTRACT

The objective of this study is to establish synthesis protocols for bismuth ferrite thin films, with a particular focus on crystallization temperature, and to evaluate the influence of these protocols on the final properties of the films. A direct correlation was identified between the selected crystallization temperatures and the formation of various types and concentrations of defects, which, in turn, modulate these properties. Our findings indicate that, within the studied temperature range, 600 °C is the ideal crystallization temperature for obtaining films with minimized defects and enhanced functional properties. The sample crystallized at this temperature exhibited a significant reduction in point -free and complex - and secondary phase defects, leading to superior performance compared to the other samples. Specifically, this sample demonstrated the lowest electrical conductivity and leakage current values, the highest percentage increase in electrical conductivity and current under green light illumination, and the highest electrical polarization values.

Keywords: Bismuth Ferrite, Crystallization Temperature, Defects, Thin Films.

Contents

1 Introduction **13**

1.1 Overview and Motivations 13

1.2 Bismuth Ferrite 16

1.2.1 Characteristics and properties 16

1.2.2 Problem in working with Bismuth ferrite 17

1.3 Goals 19

2 Materials and method **21**

2.1 Synthesis 21

2.2 Structural characterizations 24

2.2.1 X-ray Diffraction (XRD) 24

2.2.2 Raman Scattering Spectroscopy (RSS) 25

2.2.3 X-ray Photoelectron Spectroscopy (XPS) 27

2.2.4 Scanning Electron Spectroscopy (SEM) 27

2.3 Electric characterizations 28

2.3.1 Preparation of samples 28

2.3.2 Complex Impedance Spectroscopy (IS) 29

2.3.3 Leakage Current Density Analysis (LC) 32

2.3.4 Piezoresponse Force Microscopy (PFM) 35

2.4 Optical characterizations 38

3 Results and discussions **39**

3.1 Structural characterizations 39

3.2 X-ray photoelectron spectroscopy analysis 45

3.3 Microscopy analysis 48

3.4 Growth kinetics 49

3.5 Dielectric characterization 55
3.6 Leakage Current Density 65
3.7 Ultraviolet-Visible Spectroscopy 69
3.8 Piezoresponse Force Microscopy 71

4 Conclusions **75**

Bibliography **76**

A Raman spectroscopy's attachments **88**

B SEM's attachments **90**

C Kinetic reaction studies' attachments **91**

D Impedance Spectroscopy's attachments **92**

E J-E studies' attachments **98**

F PFM's attachments **101**

Chapter 1

Introduction

1.1 Overview and Motivations

The history of humanity is often defined by the materials that shaped each era, such as the Bronze Age, Iron Age, and Silicon Age, underscoring how materials influence the standard of living. Semiconductor devices, which underpin modern microelectronics, are central to today's advanced technologies and lifestyles. Despite the remarkable progress of silicon technology, inherent limitations tied to the atomic structure of silicon-based materials suggest the need for alternative approaches. These challenges are driven by the demand for smaller, faster, and more energy-efficient devices to sustain and enhance modern living standards.

Among the emerging materials that address these challenges are multiferroic materials, which exhibit at least two ferroic orders simultaneously within the same phase, enabling coupling between them [2, 3]. A ferroic order refers to a material property that allows switchable internal alignment. For example, in ferromagnetic materials, electron spins can be aligned by a magnetic field; in ferroelectric materials, dipole moments can be aligned by an electric field; and in ferroelastic materials, stress can be reoriented by an applied mechanical field [4]. Figure 1.1 illustrates the switching and coupling mechanisms in a typical multiferroic material. The yellow region (indexed as P) represents the electric polarization of a ferroelectric material, the red region (indexed as ε) represents the strain of a ferroelastic material, and the blue region (indexed as M) represents the magnetization of a ferromagnetic material. The arrows indicate the switching and coupling mechanisms, with the green arrows emphasizing magnetoelectric (ME) coupling.

The term "multiferroic" typically refers to materials that simultaneously exhibit ferroelectric and ferromagnetic orders. Ferromagnetic materials possess a permanent magnetic moment even in the absence of an external magnetic field and demonstrate significant spontaneous magnetization. However, spontaneous magnetization is not apparent in these materials due to the presence of domains, each with its own magnetization direction. When an external magnetic field is applied, domains with magnetizations most aligned to the field grow, at the expense of those with less favorable orientations. Magnetic

materials complement silicon in current technologies: while silicon is used for information processing, magnetic materials enable data storage in a binary form through the opposing orientations of their magnetic dipoles.

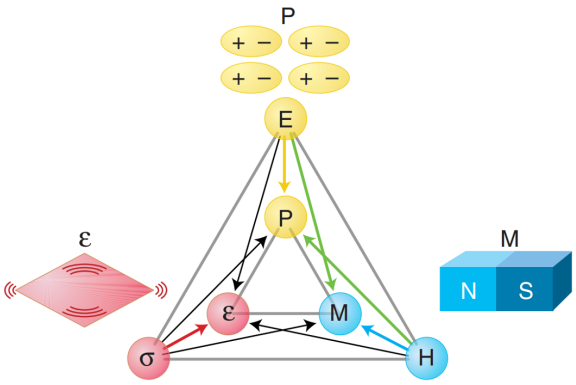

Figure 1.1: Switching and coupling of ferroic orders in a typical multiferroics material. Adapted from [5].

While magnetic data bits are stable, small, and quickly accessible, generating the necessary magnetic fields to control magnetism requires bulky, expensive, and energy-intensive components. On the other hand, ferroelectricity arises from the breaking of centrosymmetry in the crystallographic unit cell and can be manipulated through mechanical stress, chemical modifications, or the application of an external electric field. As a result, ferroelectric materials are polar dielectrics that exhibit spontaneous polarization, which can be reversed by an external electric field [6]. The ability to couple ferroelectric responses with other properties makes ferroelectric materials ideal for numerous technological applications, such as piezoelectric sensors and actuators [7], electromechanical devices [8], and non-volatile ferroelectric memories [9, 10].

A key feature of multiferroics is magnetoelectric coupling [11], where a magnetic field can tune electric polarization and an electric field can influence magnetization. This offers an advantage over conventional magnetic materials, as magnetism in multiferroics can be controlled using electric fields. Compared to magnetic fields, electric fields are more efficient, as they require smaller components and consume less energy. The coupling between different order parameters makes the physical properties of multiferroics highly promising for applications in new technological devices [12]. The rise of multiferroic materials in modern technology highlights the progress made in understanding their fundamental properties, but challenges remain that hinder the departure from traditional paradigms. Overcoming these challenges and translating scientific discoveries in multiferroics into practical applications will require innovative approaches, advanced materials engineering, and new tools to characterize the coupled behaviors of these materials [13].

Among the multiferroic materials with significant potential to drive this technological paradigm shift, bismuth ferrite ($BiFeO_3$) stands out as the most important. It

is the most extensively studied multiferroic, with nearly 6000 publications over the last decade [14]. $BiFeO_3$ is a canonical multiferroic material characterized by the coexistence of ferroelectric ($T_C \approx 1103$ K) and antiferromagnetic ($T_N \approx 643$ K) phases at room temperature, making it known for its excellent ferroelectric properties [15]. In contrast to the properties observed in $BiFeO_3$ ceramics, epitaxial thin films of $BiFeO_3$ exhibit a high remnant polarization ($P_r \approx 100\ \mu C/cm^2$) at room temperature, positioning this lead-free material as promising for microelectronic devices such as ferroelectric random-access memory (FeRAM) [16], multi-state memories [17], and others. The high polarization in $BiFeO_3$ is attributed to the stereochemical activity of the Bi^{3+} $6s^2$ lone pair, while the robust antiferromagnetism stems from the 3d electrons of Fe [18]. In addition to its structural and magnetoelectric properties, other intriguing behaviors—such as the photovoltaic effect [19], photocatalysis [20], photostriction [21], and electrochromism [22]—have been observed in nanostructured and nanoparticulated $BiFeO_3$. The photovoltaic effect [23], associated with its relatively low visible bandgap (≈ 2.7 eV), has attracted significant interest due to its potential for developing novel photovoltaic devices, despite its low energy conversion efficiency. These unique properties make $BiFeO_3$ highly attractive from a technological standpoint. On the scientific front, the unclear physical mechanisms behind the photovoltaic effect and the need to understand the fundamental physics of multiferroic behavior continue to make $BiFeO_3$ an exciting subject for research. The ongoing research on $BiFeO_3$ is unveiling fascinating physics and revealing new potential applications.

1.2 Bismuth Ferrite

1.2.1 Characteristics and properties

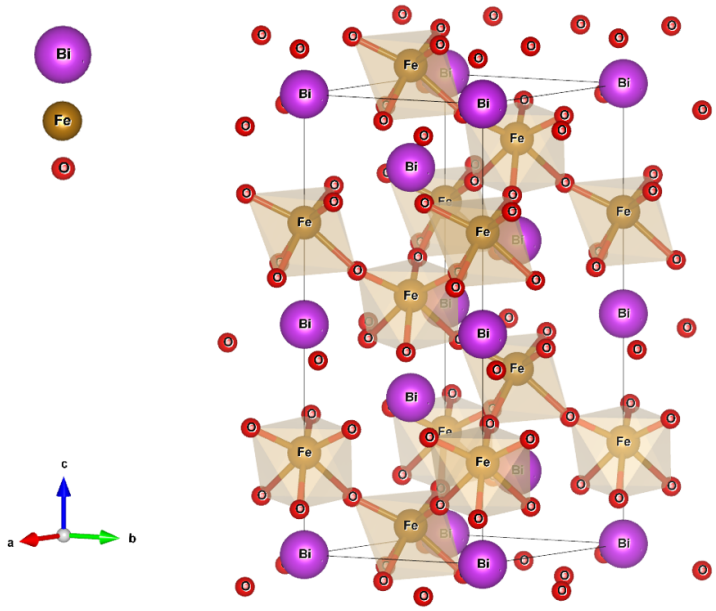

Figure 1.2: $BiFeO_3$ crystal structure. The atoms size is proportional to the radii.

Bismuth ferrite (BFO), as previously introduced, is a multiferroic material with a rhombohedral crystal structure and space group $R\bar{3}c$. This space group is non-centrosymmetric, which allows for atomic displacements, giving rise to its ferroelectric properties [24]. The BFO unit cell is a type of oxide perovskite, where octahedra of oxygen are bonded around Fe^{3+} ions in the B-site (the center of the perovskite structure), and Bi^{3+} ions occupy the A-site. Figure 1.2 illustrates the structure of BFO. The lattice parameters, at room temperature, are $a = b = c = 3.96$ $\mathring{A}$ and $\alpha = \beta = \gamma = 89.3$ ° in its pseudocubic form, however, representing as hexagonal as cited, the parameters are $a = b = 5.58$ $\mathring{A}$ and $c = 13.89$ $\mathring{A}$.

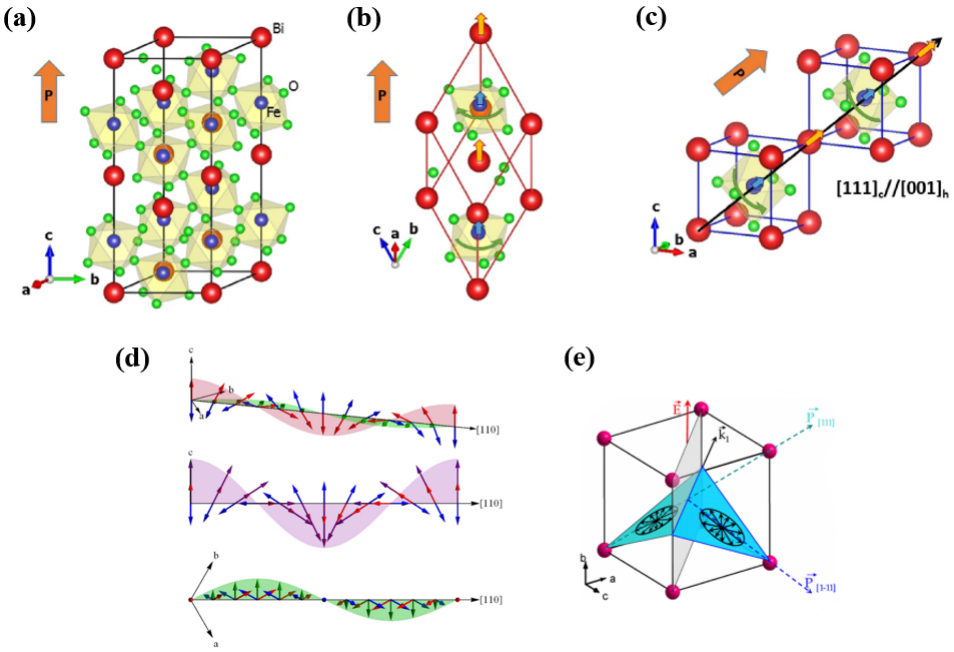

Figure 1.3: Electric and magnetic properties of $BiFeO_3$ along the crystal structure. Adapted from [25].

Figure 1.3 schematically illustrates the electric and magnetic properties of $BiFeO_3$ within its crystalline lattice. It is known that two mechanisms contribute to the ferroelectric order: the displacive mechanism and the lone-pair mechanism. The latter, which is responsible for the ferroelectric phase of $BiFeO_3$, arises from the valence shell of Bi^{3+} $6s^2$ lone pairs. These lone pairs displace from their symmetrical positions in relation to neighboring oxygens [18] and align along the crystalline direction $[111]_{\text{pseudocubic}}$ (or $[001]_{\text{hexagonal}}$), similar to the displacement of Bi ions, as shown in Figure 1.3 (a), (b), and (c). Some theoretical calculations predict a high polarization of around 100 $\mu C/cm^2$, which is associated with the high Curie temperature [18]. Regarding the magnetic properties of $BiFeO_3$, its (anti)ferromagnetism, specifically the G-type antiferromagnetism, originates from the Fe^{3+} ions in the B-site of the perovskite structure [26], where the magnetic moment forms a cycloid with a spatial periodicity of approximately 62 nm, as seen in Figure 1.3 (d). From Figure 1.3 (c) and (d), it is clear that polarization occurs along the $[001]_{\text{hexagonal}}$ direction, while wave propagation follows the $[110]_{\text{hexagonal}}$ direction. These directions define the crystallographic planes along which spin rotations occur, as shown in Figure 1.3 (e).

1.2.2 Problem in working with Bismuth ferrite

One of the biggest obstacles in the practical application of $BiFeO_3$ -based materials is the difficulty of synthesizing them, which hinders mass production with precision and accuracy required for obtaining a single-phase material. This challenge arises from

the narrow conditions for $BiFeO_3$ in the equilibrium diagram. As shown in Figure 1.4, even slight deviations in stoichiometry lead to the formation of secondary phases. In other words, to synthesize a pure, single-phase $BiFeO_3$, it is crucial to maintain an exact molar proportion.

$$Fe_2O_3 + Bi_2O_3 \rightarrow 2BiFeO_3.$$

Thus, the possible secondary phases in $BiFeO_3$ (excluding doped or substituted BFO) include oxides of Bi and Fe (Bi_2O_3 and Fe_2O_3, respectively), bismuth-rich sillenite ($Bi_{25}FeO_{39}$), and iron-rich mullite ($Bi_2Fe_4O_9$). Strict control during the synthesis of BFO is essential; for instance, temperatures above 700 °C can volatilize bismuth, favoring the formation of these secondary phases [15, 27], which directly interfere with the material's electrical properties [28, 29].

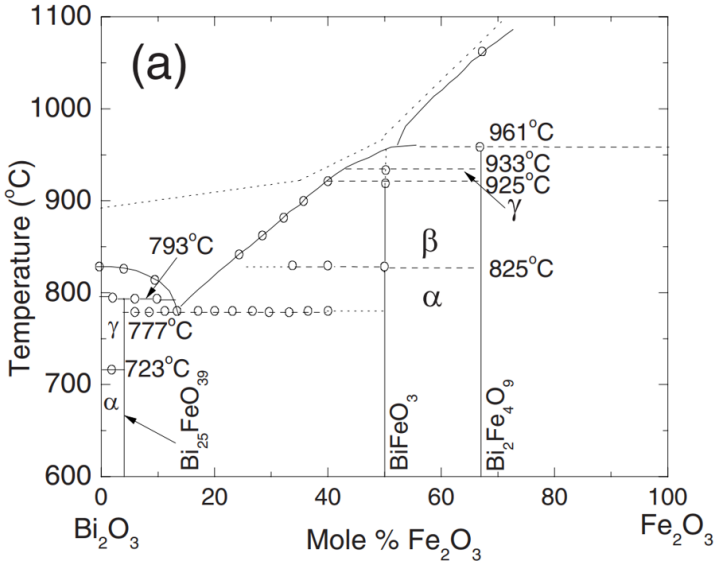

Figure 1.4: Equilibrium diagram of $BiFeO_3$ and possible phases. Adapted from [30].

In addition to secondary phases, the electrical properties of BFO are significantly compromised by oxygen vacancies [29, 31, 32], the hopping of Fe^{3+} to Fe^{2+} [28, 31, 33], and Bi vacancies [31, 34], which generate leakage currents, especially in thin films [35]. These defects also impact the optical [36] and polarization [29, 37] properties. While theoretical studies predict high polarization in BFO, the presence of secondary phases and these defects are likely the main causes of the experimentally observed low polarization in $BiFeO_3$.

Extensive research has been conducted to investigate the formation of the $BiFeO_3$ phase and to regulate the development of intermediate phases through various chemical approaches and structural configurations, including bulk materials, nanoparticles, thin films, solid-state reactions, and hydrothermal methods [38–45]. Additionally,

the literature reports that substituting A-site cations with rare-earth elements such as Sm, La, Nd, Eu, and Tb, among others [46, 47], is intended to enhance electrical properties by examining leakage current, impedance spectroscopy [48], and piezoelectric activity [49]. Meanwhile, the incorporation of metal elements such as Ba, Ca [50], and Gd has been shown to reduce leakage current, enabling a more precise definition of hysteresis loops [51]. Conversely, B-site substitutions with transition metals such as Mn, Ti, and Sn can improve the structural, physical, and chemical properties of $BiFeO_3$ [24, 52, 53] while also enhancing its electrical performance [32, 41, 43].

Doping has been widely employed to modify the physical properties of $BiFeO_3$ and indirectly regulate the formation of secondary phases during growth. The approaches used in these studies highlight the necessity of understanding the nucleation and crystallization kinetics of the $BiFeO_3$ system beyond the research conducted to date. The crystallization kinetics of $BiFeO_3$ is highly dependent on the synthesis method and the material's form, whether as bulk ceramics, nanoparticles, or thin films. A notable example illustrating this dependence is the fact that $BiFeO_3$ nanoparticles typically exhibit lower crystallization temperatures compared to bulk ceramics or thin films. Cabral *et al.* [54] investigated the growth kinetics of $BiFeO_3$ nanoparticles from an amorphous precursor using in situ synchrotron X-ray powder diffraction. Rojac *et al.* [55] provided a review on kinetic formation but focused primarily on the formation of mullite and sillenite phases, with limited discussion on the physical and chemical properties of $BiFeO_3$. Similarly, Preethi *et al.* [46] reviewed the effects of doping and site substitution in $BiFeO_3$ -based perovskites but did not address the kinetics of perovskite formation and how the synthesis protocol influences on the physical properties.

Based on the discussions presented, the next section outlines the objectives and goals of this work.

1.3 Goals

Based on the research group's experience [14, 56–63], this study will focus on bismuth ferrite in the form of a thin film. Therefore, the general objective of this work is "to map the ideal crystallization temperature for the synthesis of bismuth ferrite thin films by analyzing defect formation and modulating physical properties".

To achieve this goal, we have outlined the following specific objectives:

1. To synthesize pure and monophasic $BiFeO_3$ at different crystallization temperatures, specifically at 580°C, 600°C, 620°C, and 640°C.

2. To understand the reaction kinetics, specifically the nucleation and growth mechanisms, of the BFO phase.

3. To investigate the structure, microstructure, chemical characteristics, and morphology using various characterization techniques.

4. To analyze the dielectric and optical behaviors and interpret the effects using appropriate physical models.

5. To explain the observed effects and phenomena, drawing connections between the results obtained.

6. To develop this dissertation to provide valuable information and insights on the optimal conditions for enhancing the properties of $BiFeO_3$-based materials.

Chapter 2

Materials and method

This chapter details the procedures for synthesis, sample characterization, reagent preparation, equipment use, and data analysis methodologies.

2.1 Synthesis

The $BiFeO_3$ films were prepared using Schwartz method [64], which is analogous to the sol-gel technique. We used glacial acetic acid and methoxyethanol as solvents that act as chemical modifier, facilitating the distribution of metal ions along the organic chain of the acids. Prior to synthesis, nitrate bottles were placed under vacuum in a desiccator within a controlled environment (air-conditioned) for five days to account for the hygroscopic nature of nitrates. This precaution minimized the absorption of water molecules from the environment, which could otherwise affect the measured mass and introduce stoichiometry deviations, potentially forming the formation of secondary phases.

Initially, 0.7753 g of bismuth nitrate pentahydrate, $Bi(NO_3)_3{\cdot}5H_2O$ (Sigma-Aldrich, $\geq$ 98.0 %), and 0.6457 g of iron nitrate nonahydrate, $Fe(NO_3)_3{\cdot}9H_2O$ (Sigma-Aldrich, $\geq$ 98.0 %), were dissolved in 5 ml of glacial acetic acid, CH_3COOH (Sigma-Aldrich, $\geq$ 99.7 %), under magnetic stirring at 57 °C. The solution was maintained at this temperature for 90 minutes and then heated to 80 °C for 30 minutes to reduce the volume to 2 ml. The solution was then allowed to cool to room temperature while being stirred for 10 minutes, after which 1.5 ml of methoxyethanol, $CH_3OC_2CH_2OH$ (Sigma-Aldrich, $\geq$ 99.9 %), was added. This yielded a final solution volume of 3.5 ml with a molarity of 0.32 mol/L. Figure 2.1 provides a schematic representation of the process.

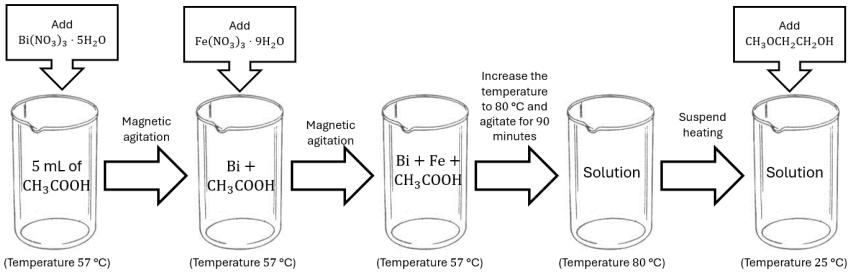

Figure 2.1: Flowchart of the processes to prepare the precursor solution for synthesis.

The substrates chose to be used were $Pt/TiO_2/SiO_2/Si(100)$ non-oriented. The substrates plates were previously washed with running water and neutral detergent, and then dried in a hot plate at 200 °C. We deposited the precursor solution via spin-coating (Spin-coater Chemat KW_4A), and the processes are hereafter described following the flowchart in Figure 2.2. The deposition was carried out in three stages,

1. Drip the solution onto the substrate, spin-coating it at 2000 rpm for 10 seconds, followed by 5000 rpm for 30 seconds. Allow the coated samples to dry on a hot plate at 200 °C for 2 minutes to remove water;

2. Place the samples in an oven at 500 °C for 10 minutes to burn off organic compounds (pyrolysis). This process was repeated 10 times to achieve a 500 nm thick film;

3. Finally, crystallize the samples at various temperatures: 580 °C, 600 °C, 620 °C, and 640 °C, each for 30 minutes. One non-crystallized (virgin) sample was reserved for comparison studies.

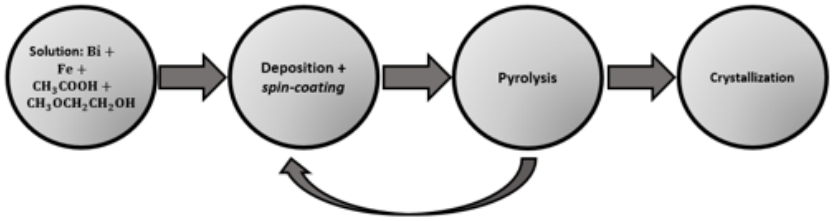

Figure 2.2: Flowchart of deposition step of synthesis.

After the crystallization time was completed, the samples were removed from the furnace (quenched) to preserve the concentration of point defects formed at the crystallization temperature. This is based on the relationship $N_V = N \exp\left(-\frac{Q_V}{k_B T}\right)$, where N_V represents the number of vacancies, N is the pre-exponential factor, Q_V is the energy required for vacancy formation, k_B is the Boltzmann constant, and T is the absolute temperature.

The Figure 2.3 exhibits the samples' photographs as a function of deposition number, and Table 2.1 shows the samples' nomination that we used in this manuscript. The name letters refers to the abbreviation of compounds of formula $BiFeO_3$ and the following number is the crystallization temperature; letters after number, such as A and B, are to identify the twin samples.

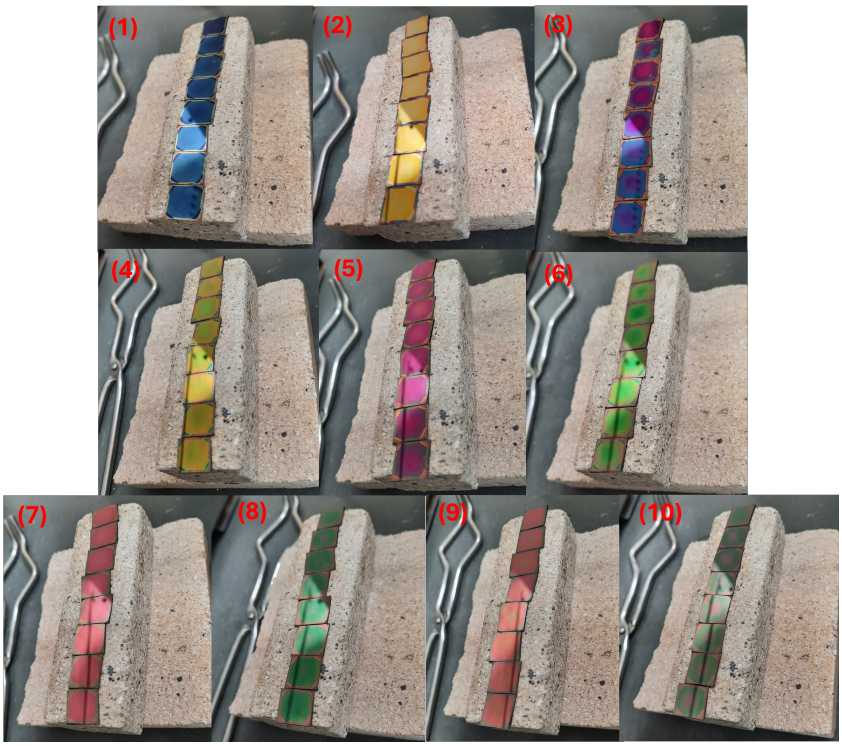

Figure 2.3: Samples' photographs as a function of number of depositions. The number between parenthesis indicates the respective number of deposition. All photographs were taken after the pyrolysis process; therefore, none of them underwent the crystallization process and can be considered identical.

Table 2.1: Code name described of samples studied. The term "T" means the crystallization temperature.

CODE	**PYROLYSIS**	**T (°C)**
BFO-500A	200°C/2min+500°C/10min	Virgin
BFO-500B	200°C/2min+500°C/10min	Virgin
BFO-500C	200°C/2min+500°C/10min	Virgin
BFO-500D	200°C/2min+500°C/10min	Virgin
BFO-580	200°C/2min+500°C/10min	580
BFO-600A	200°C/2min+500°C/10min	600
BFO-600B	200°C/2min+500°C/10min	600
BFO-620	200°C/2min+500°C/10min	620
BFO-640	200°C/2min+500°C/10min	640

The twin samples BFO-500A, BFO-500B, BFO-500C, and BFO-500D were prepared as a precaution to ensure the availability of additional samples under identical conditions, should such a need arise during the research. This approach proved necessary in the case of samples BFO-600A and BFO-600B. During the characterization process, BFO-600A exhibited exceptional properties, necessitating the preparation of a replica for

further study. However, these additional investigations fall outside the scope of this dissertation. Throughout the discussions in this manuscript, we will omit the term indicating twin samples to emphasize only the temperature at which the samples were crystallized.

Photographs were taken after each organic burning process in the electric oven (pyrolysis), as schematically illustrated in Figure 2.3. Two main effects were observed in the interactions between the sample surfaces and light: apparent color shifting (almost cyclic) and the transition between specular and diffuse reflection, which varied as a function of the deposition number. The apparent color shifting is associated with the thickness of the samples. Light interacting with the sample undergoes partial reflection and refraction, resulting in constructive and destructive interference. Depending on the magnitude of the thickness, constructive interference can enhance a specific color, progressing from blue for the thinnest layers to red for the thickest. The cyclical color variations observed in the photographs occur when the thickness reaches a multiple that reinforces the constructive interference of a previously observed color. Notably, in Figure 2.3(10), the predominant color is green, corresponding to a wavelength of approximately 500 nm, which aligns with the expected thickness from the synthesis process. The transition from specular to diffuse reflection can be attributed to surface roughness. The deposition process occurs layer by layer, repeated ten times, progressively reducing surface defects after each pyrolysis. Light transmitted through the sample is reflected by the metallic substrate. During the initial deposition, the thin layer exhibits specular reflection due to low absorption and a smooth surface. As additional layers are deposited, the sample thickness increases, resulting in greater absorption and surface roughness, which leads to a more diffuse reflection behavior.

2.2 Structural characterizations

The initial characterizations in all samples were the structural, microstructural and topography. We performed X-ray diffraction (XRD), Raman scattering spectroscopy (RSS), X-ray photoelectron spectroscopy (XPS) and Scanning electronic microscopy (SEM) techniques. All setting, brands and analysis formalisms are described in this section, as well as the complementary analysis.

2.2.1 X-ray Diffraction (XRD)

Aiming to characterize the structure, analyze the present phases, formation, and estimate the crystallite size, microstrain, unit cell parameters and ions position, we performed the X-ray diffraction (XRD) measurements. The equipment used was a X-ray Diffractometer Rigaku Ultima IV, located in the Ferroelectric Group at Department of Physics and Chemistry (FEIS-UNESP), using K_α radiation of copper, $\lambda = 1.6406\ \mathring{A}$, with

40 mA of electric current and 40 kV of voltage. The configuration was the "step-scan" mode $\theta - 2\theta$, in the range angle 20 °$\leq 2\theta \leq$ 60 °, with increment of 0.02 ° each 4 s.

The patterns in the diffractograms were analyzed using the Rietveld refinement method [65, 66]. Refinements were performed with the GSAS software [67], utilizing the EXPGUI graphical interface [68] for structure modeling. Peak profiles were fitted using a pseudo-Voigt function [69], while the background was modeled using an eight-order Shifted Chebyshev polynomial. The refinements involved adjusting various parameters, including background, unit cell dimensions, ion coordination, scale factor, zero-point correction, peak width, and thermal parameters. The quality of the refinements was assessed using the χ^2 goodness-of-fit metric [70], defined as:

$$\chi^2 = \left(\frac{R_{wp}}{R_{exp}}\right), \tag{2.1}$$

where R_{wp} and R_{exp} are parameters of weighed profile factor and expected statistically, respectively. We can also attest the "good quality" of the refinements through the Willianson-Hall (WH) curves [71], given by 2.2.

$$\frac{(\Gamma\cos(\theta))}{\lambda} = \left(\frac{1}{D}\right) + \left[\left(\frac{4\Delta d}{d}\right)\cdot\frac{1}{\lambda}\right]\sin(\theta), \tag{2.2}$$

where λ is the wavelength used (K_α of copper), θ is the angle of Bragg, d is the lattice spacing, Γ is the full width at half maximum, D is the average size of crystallite, and $\frac{\Delta d}{d}$ is the microstrain. Thus, fitting linearly the WH curves we could estimate the microstrain (ε) and average crystallite size (D) through the following relations,

$$\Gamma\cos(\theta) = \left(\frac{\lambda}{D}\right) + \left(\frac{4\Delta d}{d}\right)\sin(\theta) \rightarrow y = ax + b \Rightarrow$$

$$\Rightarrow y = \Gamma\cos(\theta),\ x = 4\sin(\theta),\ a = \frac{\Delta d}{d} = \varepsilon,\ b = \frac{\lambda}{D}.$$

Thus, the refinement can also be attested through the dispersion of points in WH curves, not only through χ^2.

2.2.2 Raman Scattering Spectroscopy (RSS)

In addition to XRD, we employed Raman Scattering Spectroscopy (RSS) as a complementary technique to study the structure. Unlike XRD, which provides long-range structural analysis, RSS focuses on short-range structural characteristics.

The interaction between light and matter gives rise to various phenomena, including reflection, absorption, transmission, and scattering. When light strikes the surface of a material, part of its intensity is reflected, while the remainder is transmitted

into the material. Within the material, the transmitted light may be partially absorbed as heat and partially scattered. The scattered light often exhibits frequencies different from the incident light. This process underpins Raman Scattering Spectroscopy (RSS) [72].

The RSS measurements involve detecting light scattered by the sample in a suspended state, allowing structural and chemical information to be obtained for various compounds, whether organic or inorganic, with the exception of metal compounds. This technique provides insights into atomic arrangements, molecular interactions, and crystalline symmetry. Identification is based on the characteristic frequencies of radiation scattered by groups of atoms within the material [72–75]. A comprehensive understanding of RSS requires a solid grasp of the mathematics underlying space group theory and detailed analysis of vibrational spectra, which are beyond the scope of this dissertation. In this work, RSS was employed solely as a complementary technique for short-range structural analysis of the samples.

The space group theory predicts, for $BiFeO_3$, 13 actives modes given by the following Equation 2.3:

$$\Gamma = 4A_1 + 9E, \tag{2.3}$$

where A_1 modes are referred to the vibration of bonding between Bi-O, and E modes are correspondent to the vibration of bonding between Fe-O, being the vibration of symmetry A_1 in the parallel direction of axis $[111]_{\text{pseudocubic}}$, meanwhile the vibrations of symmetry E are in perpendicular to this axis. Thus, we used 13 Lorentzian to fit RSS data, following the initial set of peaks positions values [76–81], commonly reported in literature (ceramics and films[1]):

$$\begin{cases} A_1 = \{147, 176, 227, 490\}\ \text{cm}^{-1} \\ E = \{77, 136, 265, 279, 351, 375, 437, 473, 525\}\ \text{cm}^{-1} \end{cases} . \tag{2.4}$$

The equipment we used to perform the RSS measurements was the confocal Microscopy Raman BX_{51}-Voyage™, Microscopy Nikon®Eclipse 8oi, 150 mW to 785 nm of laser excitation with 3.0 cm^{-1} of resolution, located in the Ferroelectric Group at Department of Physics and Chemistry (FEIS-UNESP). Our range of study was from 100 to 600 cm^{-1}.

[1]The position of the peaks may deviate depending on the architecture of the material, i.e., bulk, film, powder etc. We selected those points only for the aim to facilitate the fit supplying the algorithm an initial value.

2.2.3 X-ray Photoelectron Spectroscopy (XPS)

The X-ray Photoelectron Spectroscopy (XPS) is a technique of measurements that was founded from the photoelectric effect and it allows us to analyze the compounds of a material's surface as well as their relative concentration and chemical states.

As discussed in Section 1.2.2, BFO exhibits a high leakage current, often attributed to oxygen vacancies, bismuth vacancies, and iron reduction. By analyzing these chemical states and their relative concentrations, it becomes possible to infer and correlate the electrical and optical properties with the concentration of point defects.

Based on the characteristic survey curve of the XPS measurements, we focused on analyzing the chemical states of Bi 4f, Fe 2p, and O 1s, which are associated with the previously mentioned defects. The baseline was modeled using the Shirley type, and deconvolution was performed using Gaussian functions. From this, the ratios Fe^{3+}/Fe^{2+} and O_I/O_{II} (where O_I refers to lattice oxygen and O_{II} to oxygen vacancies) were calculated by integrating the areas of the Gaussian peaks, since each chemical state corresponds to a specific binding energy distribution.

The equipment we have performed the XPS measurements was using a $Al_{K\alpha}$ radiation (1486 eV), with number of scans 10m, spot size 300 μm, pass energy 50.0 eV, energy step size 0.10 eV and dwell time 50 ms.

2.2.4 Scanning Electron Spectroscopy (SEM)

Scanning Electron Microscopy (SEM) is one of the most commonly used characterization techniques for a wide range of materials. This method allows for high-resolution imaging of a material's surface by directing a focused electron beam onto a small, targeted region. As the electrons interact with the atoms on the material's surface, various signals are emitted, which are then collected and analyzed to provide detailed information about the surface morphology and composition of the material. Most SEM systems utilize a tungsten filament as the electron source, due to its ability to produce a stable and reliable electron beam. This technique is valuable for investigating the microstructure, topography, and other surface properties of materials across a broad spectrum of fields, including materials science, biology, and engineering.

In general, for samples to undergo Scanning Electron Microscopy (SEM) analysis, they must be conductive. This is essential because non-conductive materials tend to accumulate charge on their surface during imaging, which can degrade the resolution by introducing noise. When the electron beam strikes the material's surface, it can cause localized regions to become negatively charged. If this charge accumulation is significant, it can disrupt the imaging process by deflecting both the incident and emitted electrons,

leading to distorted or poor-quality images [82]. To prevent this, non-conductive materials are often coated with a thin layer of gold via sputtering, which ensures that electrons can flow freely and prevents charge buildup. However, in our study, although our samples are not conductive, we chose not to sputter them with gold. This is because the sputtering process is destructive and could interfere with subsequent characterizations, which require the integrity of the sample surface to be maintained.

The equipment we used to do the SEM images was the Scanning Electron Microscopy environmental of Zeiss, model EVO LS_{15} with electron filament of tungsten anode. To analyze the images, we used the software ImageJ [83].

2.3 Electric characterizations

After the initial characterization to analyze phase formation and the other properties mentioned in subsection 2.2, it is necessary to evaluate the electrical properties of the samples. This section is dedicated to that analysis. We performed Complex Impedance Spectroscopy (IS), Leakage Current Density (LC) and Piezoresponse Force Microscopy (PFM) measurements, which are described in this section.

2.3.1 Preparation of samples

The use of the platinum substrate ($PT/TiO_2/SiO_2/Si(100)$) have been employed in the research group in the past studies [14, 56, 57], aiming to measure and analyze the electric and dielectric properties and behavior of $BiFeO_3$ thin films. Thus, analogous to a parallel plates capacitor, the platinum substrate represent one of the plates.

To perform the electrical measurements, circular gold electrodes were deposited on the sample via sputtering. The electrodes had an approximate area of 340 nm^2, and the sputtering process was carried out using a Scancoat Boc Edwards system, with a current of 20 mA and a voltage of 1.5 kV, all controlled under an argon atmosphere. The sputtering was performed on a sample that had been previously cut, allowing the remaining parts to be used for other measurements, such as those in Section 2.4. The gold electrodes were arranged in a matrix pattern, either 4x4 or 5x5, depending on the size of the sample area.

The following Figure 2.4 illustrates the metal/ferroelectric/metal system, composed of gold, $BiFeO_3$, and platinum, respectively.

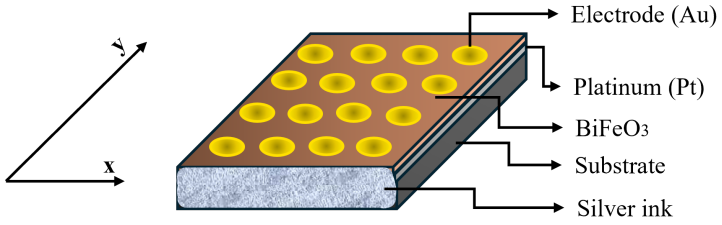

Figure 2.4: System of a parallel plates capacitor of BFO thin film to electric characterization.

Using this setup, we created a matrix system to identify each electrode. Silver ink was used to connect the platinum thin film to the sensor, serving as a reference and acting as an identifier vector (see Figure 2.4 above). This approach ensures the reproducibility of the measurements, should it be necessary to repeat or verify the results.

2.3.2 Complex Impedance Spectroscopy (IS)

The Complex Impedance Spectroscopy (IS) is a technique that consists in analyze a material submitted to an alternate voltage. In short, the impedance can be defined as:

$$Z^*(\omega) = \frac{F\{V(t)\}}{F\{i(t)\}}, \tag{2.5}$$

where $F\{\}$ is the Fourrier Transform, and the asterisk symbols $(*)$ indicates a complex number. However, once the alternate voltage is sinusoidal, $V(t) = V_0 \sin(\omega t)$, we can describe the complex impedance as the ratio between the maximum voltage per maximum of electric current, as follows,

$$Z^* = \frac{V_{\max}}{i_{\max}}. \tag{2.6}$$

Thus, admitting that the voltage and electric current can assume a complex value, as $V^*(t) = V_0 e^{j\omega t}$, where $j = \sqrt{-1}$, then:

$$Z^*(\omega) = \frac{V^*}{i^*}. \tag{2.7}$$

All of the detailed discussions and mathematic development about the impedance description, in each element of a electric circuit and their combination, were already done [14, 62]. In this work, we are not concerned about to explain and describe deeply the IS technique, but using it to analyze the properties between samples itself. However, it is important to highlight that the equivalent electric circuit model we used to describe the dielectric behavior of our samples was the brick-layer one.

The original brick-layer model is composed by a resistor in parallel to a capacitor, in series to another resistor in parallel with a capacitor, which makes an allusion to a real brick layer, being the grains with high conductivity as the bricks, surrounded by grain boundaries with high resistivity [84–86]. In this work, we used the brick-layer with CPE (constant phase element) model, shown in Figure 2.5

The CPE admits there is a distribution of relaxation time [87, 88] that, in our case, it is associated to the grain boundary. In Figure 2.5, the index **g** is referred to the grain properties and **gb** to the grain boundary properties.

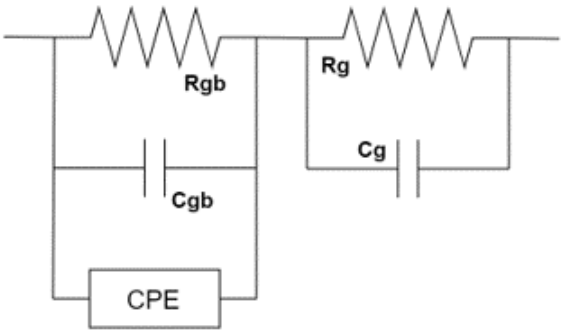

Figure 2.5: Brick-layer with CPE model. Left side of the circuit is related to the grain boundaries' properties (index with **gb**), and the right side to the grains' properties (index with **g**).

To analyze and fit the data (spectra), we employed both electric impedance and electric modulus, where the electric modulus is defined as the reciprocal of the permittivity, $M^* = 1/\varepsilon^*$. Electric impedance provides valuable insights into the resistance of the material, while the electric modulus offers information related to the capacitance. It is important to note that the electric modulus, like the electric impedance, is a complex quantity. Therefore, it is necessary to separate the real and imaginary parts of both the electric impedance and the electric modulus for accurate analysis. The relationship between electric impedance and electric modulus is given by the Equation 2.8, which facilitates the conversion of data between the two quantities. By utilizing this approach, we were able to gain a deeper understanding of the material's electrical behavior, including its resistance and capacitive properties, across different frequencies and under varying experimental conditions.

$$\underbrace{M^* = j\omega C_0 Z^*}_{Z^*=Z'-jZ'',\ M^*=M'+jM''} \quad . \tag{2.8}$$

We fitted the curves varying the parameters between Z' (real impedance), Z'' (imaginary impedance), M' (real modulus) and M'' (imaginary modulus), through the following equations:

$$Z' = \frac{R_{gb}\left[1 + R_{gb}A\omega^n \cos\left(\frac{n\pi}{2}\right)\right]}{\left[1 + R_{gb}A\omega^n \cos\left(\frac{n\pi}{2}\right)\right]^2 + \left[\omega R_{gb}C_{gb} + R_{gb}A\omega^n \sin\left(\frac{n\pi}{2}\right)\right]^2} + \frac{R_g}{1 + \left(\frac{f}{f_g}\right)^2}, \quad (2.9)$$

$$Z'' = \frac{R_{gb}\left[\omega R_{gb}C_{gb} + R_{gb}A\omega^n \sin\left(\frac{n\pi}{2}\right)\right]^2}{\left[1 + R_{gb}A\omega^n \cos\left(\frac{n\pi}{2}\right)\right]^2 + \left[\omega R_{gb}C_{gb} + R_{gb}A\omega^n \sin\left(\frac{n\pi}{2}\right)\right]^2} + \frac{R_g\left(\frac{f}{f_g}\right)}{1 + \left(\frac{f}{f_g}\right)^2}, \quad (2.10)$$

$$M' = \frac{(\omega C_0)R_{gb}\left[\omega R_{gb}C_{gb} + R_{gb}A\omega^n \sin\left(\frac{n\pi}{2}\right)\right]^2}{\left[1 + R_{gb}A\omega^n \cos\left(\frac{n\pi}{2}\right)\right]^2 + \left[\omega R_{gb}C_{gb} + R_{gb}A\omega^n \sin\left(\frac{n\pi}{2}\right)\right]^2} + \frac{(\omega C_0)R_g\left(\frac{f}{f_g}\right)}{1 + \left(\frac{f}{f_g}\right)^2}, \quad (2.11)$$

$$M'' = \frac{(\omega C_0)R_{gb}\left[1 + R_{gb}A\omega^n \cos\left(\frac{n\pi}{2}\right)\right]}{\left[1 + R_{gb}A\omega^n \cos\left(\frac{n\pi}{2}\right)\right]^2 + \left[\omega R_{gb}C_{gb} + R_{gb}A\omega^n \sin\left(\frac{n\pi}{2}\right)\right]^2} + \frac{(\omega C_0)R_g}{1 + \left(\frac{f}{f_g}\right)^2}. \quad (2.12)$$

Once the curves are fitted, we obtain the resistance and the capacitance of both grain and grain boundary, and the CPE parameters associated to the grain boundary **A** and **n**. These parameters are important to analyze, for example, the dc conductivity of the samples, as hereafter described.

The universal power law of Jonscher is given by:

$$\sigma(\omega) = \sigma_{dc} + A\omega^n, \quad (2.13)$$

where $\sigma(\omega)$ is the conductivity as a function of angular frequency, σ_{dc} is the dc conductivity, and A and n are empirical parameters, which $0 \leq n \leq 1$. Applying the limit of frequency going to zero, we obtain,

$$\lim_{\omega \to 0} \sigma(\omega) = \sigma_{dc}.$$

Through the relation above, the dc conductivity must present, in the curves, a plateau region which should estimate the dc conductivity. In our samples, we did not see any plateau region (discussed in Section 2.3), thus, through the conductivity equation of brick-layer with CPE model, we can apply the limits also going to zero so determine and estimate the dc conductivity as dependent on the parameters of the model:

$$\lim_{\omega\to 0}\sigma(\omega) = \frac{\sigma_g\sigma_{gb}^2 + \sigma_g^2\sigma_{gb}}{(\sigma_g+\sigma_{gb})^2} = \frac{\sigma_g\sigma_{gb}\,(\sigma_g+\sigma_{gb})}{(\sigma_g+\sigma_{gb})^2} = \frac{\sigma_g\sigma_{gb}}{\sigma_g+\sigma_{gb}} \to \sigma_g \gg \sigma_{gb} \Rightarrow$$

$$\Rightarrow \lim_{\omega\to 0}\sigma(\omega) \approx \frac{\sigma_g\sigma_{gb}}{\sigma_g} \approx \sigma_{gb} = \frac{d}{R_{gb}A} \approx \sigma_{dc}. \tag{2.14}$$

To determine the direct current (DC) conductivity of the samples, we employed the relation 2.14. In addition, we applied the same relation using the grain resistance to analyze its conductivity, allowing us to explore the conductivity at the grain level. For these measurements, we utilized the Impedance Analyzer RF Agilent $E_{4991}A$, which operates over a frequency range from 100 Hz to 1 MHz. The temperature during the measurements was varied between 400 and 500 K to study the temperature-dependent electrical behavior of the samples.

2.3.3 Leakage Current Density Analysis (LC)

This analysis consists in applying a voltage through the sample, increasing it step by step and register the electric current from the sample. These results are converted to electric current density versus applied electric field (J-E) and, through these curves, we can analyze the leakage current and the conduction mechanisms. Below, it is briefly described some ways to analyze these mechanisms. It is important to highlight that all models where tested through a linearization, i.e., formatted the original equation into $y = ax+b$ straight line equation (where **a** is slope and **b** is intercept), and possibility of the mechanisms occurrence based on physical conditions (temperature, frequency, maximum applied electric field etc).

There are several models that try to explain the samples' electric behavior, some of them are associated to the contact between the electrode and the surface of sample, and others to the samples' bulk itself [89]. In this work, we considered the models of ohmic conduction, space-charge-limited current, Schottky emission, Poole-Frenkel emission and Fowler-Nordheim tunneling, often reported in BFO ceramics [90].

The ohmic regime can be "simply" described through the equation [89],

$$J = \sigma E, \tag{2.15}$$

where J is the electric current density, σ is the conductivity and E is the applied electric field. We can also describe J as a function of the charge carriers density (n) and the electronic mobility (μ),

$$J = ne^{-}\mu E, \tag{2.16}$$

where e^{-} is the elementary charge (1.602×10^{-19} C).

To attest this conduction mechanism, we plot the curve in log-log scale, once,

$$\begin{aligned} J = \sigma E \Rightarrow \ln(J) = \ln(\sigma) + \ln(E) \Rightarrow \\ \Rightarrow \ln(J) = \ln(\sigma) + 1\ln(E), \end{aligned} \tag{2.17}$$

thus, the slope of the linear fit must be 1 to confirm this mechanism and, therefore, we can estimate the conductivity through the intercept ($\sigma = e^{b}$), or through the slope in linear scale.

A typical curve of the space-charge-limited current (or simply SCLC) in log-log plot is bounded by three limited curves: Ohm's law (previously discussed), traps-filled-limited (TFL) current and Child's law.

The child's law can be described as follows [89],

$$J = \left[\frac{9\varepsilon_0\varepsilon_r\mu}{8L}\right] E^2, \tag{2.18}$$

where ε_0 is the vacuum permittivity (8.85×10^{-12} F/m), ε_r is the relative permittivity (or often named as "dielectric constant") and L is the thickness of sample (500 nm). Linearizing:

$$\ln(J) = \ln\left[\frac{9\varepsilon_0\varepsilon_r\mu}{8L}\right] + 2\ln(E). \tag{2.19}$$

Thus, in a typical SCLC behavior, we must observe the regions with three different slopes:

$$a_{Ohm} = 1,$$

$$a_{TFL} > 2,$$

$$a_{Child} = 2.$$

The Schottky (SC) emission can be mathematically describe as [89],

$$J_{SC} = AT^2 exp\left[-\frac{q\phi - \alpha\sqrt{E}}{k_B T}\right], \tag{2.20}$$

where $q\phi$ is the Schottky barrier height, k_B is the Boltzmann constant, T is the abso-

lute temperature, A is a constant, $\alpha = \left[\frac{q^3}{4\pi\varepsilon_0\varepsilon_\infty}\right]^{\frac{1}{2}}$, and ε_∞ is the optical permittivity. Linearizing the Equation 2.20:

$$\ln\left(\frac{J_{SC}}{T^2}\right) = \ln(A) + \frac{\alpha\sqrt{E} - \phi q}{k_B T}, \tag{2.21}$$

thus, the permittivity should be determined through the slope of the fitting. In addition to a straight-line behavior when the curves are plotted $ln(J/T^2)$ versus $\sqrt{E}$, to guarantee the Schottky mechanism it is necessary to determine the optical permittivity, once it must be physically possible, i.e., higher than 1 ($\varepsilon_r = \varepsilon/\varepsilon_o > 1 \Rightarrow \varepsilon > \varepsilon_0$).

Poole-Frenkel (PF) emission mechanism is very similar to Schottky emission, sometimes called as internal Schottky emission. The thermal excitation of electrons may emit from traps into the conduction band of the material. The equation of this model is [89],

$$J_{PF} = BEexp\left[-\frac{E_I - \beta\sqrt{E}}{k_B T}\right] \Rightarrow$$

$$\ln\left[\frac{J_{PF}}{E}\right] = \ln(B) + \ln\left[\frac{\beta\sqrt{E} - E_I}{K_B T}\right], \tag{2.22}$$

where B is a constant, E_I is the trap energy level, and β is 2α. Thus, the optical permittivity should be also determined through the slope depite the straight-line behavior in this plot.

Finally, Fowler-Nordheim (FN) tunneling is a conduction mechanism which take in count the probability of the electron existing on another side of the potential barrier, of course with some criteria. The following equation describes the FN behavior [89],

$$J_{FN} = CE^2 exp\left[-\frac{D^2\phi^{3/2}}{E}\right], \tag{2.23}$$

$$\ln\left[\frac{J_{FN}}{E^2}\right] = \ln(C) - \frac{D^2\phi^{3/2}}{E}, \tag{2.24}$$

where C and D are constants, ϕ is the potential barrier. It has been reported that the conduction mechanisms models are strongly dependent on the thickness in ferroelectric thin films [91–93]. Thus, there are some consideration about the mechanisms: FN can be ruled out in all samples due to the impossibility of tunneling which requires a thickness equal or less than 50 nm. However, in BFO-500 which presents coexistence of secondary phase, it is possible the tunneling between one phase to another. PF and SC need considerations also once it is oftentimes reported in high fields, which it is not the present

case [94, 95].

In summary, Table 2.2 shows all plots to identify the mechanism through straight-line behavior of the curves:

Table 2.2: Conduction mechanism and their plot axis when linearized.

Model	Equation	x-axis	y-axis
Ohmic	$J_{Ohm} = \sigma E$	$\ln(E)$	$\ln(J_{Ohm})$
SCLC	$J_{SCLC} = \left(\frac{9\varepsilon_o\varepsilon_r\mu}{8L}\right) E^2$	$\ln(E)$	$\ln(J_{SCLC})$
SC	$J_{SC} = AT^2 exp\left(-\frac{q\phi - \alpha\sqrt{E}}{k_B T}\right)$	$\sqrt{E}$	$\ln\left(\frac{J_{SC}}{T^2}\right)$
PF	$J_{PF} = BE exp\left(-\frac{E_I - \beta\sqrt{E}}{k_B T}\right)$	$\sqrt{E}$	$\ln\left(\frac{J}{E}\right)$
FN	$J_{FN} = CE^2 exp\left(-\frac{D^2\phi^{3/2}}{E}\right)$	$\frac{1}{E}$	$\ln\left(\frac{J}{E^2}\right)$

The equipment we used to measure the leakage current density was a electrometer (Keithley 6571b) with a software (Labview) that through a staircase signal obtain the curves i-V (electric current versus voltage). The conversion to J-E was using 500 nm thick and 340 nm^2 of electrode area. We measured from negative to positive branch $\pm$1.5 V, with 0.02 V per second.

2.3.4 Piezoresponse Force Microscopy (PFM)

Ferroelectric materials are part of the group of piezoelectric materials [96], which it allows us investigate the ferroelectric domains patterns through the piezoelectric effect. The technique employed in studying such domains through the piezoelectric effect is the so-called Piezoresponse Microscopy (PFM), which derivatives from another technique, the Atomic Force Microscopy (AFM), however, this one is in contact mode with the sample surface [97]. The application of an alternate potential difference between the cantilever tip and an electrode, located at the bottom of the sample, induce to vibrations which are transmitted to a "lock-in" amplifier, enough sensible to read such displacements.

The Equation 2.25 exhibits a general strain (S_j) induced in a piezoelectric material under an applied electric field (E_i), where d_{ij} is the piezoelectric coefficient [98].

$$S_j = d_{ij} E_i. \tag{2.25}$$

The indices 1 through 3 represent the components along the x, y, and z axes of a three-dimensional orthogonal coordinate system, while indices 4 through 6 correspond to the shear components of the strain tensor. This coordinate system is typically chosen such that its axes align with the crystallographic directions of the crystal being studied, ensuring a clear and consistent reference frame. In the case of ceramics and thin films, the z axis is often selected to coincide with the direction of polarization, which is perpendicular, or normal, to the plane of the film. This alignment facilitates the study of properties influenced by the polarization direction. One important parameter in such systems is the longitudinal piezoelectric constant, denoted as d_{33}. This constant can be experimentally determined by observing the sample's displacement, Δz, along the z axis in response to an applied electric field, E_3, directed along the same axis [99],

$$\Delta z = d_{33} V, \tag{2.26}$$

assuming $S_3 = \dfrac{\Delta z}{z_0}$ and $E_3 = \dfrac{V}{z_0}$, where V is the applied voltage and z_0 is thickness of the sample. Thus, the sample may expand or contract depending on the direction of polarization, if it is parallel or antiparallel. Regarding the small changes in its dimensions, it is easier to detect the effects through a ac measurements, described below.

$$V = V_{ac} \cos(\omega t), \tag{2.27}$$

where V_{ac} is the ac voltage, ω is the angular frequency of the applied voltage, and so, the displacement induced can be described as,

$$\Delta z = d_{33} V_{ac} \cos(\omega t + \phi). \tag{2.28}$$

Therefore, when $\phi = 0$, the polarization points down, and when $\phi = 180\,^{\circ}$, the polarization points up. So, the piezoresponse will oscillate in-phase or out-off phase, if the polarization is parallel or antiparallel, respectively.

It is common in studies like this, with piezoresponse, to record the strain and polarization as a function of the applied electric field [100]. Figure 2.6 exhibits the curves (sketch of the theoretical curves and representation of the experimental curves obtained) of the electric polarization and strain as a function of the applied electric field. The hysteresis loop of electric polarization can be interpreted as a "fingerprint" of a ferroelectric material,

such hysteresis loop is represented in Figure 2.6(c). There are some important points that we must highlight. The maximum value that the electric polarization can reach is named as "saturation polarization"; once polarized and the applied electric field is removed (null electric field), the polarization is not null, this value of polarization is named as "remanent polarization". Reversing the electric field sweep direction, the electric field magnitude able to reach null polarization is named as "coercive field", and the cycle is repeated with same properties in reverse direction. The area below the hysteresis loop curve represents the energy (work) enough to polarize the material.

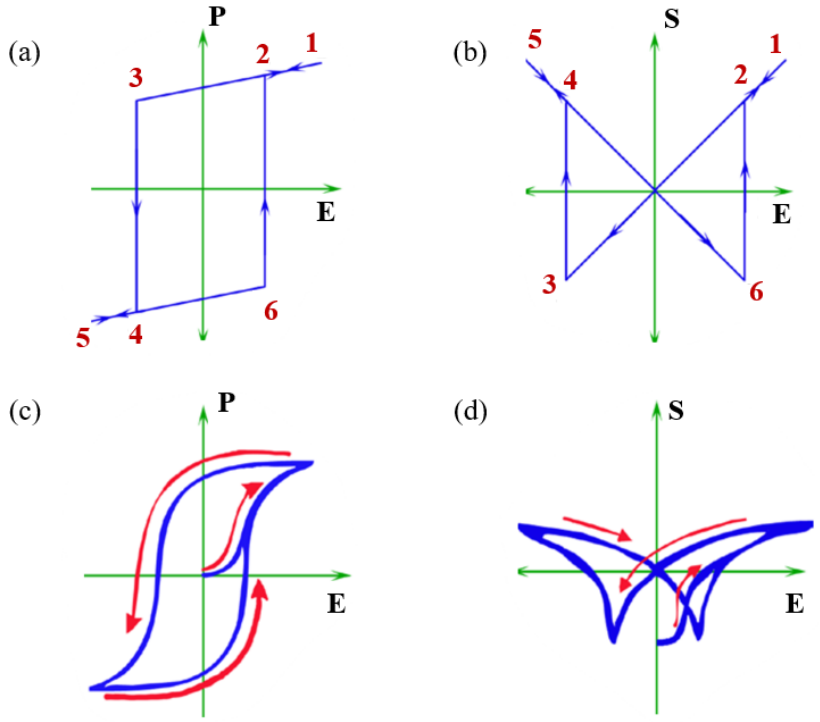

Figure 2.6: Schematically illustrations of dependence of the electric polarization (**P**) and strain (**S**) on the applied electric field (**E**). (a): Theoretical curve of the hysteresis loop of electric polarization, (b): theoretical curve of quadratic hysteresis loop of strain. The indexes 1 to 6 represents the electric field sweep direction during measurements. (c): sketch of a real hysteresis loop of the electric polarization, and (d): sketch of a real hysteresis loop of the strain, known as "butterfly" curve. Adapted from [99].

It is important to highlight that the ferroelectric hysteresis obtained via PFM technique is local, i.e., the analysis is concerned in changes of the electric polarization in nanoscale. The main difference between this technique (known as "switching spectroscopy piezoresponse force microscopy, SS-PFM) and the macroscale measurement to obtain the hysteresis loops is that, whereas macroscopic hysteresis occur due to the growth of the nucleation and the interaction of multiples separated domains (cooperative action), in the hysteresis obtained via SS-PFM the nucleation occurs under a sharp point and the signal follows the development of the ferroelectric domains in a unique region [101].

2.4 Optical characterizations

There are several ways to estimate the bandgap of materials through the Ultraviolet-Visible (UV-Vis) technique. In semiconductor, it is sometimes estimated through the Tauc's plot [102], as follows,

$$(\alpha h\nu)^{1/\gamma} = B\left(h\nu - E_g\right), \tag{2.29}$$

where α is the absorption coefficient, E_g is the bandgap, h is the Planck constant, ν is the photon frequency, B is a constant, and γ is a factor that depends on the nature of the electron transition, it may assume value as 1/2 or 2 for the direct and indirect transition bandgaps, respectively [103, 104]. However, the Tauc's plot maybe provide an estimate with errors, for example errors that are associated with a significant absorption of sub-bandgap energy photons.

Thus, P. Kubelka and F. Munk proposed that the measured reflectance spectra can be transformed to the corresponding absorption spectra through the relation known as Kubelka-Munk (KM) function [105, 106],

$$F\left(R_\infty\right) = \frac{K}{S} = \frac{\left(1 - R_\infty\right)^2}{2R_\infty}, \tag{2.30}$$

where K and S are the absorption and scattering coefficients, respectively, and R_∞ is the reflectance of an infinitely thick specimen, as $R_\infty = \dfrac{R_{\text{sample}}}{R_{\text{standard}}}$. So, substituting these relation in Equation 2.29, we obtain,

$$\left(F\left(R_\infty\right) h\nu\right)^{1/\gamma} = B\left(h\nu - E_g\right). \tag{2.31}$$

In the case of $BiFeO_3$, the electron transition is indirect, i.e., the factor $\gamma = 1/2$. Therefore, the plot of KM function for UV-Vis is:

$$\left(F\left(R_\infty\right) h\nu\right)^2 = B\left(h\nu - E_g\right) \tag{2.32}$$

Once fitting the curves by a straight-line in the steep region, which means a linear increase of light absorption with increasing energy (a semiconductor characteristic), and extending curve, the estimated bandgap is that value where the x-axis is touched.

We used a Hitachi (U2900 model) spectrophotometer, with excitation in the region of ultraviolet and visible from 190 to 1100 nm. The equipment is located in the Physics Institute of São Carlos.

Chapter 3

Results and discussions

3.1 Structural characterizations

In this section, we discuss the structural characterization of the samples using X-ray diffraction techniques and Raman scattering spectroscopy. The phases analysis and their formation were carried out based on the X-ray diffraction pattern. Figure 3.1(a) shows XRD experimental and calculated data of the studies $BiFeO_3$ thin films.

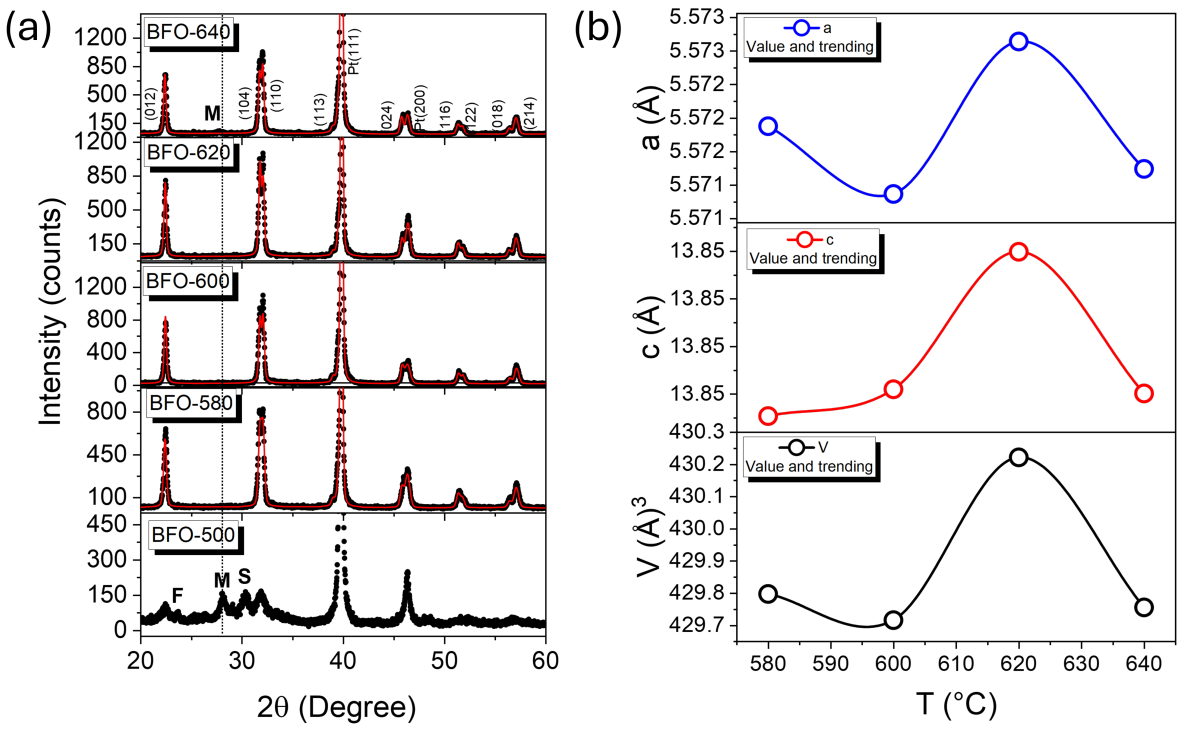

Figure 3.1: (a): X-ray diffraction patterns of samples studied. The black points are the experimental data, the red line is the adjustment by Rietveld refinement, and the dot-line is a guide for the eyes. The planes indexed with Pt is referred to the platinum of substrate and the symbols marks (**F**, **M** and **S**) are refereed to the presence of secondary phases. Phase **F** around 23.6° is correspondent to ferrite Fe_2O_3, the **M** symbol around 28.0° is correspondent to iron rich mullite phase ($Bi_2Fe_4O_9$), and the **S** symbol around 30.5° is correspondent to bismuth rich sillenite phase ($Bi_{25}FeO_{40}$). (b): Parameter **a** and **c** and unit cell volume **V** as a function of crystallization temperature. The lines are guides for the eyes.

We observe clearly the transition between non-crystalline and secondary phases to pure $BiFeO_3$ phase with rhombohedral structure and space group $R\bar{3}c$. The space group can be preliminarily determined through the refinement, assuming a $R\bar{3}c$ space group. However, in sample BFO-640 we can see a prominence that looks like a mullite growth, in what is considered the precision of equipment. We can expect and deduce that BFO phase is thermodynamically stable and secondary phases are kinetically controlled, i.e., $BiFeO_3$ is thermodynamically more stable in crystallization temperatures of 580 °C, 600 °C and 620 °C, once crystallization temperatures 500 °C and 640 °C seem to potentially favor the secondary phases formation. At high temperatures, such as 640 °C, bismuth volatilization likely begins, causing a shift in stoichiometry that favors the formation of the iron-rich phase and mullite. The Table 3.1 shows the parameters obtained from Rietveld refinement of these samples.

Table 3.1: Unit cell (being **a**, **c** and **V** the cell lengths and volume, respectively), ion coordinates and fitting parameters obtained in Rietveld refinement method. The deviation is contained within parentheses.

Sample	Lattice parameters	Ion	x	y	z	Refinement parameters
	$a = 5.571(4)\mathring{A}$	Bi^{3+}	0	0	0	$R_{wp} = 16.88\%$
BFO-640	$c = 13.845(1)\mathring{A}$	Fe^{3+}	0	0	0.229200	$R_p = 11.82\%$
	$V = 429.755(6)\mathring{A}^3$	O^{2-}	0.843989	1.3053564	0.941033	$\chi^2 = 2.652$
	$a = 5.572(9)\mathring{A}$	Bi^{3+}	0	0	0	$R_{wp} = 17.00\%$
BFO-620	$c = 13.852(5)\mathring{A}$	Fe^{3+}	0	0	0.225642	$R_p = 12.89\%$
	$V = 430.221(4)\mathring{A}^3$	O^{2-}	0.485691	0.005324	0.913018	$\chi^2 = 2.253$
	$a = 5.571(1)\mathring{A}$	Bi^{3+}	0	0	0	$R_{wp} = 17.19\%$
BFO-600	$c = 13.845(2)\mathring{A}$	Fe^{3+}	0	0	0.227542	$R_p = 12.19\%$
	$V = 429.716(1)\mathring{A}^3$	O^{2-}	2.517060	0.461911	0.737292	$\chi^2 = 2.673$
	$a = 5.571(9)\mathring{A}$	Bi^{3+}	0	0	0	$R_{wp} = 19.00\%$
BFO-580	$c = 13.843(8)\mathring{A}$	Fe^{3+}	0	0	0.221200	$R_p = 14.17\%$
	$V = 426.797(4)\mathring{A}^3$	O^{2-}	0.445000	0.018000	0.950300	$\chi^2 = 2.681$

To evaluate the influence of crystallization temperature on the cell parameters and their corresponding volume, an analysis was conducted by plotting these parameters and volumes as a function of the crystallization temperature. The resulting graphical representation, shown in Figure 3.1(b), provides insights into how variations in crystallization temperature affect the structural dimensions of the unit cells. We observed that BFO-620 has presented maximum values in all parameters. However, when it comes to

the unit cell volume, we observed that sample BFO-600 presents a minimum value.

To evaluate the accuracy of the refinement and estimate the average size of crystallite and microstrain, we plotted Williamson-Hall's curves (WH) (as discussed in Section 2.2), in Figure 3.2, using the angles of the deflected peaks, full width at half maximum determined in the refinement, slope and intercept of WH curves.

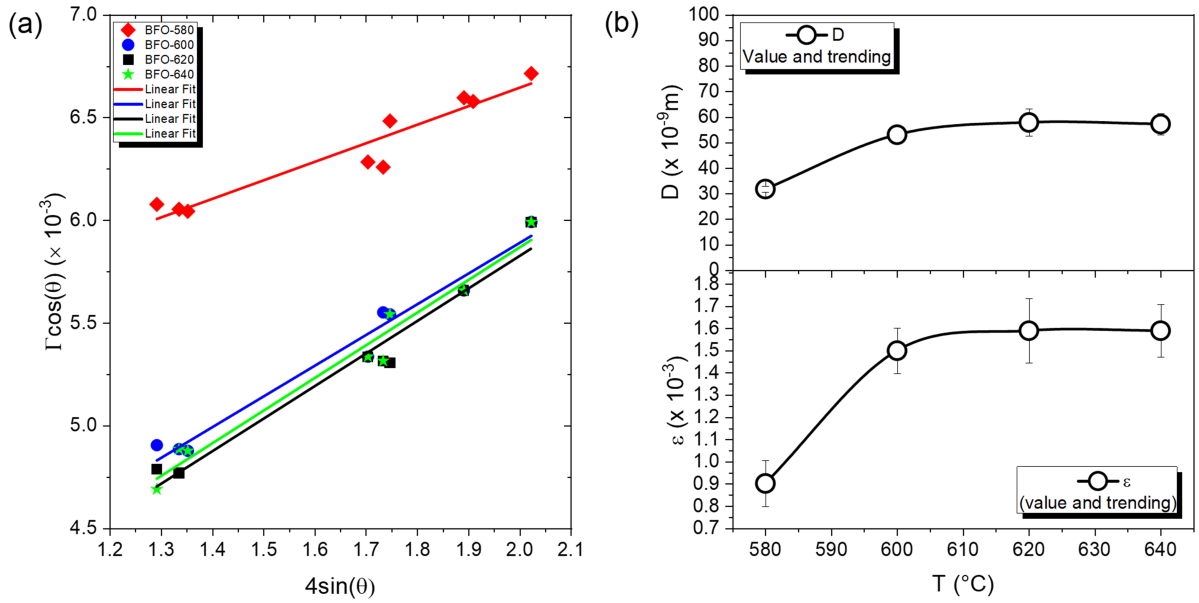

Figure 3.2: (a) Williamson-Hall's curve of the samples. The points are the respective calculated from Equation 2.2, and the segment is the straight-line fit. (b): microstrain (ε) and average crystallite size (D) estimated by the linear fitting as a function of the crystallization temperature. The lines are guides for the eyes

The points in the WH curves exhibit a straight-line behavior, indicating that the refinement closely matches the experimental data. However, a dispersion of points around the straight-line fitting suggests that the refinements are not fully optimized. An estimation of the average crystallite size and microstrain is provided in Table 3.2.

Table 3.2: Values of microstrain (ε) and average crystallite size (D) obtained through the linear adjustment of WH curves.

SAMPLES	ε	**D (nm)**
BFO-640	$(1.5 \pm 0.1) \times 10^{-3}$	57 ± 4
BFO-620	$(1.6 \pm 0.1) \times 10^{-3}$	58 ± 5
BFO-600	$(1.5 \pm 0.1) \times 10^{-3}$	53 ± 3
BFO-580	$(9 \pm 1) \times 10^{-4}$	32 ± 1

Sample BFO-580 has shown a minimum in both microstrain and average crystallite size, and the values are increased in BFO-600 and are maintained almost constant

until BFO-640. Such behavior indicates that the microstrain and average crystallite size establish above 600 °C of crystallization temperature in our samples. Even though the Rietveld refinements are not adequately adjusted, all values estimated here are agreed to the reports in the literature [45, 107]. To observe the structure of samples, we simulated the crystal structure in software Vesta using the .cif (Crystallographic Information Framework File), generated from GSAS after done refinement, as shown in Figure 3.3. Figure (a), (b), (c) and (d) are the crystal structure of BFO-580, BFO-600, BFO-620 and BFO-640, respectively.

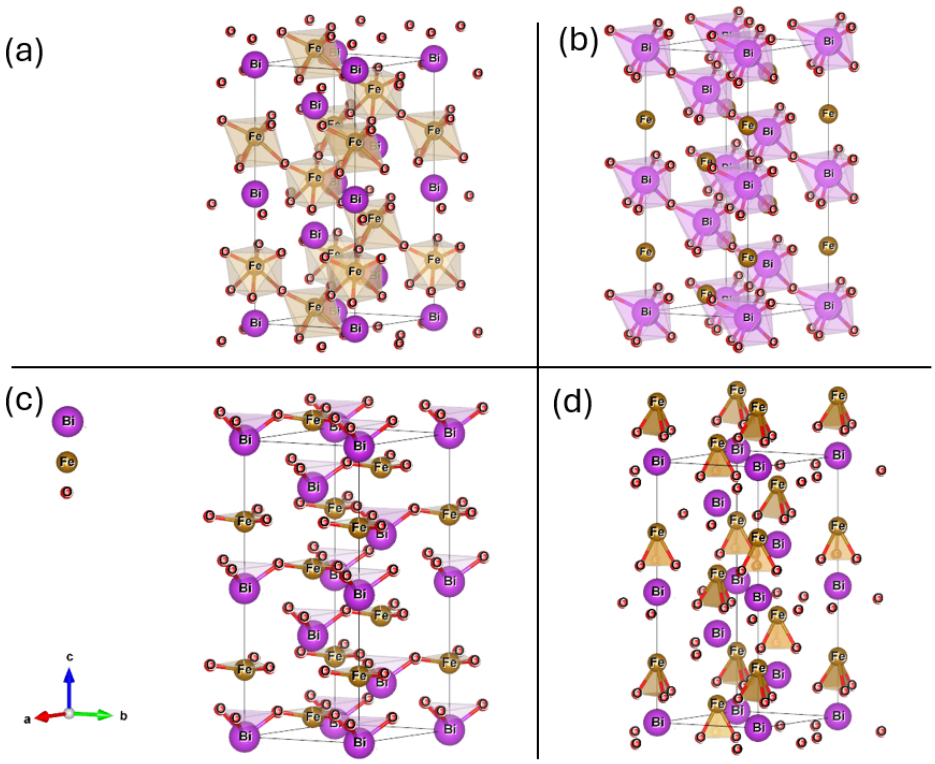

Figure 3.3: Crystal structure of $BiFeO_3$ samples simulated in Vesta Software. (a): is the structure of sample BFO-580 (b): BFO-600, (c): BFO-620, and (d): BFO-640.

As a complementary technique, Raman Scattering Spectroscopy (RSS) spectra are presented in Figure 3.4(a). Three prominent peaks are observed at low wavenumbers around 133, 142, and 172 cm^{-1}, corresponding to the Fe–O bonding mode (E) near 133 cm^{-1}, and the Bi–O bonding modes (A_1) near 142 and 172 cm^{-1}. The BFO-500 sample did not exhibit any well-defined peaks associated with the active modes of BFO. Regarding other active modes, none were clearly defined in the spectra, even after repeating the measurements and adjusting the focus region of the surface. However, slight protuberances can be observed near the marked lines, which correspond to the regions predicted for existing active modes.

Aiming to investigate the protuberances, we deconvoluted the spectra using a Lorentzian function, with the blue and green areas representing the Bi–O and Fe–O

bonds, respectively, and the final fitting shown as the red line.

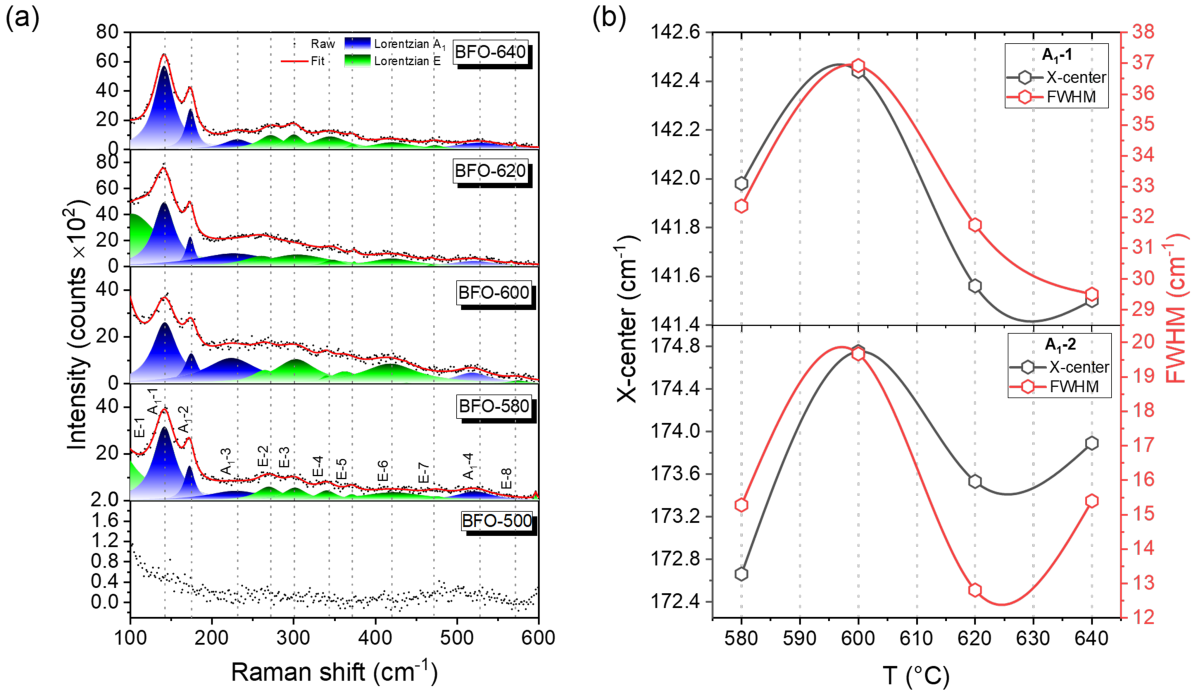

Figure 3.4: (a): Raman Scattering Spectroscopy patterns of the samples: the points represent the experimental data, the red lines show the fitted data, and the shaded areas correspond to the Lorentzian fits. The blue areas indicate the Bi–O bonds, indexed as A_1 (the following number after the mode name is only to distinguish each mode), while the green areas represent the Fe–O bonds, indexed as E. (b): Fit parameters, including X-center (peak position) and FWHM (band width), of the core peaks as a function of crystallization temperature. Detailed values are provided in Table 3.3, and the lines are guides for the eyes.

Tables A.1 and A.2 present all parameters obtained from the Lorentzian fits of the Raman spectra. While all parameters (position, full width at half maximum, area, and height) are provided, our analysis focuses on the position and band length of the core peaks for comparison purposes, as summarized in Table 3.3[1]. The corresponding data points and trends are plotted in Figure 3.4(b).

The observed peaks are clearly shifted to lower frequencies compared to the expected wavenumber. This displacement, known as the Raman shift, is attributed to the residual strain between the material ($BiFeO_3$) and the substrate ($Pt/TiO_2/SiO_2/Si(100)$) [108, 109]. Higher strain typically causes a shift to higher frequencies, as increased strain significantly affects bonding and distorts the material's structure, leading to greater vibrational amplitudes. Based on the values in Table 3.3, the samples with core peaks shifted to lower frequencies indicate lower residual strain compared to what is reported for other architectures (e.g., bulk) and substrates in the literature, such as $SrTiO_3$ and

[1]Although the first three expected peaks above 100 cm^{-1} are observed, we focus on peaks A_1-1 and A_1-2, as only BFO-620 yielded fit values within the experimental analysis range.

$LaNiO_3$-coated $SrTiO_3$(001) [76, 77, 79]. On the other hand, the band width of the peaks (spectroscopy line broadening, FWHM) can qualitatively provide insights into defect concentrations, such as the mismatch between the material and substrate, lattice vacancies (e.g., bismuth and oxygen vacancies), and local lattice disorder in the film [108, 110, 111]. As shown in Figure 3.4(b), the relationship between these parameters and crystallization temperature reveals that the maximum values are observed at 600 °C. But also, these curves suggest that both residual strain and defects, such as deficiencies, play significant roles in influencing the Raman shift. Yang *et al.* [79], studying BFO as a function of the substrate and atmosphere, observed the reverse trend in their plots. They attributed this to lattice vacancy concentrations being the dominant factor affecting the microstructure, rather than residual strain.

Table 3.3: Position (**Xc**) and the band length (**FWHM**) of the core peaks in Raman spectra. The values in x_0 are the initial values supplied to the algorithm, as cited in 2.4. All values are in cm^{-1}.

Peak	x_0 [76, 77]	**BFO-580**	**BFO-600**	**BFO-620**	**BFO-640**	
E-1	136	< 100	< 100	102.40	< 100	**Xc**
A_1-1	147	141.98	142.44	141.56	141.50	
A_1-2	176	172.66	174.75	173.53	173.89	
E-1	-	-	-	80.54	-	**FWHM**
A_1-1	-	32.36	36.92	31.75	29.50	
A_1-2	-	15.27	19.66	12.80	15.39	

Regarding the structural characterization discussed thus far, X-ray diffraction analysis combined with Rietveld refinements provided the crystalline structure and space group ($R\bar{3}c$) of the samples, except for BFO-500, which showed coexistence with sillenite, mullite, and iron oxide phases. The WH curve plots exhibited a straight-line behavior, despite some dispersion of points around the linear fit, suggesting that the Rietveld refinements were not fully optimized. Although the estimated microstrain and average crystallite size align with values reported in the literature, this dispersion indicates that the property trends may not be entirely precise. As a result, there is no direct correlation between the microstrain observed in the WH curves (Figure 3.2(b)) and the trends in Raman shift (Figure 3.4(b)), especially when considering other mechanisms contributing to microstrain and residual strain. Despite these inconsistencies, these techniques (XRD, refinements and RSS) have served their purpose in this dissertation, providing crucial and precise information about the crystalline structure and space group.

3.2 X-ray photoelectron spectroscopy analysis

The X-ray photoelectron spectroscopy (XPS) survey of the samples is shown in Figure 3.5(a). While we identify the core peaks in the survey, we focused in detail on the chemical states of Bi 4f, Fe 2p, and O 1s, which include Bi $4f_{7/2}$ and Bi $4f_{5/2}$, Fe $2p_{3/2}$ and Fe $2p_{1/2}$, respectively. The C 1s peak is used for calibration and binding energy correction. It is important to note that XPS measurements provide information only about the compounds on the material's surface, so all discussions in this section pertain specifically to the surface of our samples. However, for thin films, we can correlate these surface analyses to the bulk material, with the understanding that the diffusion of defects on the surface is more pronounced. Figures 3.5(b) and (c) show the chemical states of bismuth 4f (from 155 to 169 eV) and oxygen 1s (from 527 to 533 eV) spectra from the survey, where O_I is referred to the oxygens in the lattice, and O_{II} is related to the oxygen vacancies [112–114].

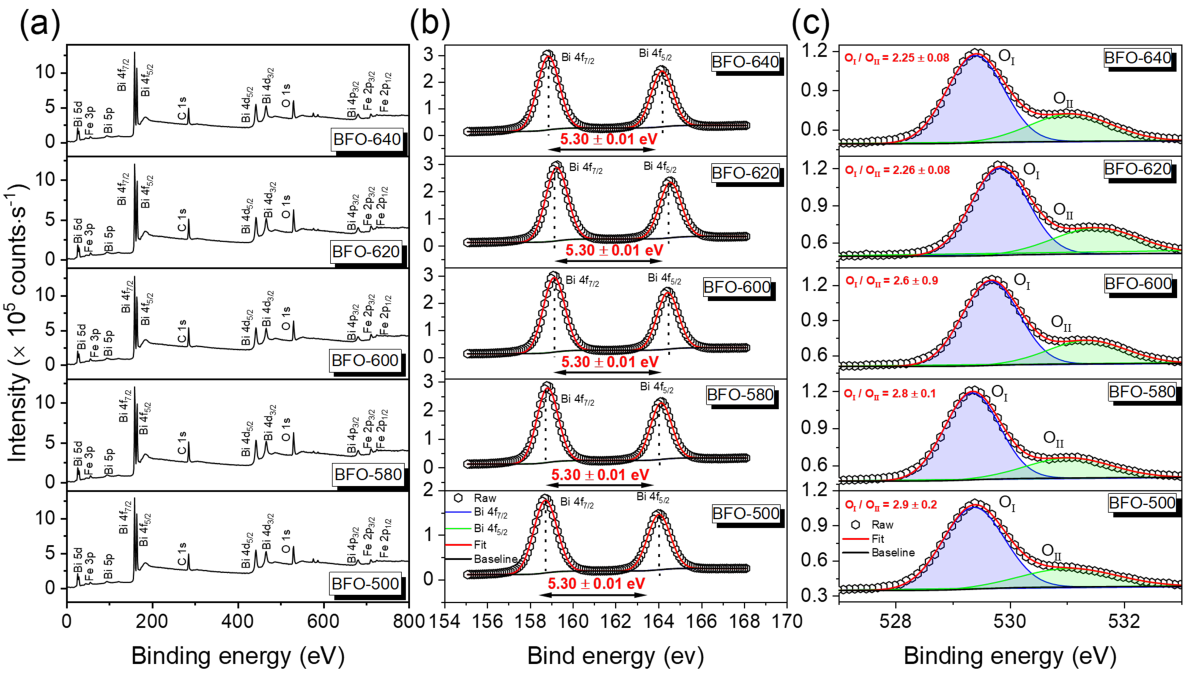

Figure 3.5: (a): X-ray Photoelectron Spectroscopy survey of samples. (b): XPS spectra of chemical state of Bi 4f, and (c): O 1s.

The binding energy separating Bi $4f_{7/2}$ and Bi $4f_{5/2}$ for all samples was determined[2] to be (5.30 ± 0.01) eV, indicating the presence of Bi^{3+} in the lattice and confirming the valence state of bismuth according to the stoichiometry [114–117]. The separation was determined by fitting Gaussian functions to the peaks and using the x-center parameter of each peak to calculate the deviation. The Figure 3.5(c) exhibits the relationship

[2]In this section (3.2), all deviation and error propagation belong to the adjustment, not the experimental data.

between the oxygen into the lattice (O_I) and oxygens vacancies, and Table 3.4 brings all ratio between O_I and O_{II}, the ratio between Fe^{3+} and Fe^{2+}, and their respective deviation obtained through gaussians fits.

Table 3.4: Calculated ratios between oxygen in lattice and oxygen vacancies concentration (O_I/O_{II}), and between Fe^{3+} and Fe^{2+} concentrations.

SAMPLES	O_I/O_{II}	Fe^{3+}/Fe^{2+}
BFO-640	2.2 ± 0.1	1.5 ± 0.2
BFO-620	2.3 ± 0.1	1.5 ± 0.1
BFO-600	2.6 ± 0.9	1.9 ± 0.2
BFO-580	2.8 ± 0.1	1.3 ± 0.1
BFO-500	2.9 ± 0.2	1.5 ± 0.1

It is important to note that the calculated uncertainties were derived from the values obtained from the fits. Even with this approach, it remains challenging to determine, even qualitatively, the concentration of oxygen vacancies. Therefore, we developed a defect equation based on physicochemical principles to estimate the ideal oxygen vacancy concentration, which is inferred from the iron reduction, as follows.

The possible point defects of $BiFeO_3$ are:

$$\text{null} \rightleftharpoons V_{Bi}^{'''} + Bi_i^{\cdots},$$

$$\text{null} \rightleftharpoons V_O^{\cdot\cdot} + O_i^{''},$$

$$\text{null} \rightleftharpoons V_O^{\cdot\cdot} + O_{gb}^{''},$$

$$\text{null} \rightleftharpoons V_O^{\cdot\cdot} + O_s^{''}.$$

Then,

$$\text{null} \rightleftharpoons V_{Bi}^{'''} + V_{Fe}^{'''} + 3V_O^{\cdot\cdot},$$

$$\text{null} \rightleftharpoons V_{Fe}^{'''} + Fe_i^{\cdots},$$

$$\text{null} \rightleftharpoons V_{Fe}^{'''} + Fe_{gb}^{\cdots},$$

$$\text{null} \rightleftharpoons V_{Fe}^{'''} + Fe_s^{\cdots},$$

$$Fe_{Fe}^{x} + e' \rightleftharpoons Fe_{Fe}^{'},$$

$$2O_O^{x} \rightleftharpoons O_2(g) + 2V_O^{\cdot\cdot} + 4e',$$

$$\text{null} \rightleftharpoons 4\text{Fe}'_{\text{Fe}} + 2\text{V}_{\text{O}}^{\cdot\cdot} + \text{O}_2(\text{g}). \tag{3.1}$$

All notations used here follow the Kröger-Vink notation [118], which describes the defect (main symbol), the defect's position (subscript), and its charge (superscript). Therefore, we can qualitatively correlate some properties of the samples with the concentrations of oxygen in the lattice, its vacancies, and the reduction of Fe^{3+} to Fe^{2+} [113]. Figure 3.6(a) presents the iron spectra from the survey and their fits containing the calculated iron reduction, and (b) the comparative ratios between Fe^{3+}/Fe^{2+} and oxygen vacancies (ideal and experimental):

In Figure 3.6(a), the main peaks are around 710 and 723 eV separated by 13.68 eV for BFO-500, 13.69 eV for BFO-580, 13.70 eV for BFO-600 and BFO-620, and 13.41 eV for BFO-640, the most distinct, although they confirm the coexistence between Fe^{3+} and Fe^{2+} [114, 117, 119, 120]. There are satellite peaks separating the main ones, already reported, indicating possible reduction states of iron [121]. In Figure 3.6(b), it is plotted the ratio between the oxygen in lattice and its vacancies (from fit and ideal[3]) and the iron reduction as a function of the crystallization temperature. We observe that BFO-600 presents less iron reduction and BFO-580 was the sample with the largest reduction. Thus, "ideal" oxygen concentration should follow the same relation, i.e., BFO-600 should have less oxygen vacancies concentration and BFO-580 more oxygen vacancies concentration, as ideal curve. However, through fit from oxygens chemical states ("experimental" vacancies concentration), BFO-500 showed less oxygens vacancies concentration and BFO-640 more oxygens vacancies, in addition a gradually increasing of oxygens vacancies concentration as a function of temperature.

As discussed in Chapter 1, Section 1.2.2, the origin of the leakage current in $BiFeO_3$ ceramics is commonly attributed to defects such as bismuth and oxygen vacancies [113], and iron reduction [29]. Considering the limitations of the XPS technique and the defects estimated using Kröger-Vink notations, we will focus on the curves for iron reduction and the ideal oxygen vacancy concentration shown in Figure 3.6 and Equation 3.1. This approach was chosen due to the clear difficulty in experimentally quantifying oxygen, while quantifying iron in materials is more straightforward. Therefore, analyzing the oxygen vacancy ratio based on the theoretical calculation in Equation 3.1 offers a more accurate estimation[4].

[3] By "ideal", we mean that these values of oxygen vacancies concentrations were calculated through the Equation 3.1. Therefore, in an analogical way, "experimental" oxygen vacancies concentration refers to the fit curve of O_I/O_{II}.

[4] A more detailed discussion of these point defect concentration curves will be provided in the final Section 3.8, where the results will offer additional insights for their physical interpretation.

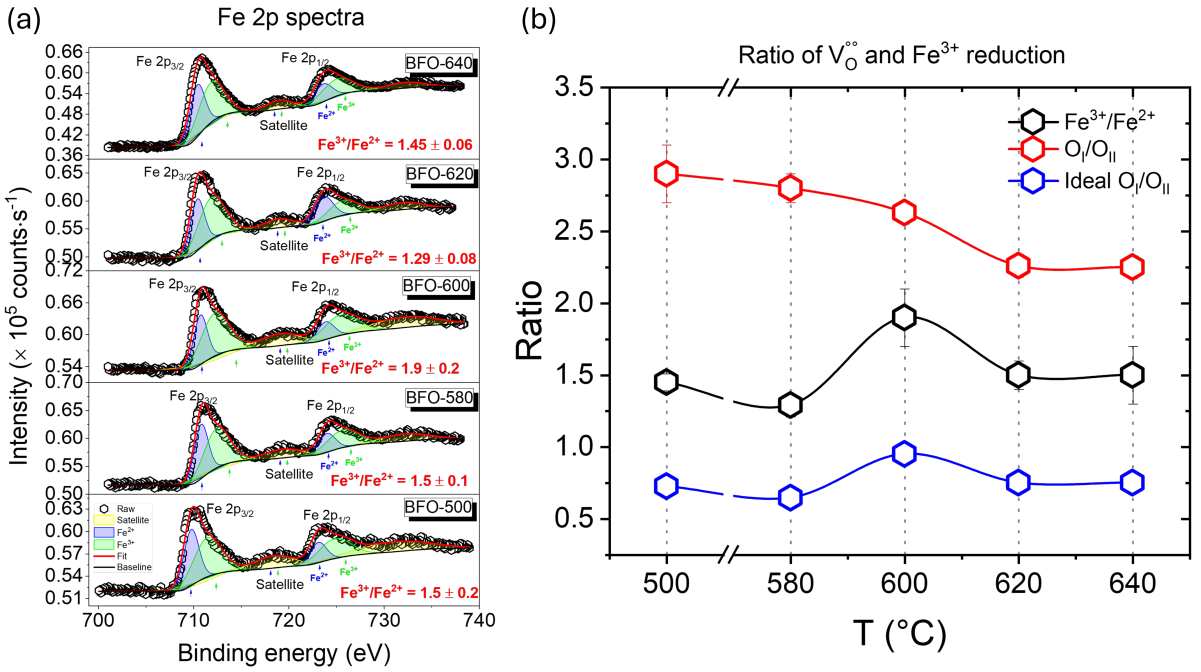

Figure 3.6: (a): Iron chemical state spectra from the survey and their respective fit. The open symbols are the experimental data, the final adjustment is represented by the solid red line, and the chemical state Fe^{3+}, Fe^{2+} and satellite are, respectively, presented by the shaded areas of blue, green and yellow. (b): Ratios of O_I/O_{II} ratios from fits (red) and ideal (blue) calculation, and iron reduction (black) rate as a function of the crystallization temperature, and the lines are guides for the eyes.

3.3 Microscopy analysis

In Section 2.3, we discussed that we did not sputter the samples with gold to preserve them for future measurements, so as not to "destroy" the samples. As a result, the images were not of sufficient quality to clearly observe the grains and topography in detail. All figures are provided in Appendix B. Despite these limitations, we were able to estimate some important parameters from the samples, facilitated by the conductive gold electrodes and the backscattered mode of SEM. These parameters, including the sample thickness and electrode area, were essential for converting the i-V data to J-E (electric current to current density, and voltage to electric field). Additionally, they contributed to a more accurate determination of the parameters in the equivalent electric circuit model in impedance spectroscopy (IS). The estimations of parameters are in Figure 3.7.

Although fluctuations in thickness were observed (view Figure 3.7(a-e)), they do not significantly affect the conversion process or interfere with the studies, as the dispersion is not considerable in comparison to the expected. The electrode areas (view Figure 3.7(f)) were found to be in close agreement with the calibration of the dark mask used during deposition. This deviation is minimal and does not impact the validity of the results.

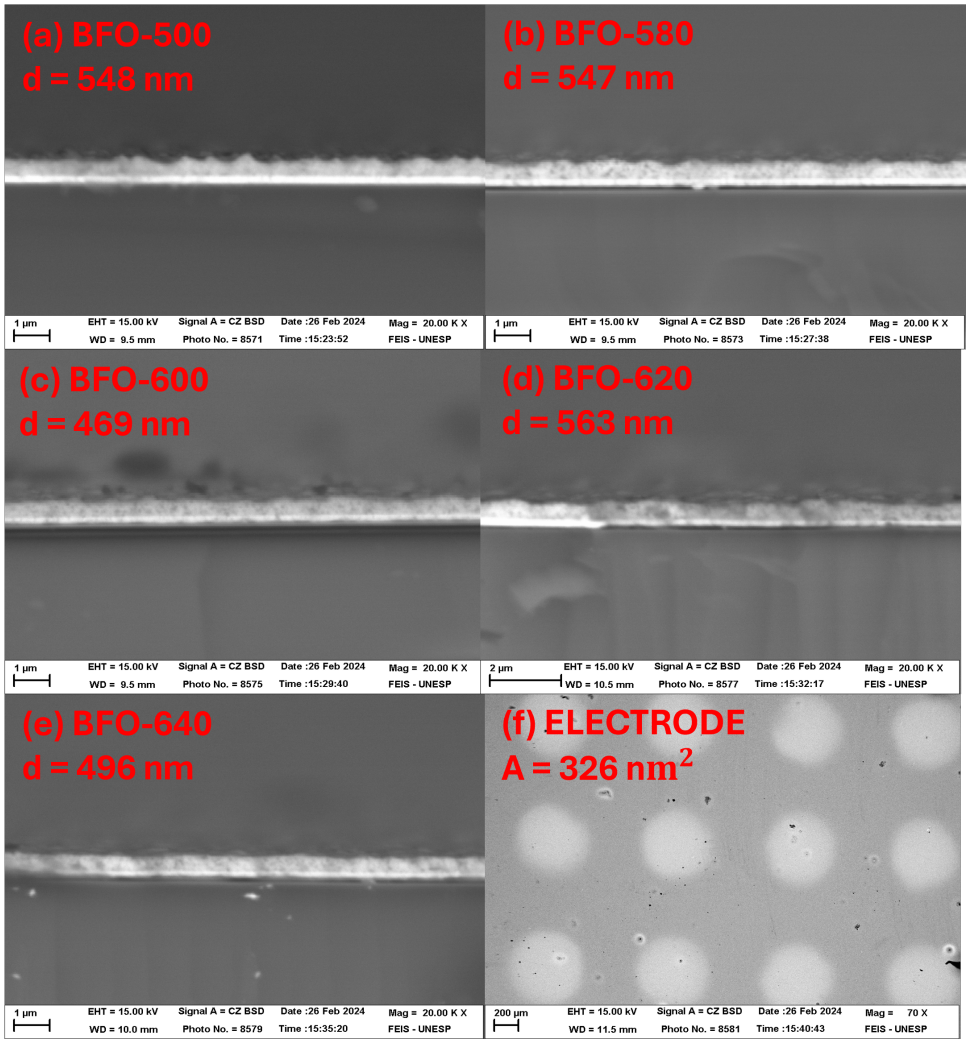

Figure 3.7: (a-e): Thickness (d) of samples collected in backscattered mode of SEM. (f): The electrode area (A) was estimated from SEM images of sample BFO-600, which serves as a representative sample.

3.4 Growth kinetics

With structural characterizations, the presence of secondary phases was observed at 500 and 640 °C. However, between these temperatures, single-phase bismuth ferrite was formed. These analyses motivated this study to investigate how the perovskite phase formation process occurs, including its formation stages, interactions with secondary phases, and formation rate, among other factors. This section addresses the reaction kinetics of $BiFeO_3$ thin films.

Another set of samples was prepared, but this time, pyrolysis was performed at 400 °C. As observed in Figure 3.1(a), the BFO-500 sample had already initiated its formation process; therefore, 400 °C was chosen as the pyrolysis temperature.

Initial studies were performed to investigate the evolution of crystalline phases in BFO thin films under isothermal treatments, using X-ray diffraction data to follow the

evolution of the crystalline phases. Figure 3.8(a) shows the XRD patterns of BFO thin films heat annealed at 600 °C for time annealing from 0 to 12 minutes. In this figure, the XRD pattern of the BFO film pyrolyzed at 400 °C (without heat annealing) shows a typical shape of an amorphous material. The evolution of the XRD patterns in Figure 3.8(a) shows a quick crystallization of the perovskite phase in the $BiFeO_3$ film. After only about 1 minute at 600 °C, intense (012), (104), and (110) reflections suddenly appeared at around 22.5° and 32.0°, clearly indicating the formation of the rhombohedral (space group $R3\bar{c}$) perovskite phase of $BiFeO_3$. Furthermore, the low-intensity peaks at around 24 and 30° indicate the presence of small amounts of secondary phases, possibly attributed to ferrite (Fe_2O_3) and sillenite ($Bi_{12}FeO_{20}$ or $Bi_{25}FeO_{40}$) phases. More on the formation of these and other secondary phases is discussed later. Increasing the thermal treatment time leads simultaneously to the disappearance of peaks associated with secondary phases and an increase in the peaks of the perovskite phase. From the process's perspective, the results suggest, at these synthesis conditions, that the perovskite phase is formed either by nucleation and growth of crystals from the initial non-crystalline phase or by reaction between the secondary phases. Since the non-crystalline phase is the only phase present since the start, we expect nucleation and growth to be the dominant process. It is the most likely scenario when considering that the second option would require the formation of intermediate crystalline phases, which doesn't seem to be kinetically feasible in so little time.

To better understand the crystallization kinetics of the perovskite phase in pure BFO, we conducted kinetic modeling of XRD data. To do so, we extracted the perovskite peak areas (integrated intensities) at each time. With these data, we then defined the converted fraction of the perovskite phase (α) as $\alpha = (A - A_{min})/(A_{max} - A_{min})$, where A, A_{min}, and A_{max}, are the sum of peak areas at a given time and the minimum (initial) and maximum (final) obtained sum of areas, respectively. We used the sum of areas of all perovskite peaks to mitigate eventual orientation effects during the thermal treatment. Figure 3.8(b) shows the time dependence of the converted fraction of the perovskite phase (α) of pure BFO film heat annealed at 600 ºC, constructed based on XRD patterns shown in Figure 3.8(a), indicating that the transformed fraction increased until approximately 3 minutes steeply, and then slowly until the end of the reaction. The modeling of this data was best fitted with a second-order reaction law, such that $\alpha = kt/(1 + kt)$, where k is the reaction rate constant at a given temperature. It suggests that the rate-limiting step depends on the reaction or aggregation of two chemical species. Since oxygen is expected to be abundant in the reaction media, we infer the two chemical species to be the Bi^{3+} and Fe^{3+} ions of the same concentrations, dispersed along the non-crystalline phase.

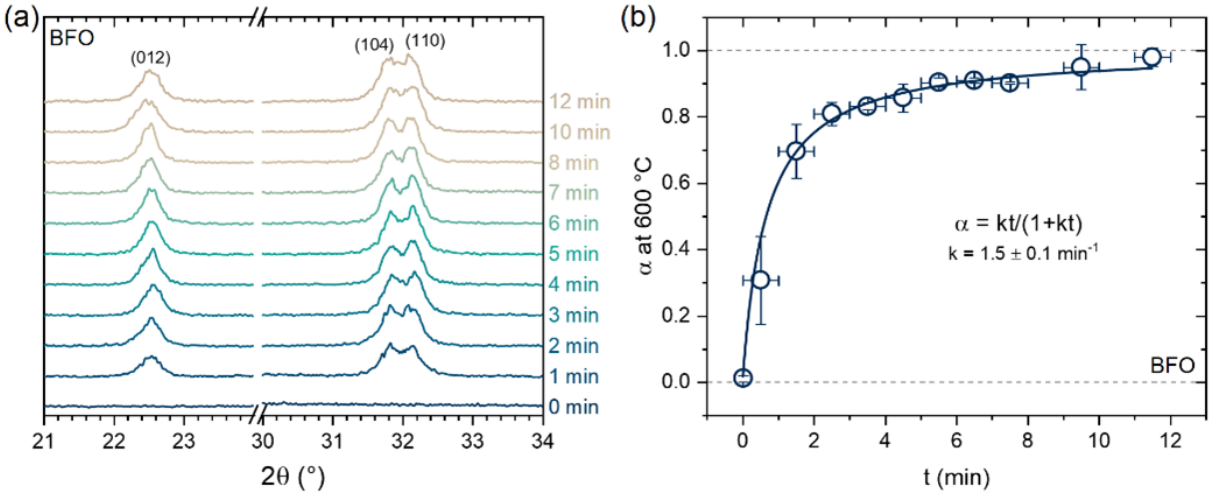

Figure 3.8: (a): Time dependence of XRD patterns of pure BFO thin films and (b): the converted fraction of the perovskite phase (α) at 600 °C. The α values shown are the mean between two sequential times. The line represents the theoretical fit considering a second-order reaction law.

An additional isothermal study of the crystallization kinetics was also performed on another sample (virgin) to gain more insight into the formation of secondary phases in these systems. For this purpose, these films were thermally annealed at 400 °C at a fixed temperature from 0 to 80 hours. Figure 3.9(a) shows the XRD patterns of virgin BFO thin films at thermal treatments at 400 °C for different times. The XRD patterns time evolution of BFO film (Figure 3.9(a)) again indicates that the structure of the as-prepared BFO thin film (only pyrolyzed at 400 ºC) is composed initially of non-crystalline phases, and a small portion of a crystalline phase, possibly mullite (composition $Bi_2O_3.2Fe_2O_3$ or $Bi_2Fe_4O_9$), given characteristic peak of reflection by planes M: (121) + (211) of this phase. Over the course of treatment, the diffractograms' profiles are maintained approximately constant until 8 h of thermal treatment. However, heat treatments above 8 hours change the structure with the appearance of additional crystalline phases. From thermal treatments from 8 to 22 h, new peaks arise, being F: (012) at ≈ 23.5° related to the ferrite (Fe_2O_3) in a rhombohedral phase of space group R3$\bar{c}$, S: (222) at ≈ 30.5° related to sillenite ($Bi_{12}FeO_{40}$ or $Bi_{25}FeO_{40}$) in cubic phase of space group I23, and P1: (012) and P2: (104) + (110) at respectively ≈ 22.5 and ≈ 32.0° of perovskite (BFO) in a rhombohedral phase of space group R3$\bar{c}$. From 22 to 80 h of thermal treatment, the intensity of peaks P1, F, S and P2 increase with the reduction of M and the apparent decrease of the non-crystalline phase band. In equilibrium conditions, the stable phase is the perovskite, formed only after a long treatment, whereas the first crystalline phase formed is mullite. It indicates that the development of phases is kinetically controlled in the experimental conditions employed. It corroborates the initial results that when BFO thin films are thermally treated at 600 °C for 1 minute, perovskite is the first crystalline phase formed. Although perovskite is chemically less complex than mullite,

the crystallization of mullite requires aggregation of fewer atoms to form its unit cells than perovskite, which can lead to the formation of mullite comparatively faster. The eventual transformation of mullite in perovskite, which has stoichiometry proportions of bismuth and iron, must occur concurrently with the secondary phase formation, especially Bi-rich sillenite because mullite is Fe-rich. Nevertheless, it is interesting to notice that from 8 to 22 h, the intensity of perovskite peaks increases abruptly, while mullite's remain almost constant. Parallelly, peaks of sillenite and ferrite also increase abruptly. These observations show that, during the isothermal treatment, the perovskite, ferrite, and sillenite phases can be formed by the decomposition of mullite and crystallization from non-crystalline phases. Goldman *et al.* [122] exploring the reaction pathway in the hydrothermal growth of phase-pure bismuth ferrites, have observed that the intermediates products that lead to a pure-phase BFO are a mixture of crystalline selenite, amorphous material, and some unidentified crystalline phases. Thus, the configuration of BFO formation seems to agree with this work, although we used different solvents and chemical synthesis techniques.

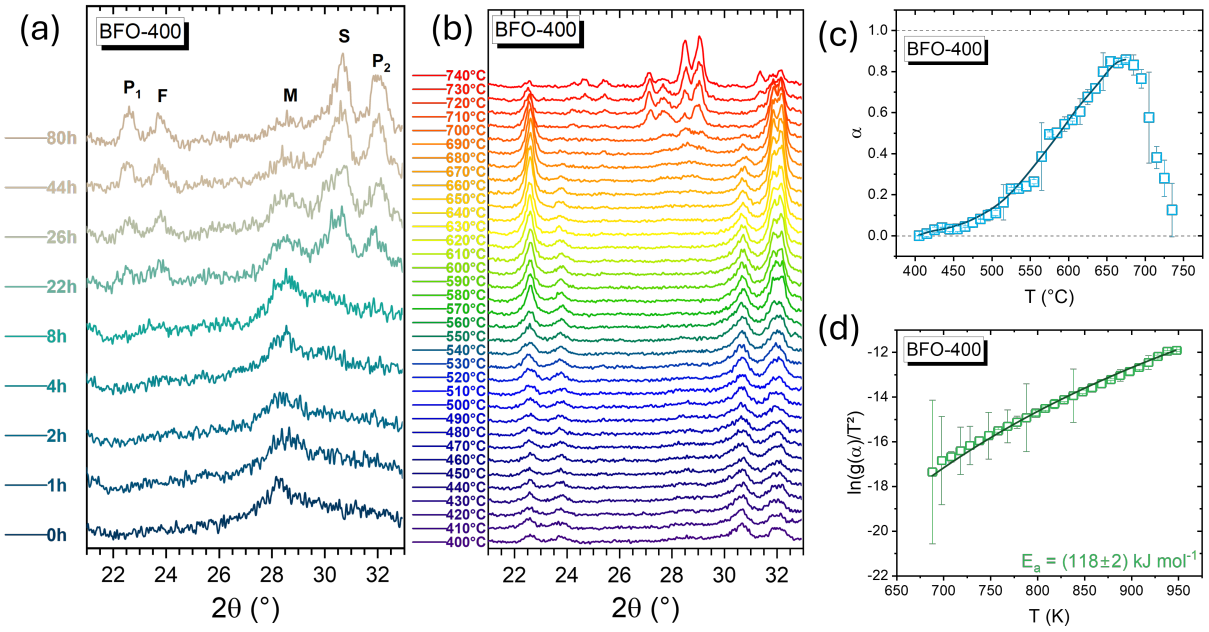

Figure 3.9: (a): XRD patterns of virgin BFO thin film at isothermal thermal treatments at 400 °C for different times from 0 to 80 hours. Possible attributions are P1: (012) of BFO (perovskite), F: (012) of Fe_2O_3, M: (121) + (211) of $Bi_2Fe_4O_9$ (mullite), S: (222) of $Bi_{12}FeO_{20}$ or $Bi_{25}FeO_{40}$ (sillenite), P2: (104) + (110) of BFO (perovskite). (b): XRD patterns of BFO thin film heat annealed in a non-isothermal regime at different temperatures and heating rate of 1 °C/min. (c): Fractions of formed perovskite phase (α) as a function of temperature under constant heating of BFO film. The line is generic fit with a smooth function (weighted average of 5 points) in the region of interest for kinetic modeling. (d): Transformed data to fit with the kinetic models.

The kinetic of crystalline phase formation in BFO films was also studied under a non-isothermal regime. So, from pyrolyzed pure BFO thin film at 400 °C at 10 min, a

new set of samples was prepared heat treating the film increasing the temperature from 400 to 740 °C with a heating rate of 1 °C/min, and performing XRD measurements at each temperature separated by a 10 °C step. Figure 3.9(b) shows the obtained XRD patterns of BFO thin films heat annealed in a non-isothermal regime at different temperatures. In the Figure 3.9(b), the last stage profile of the isothermal regime was maintained until 690 °C, with a reservation that perovskite peaks increase and secondary phases decrease. As previously discussed, one hypothesis of perovskite formation is at the cost of non-crystalline phases and due to the decomposition/reaction of secondary phases. However, a subtle formation of four peaks around 27 and 29° was observed from 650 °C, which grew abruptly from 700 °C while perovskite peaks degrade. It suggests that these phases form at the cost of perovskite, probably due to the volatilization of bismuth since there is enough energy to break bonds of Bi species and evaporate [15, 27]. This phenomenon entails iron-rich phase re-formation on what supports the hypothesis of Bi absence. This phenomenon was also observed in similar works , such as one mixing bismuth (Bi_2O_3) and iron oxides (Fe_2O_3), where increasing the time spent on the reaction causes the total conversion of perovskites to mullite phase ($Bi_2Fe_4O_9$). Based on conservation mass law, at this temperature or spent time of reaction, it is supplied enough energy to break bismuth bonds of solid and favor the iron-rich phase from the equilibria diagram possible formations, which in these conditions, it has become the thermodynamically stable phase [123]. Xu *et al.* observed the competition of secondary phases as a function of temperature treatment between the BFO phase, mullite, and oxides [124].

A quantitative description of the perovskite phase formation kinetics of the different studied thin films under non-isothermal regimes was also obtained by fitting the time/temperature-dependent XRD data using typical solid-state kinetic models [125, 126]. Instead of using model-free approaches [127, 128], reaction-specific models were used in the present work to observe whether the kinetics in the sample may differ and if additional insights can be collected, from the already observed. The advantages and disadvantages in each case were thoroughly discussed in the literature [129, 130]. In the present work, the perovskite peak areas at each time/temperature were quantified using the same procedure to obtain the converted fraction α of the perovskite phase. Figure 3.9(c) shows the temperature dependence of the fractions of perovskite phase (α) of BFO thin film. In Figure 3.9(c), the aforementioned behaviors of perovskite phase being formed and promptly increase with the non-isothermal treatment, with a later reduction possibly due to solid-state decomposition of the perovskite into secondary phases. The analysis was restricted to the temperature range between the onset of α increase and the point at which α begins to decay due to phase decomposition, to perform the actual kinetic modeling of the perovskite phase formation.

In non-isothermal experiments, the general differential form of α concerning

the temperature is given by [123, 129] $d\alpha/dT = (A/\beta)f(\alpha)exp(-E_a/RT)$, where A is the pre-exponential (frequency) factor, β the heating rate, $f(\alpha)$ the reaction model, E_a the activation energy of the rate-limiting step, and R the gas constant. The integral function $g(\alpha)$ is related to $f(\alpha)$ by,

$$g(\alpha) = \int_0^{\alpha} [f(\alpha)]^{-1}\, d\alpha,$$

which, after some minor algebra, leads to,

$$g(\alpha) = \left(\frac{A}{\beta}\right) \int_0^{T} exp\left(-\frac{E_a}{RT}\right) dT.$$

The information on what kinetic law is operating in each solid-state process is contained in $f(\alpha)$ and $g(\alpha)$, which were solved for several initial boundaries and geometric conditions. The tested models are summarized in Table 3.5.

Table 3.5: Integral functions of reaction kinetic models tested to fit the experimental data collected under non-isothermal conditions.

Group	Model	Symbol	$g(\alpha)$
Nucleation	Second-order power law	P2	$\alpha^{1/2}$
	Third-order power law	P3	$\alpha^{1/3}$
	Fourth-order power law	P4	$\alpha^{1/4}$
	Avrami-Erofeyev	A2	$[-\ln(1-\alpha)]^{1/2}$
		A3	$[-\ln(1-\alpha)]^{1/3}$
		A4	$[-\ln(1-\alpha)]^{1/4}$
Geometrical contraction	Contracting area	R2	$1-(1-\alpha)^{1/2}$
	Contracting volume	R3	$1-(1-\alpha)^{1/3}$
Diffusion	1D diffusion	D1	α^2
	2D diffusion	D2	$[(1-\alpha)\ln(1-\alpha)]+\alpha$
	3D diffusion	D3	$\left[1-(1-\alpha)^{1/3}\right]^2$
Reaction order	First-order	F1	$-\ln(1-\alpha)$
	Second-order	F2	$[1/(1-\alpha)]-1$
	Third-order	F3	$(1/2)\left[(1-\alpha)^{-2}-1\right]$

To fit the data and obtain the kinetic triplet, i.e., $g(\alpha)$, A and E_a, an explicit α vs T function must be derived, which demands calculating the last integral, that does not have an analytical solution. By using the Coats-Redfern [131] approximation, one approximate solution is,

$$\ln\left[\frac{g(\alpha)}{T^2}\right] = \ln\left[\left(\frac{AR}{\beta E_a}\right)\left(1-\frac{2RT}{E_a}\right)\right] - \frac{E_a}{RT}.$$

The procedure is to calculate the left part of the equation with experimental data using the different $g(\alpha)$ models, plot the results as a function of T, and fit the points with the right part of the equation. The obtained fits are given in Figure C.1 in Appendix C.

For solid-state reactions, there is no defined way to identify the most appropriate model to be used to interpret the experimental data. Here, the choice was made considering the adequacy of the model to the data, indicated by the R^2 value of the fits, and the assumption of the possible reactions that may occur. By both criteria, the most appropriate model for pure BFO was a second-order reaction model. The respective fits using these models are presented in Figure 3.9(d). The obtained A and E_a parameters from all kinetic models are presented in Figure C.2(a-b), also in Appendix C. As expected, the values are strongly dependent on the model employed [132]. Considering the obtained results, a possible interpretation for the adequate kinetic model of the films is connected to its compositions. In pure BFO films, the Fe^{3+} and Bi^{3+} cations combine with oxygen anions to form the $BiFeO_3$ perovskite phase, indicating that the rate-limiting step depends on both metal cation concentrations leading to the second-order reaction order. This result corroborates the model employed for phase formation kinetics for the isothermal treatment at 600 °C.

3.5 Dielectric characterization

The dielectric characterization involved measuring dielectric permittivity as a function of both the applied electric field's frequency and temperature. Impedance spectroscopy was used to obtain this data for the study.

Impedance Spectroscopy (IS) was performed over a range of frequencies and temperatures, specifically $100 \leq f \leq 1$ MHz and $400 \leq T \leq 500$ K (see Section 2.3). Figure 3.10(a) illustrates the real permittivity as a function of temperature. All samples exhibited a similar profile, although certain samples, such as BFO-620 and BFO-640, showed a more pronounced increase. In contrast, Figure 3.10(b) reveals that the imaginary permittivity increases sharply, by nearly two orders of magnitude. This behavior suggests that a non-Debye relaxation model is appropriate for all samples, as the observed relaxation time distribution is evident in the permittivity curves. To further emphasize the frequency dependence of permittivity, $\varepsilon(f)$ was plotted at different temperatures, as presented in Figures 3.10(c) and (d).

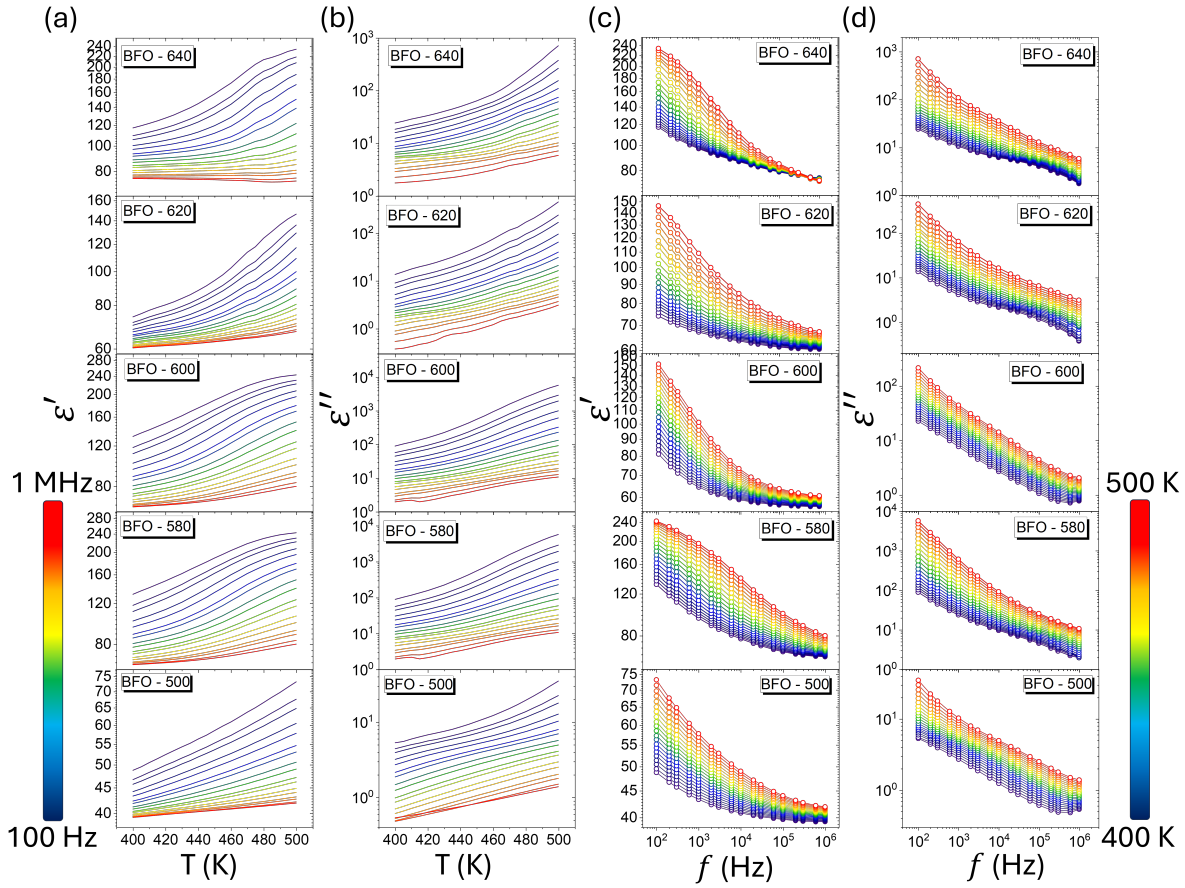

Figure 3.10: (a): Real permittivity (ε') as function of temperature, and (b): imaginary (ε'') permittivity as a function of the temperature. (c): Real permittivity as a function of frequency, and (d): imaginary permittivity as a function of frequency. The change of color indicates variation of frequency and temperature and the lines are guides for the eyes.

The real and imaginary permittivities of all samples decrease with increasing frequency and temperature. For real permittivity, as shown in Figure 3.10(b), BFO-500 exhibits a maximum and minimum of approximately 73 and 42, respectively. BFO-580 shows maximum and minimum values of 243 and 65, respectively, while BFO-600 demonstrates corresponding values of 152 and 56. Similarly, BFO-620 presents maximum and minimum values of 146 and 60. Finally, BFO-640 reaches a maximum value of 234 and a minimum of 73 at around 485 K. Notably, BFO-640 is the only sample that does not exhibit the lowest real permittivity at high frequencies and low temperatures. The permittivity of a dielectric material can be determined by summing all contributing factors, including interfacial charges, dipolar, ionic, and electronic contributions. Accordingly, the decrease in real permittivity as a function of frequency suggests that the contribution of interfacial charges diminishes progressively, leaving the permittivity primarily determined by dipolar, ionic, and electronic effects. The dominant contribution arises from dipolar polarization, as $BiFeO_3$ is a ferroelectric material with a significant number of dipole moments. This often results in high permittivity values, exceeding a thousand, as reported

in previous studies [96, 133]. However, as observed in the permittivity data presented here, none of the samples exhibit such high values. This discrepancy can be attributed to the granular morphology of the samples.

Considering the proposed equivalent electrical circuit model, the permittivity can be expressed as,

$$\varepsilon = \frac{\sigma_{gb}^2 \varepsilon_g + \sigma_G^2 \varepsilon_{gb} + \omega^2 \varepsilon_0^2 \varepsilon_g \varepsilon_{gb} \left(\varepsilon_g + \varepsilon_{gb}\right)}{\left(\sigma_g + \sigma_{gb}\right)^2 + \omega^2 \varepsilon_0^2 \left(\varepsilon_g + \varepsilon_{gb}\right)^2}. \tag{3.2}$$

Calculating Equation 3.2 for high frequencies, it entails,

$$\lim_{\omega \to \infty} \varepsilon = \frac{\varepsilon_0^2 \varepsilon_g \varepsilon_{gb} \left(\varepsilon_g + \varepsilon_{gb}\right)}{\varepsilon_0^2 \left(\varepsilon_g + \varepsilon_{gb}\right)^2} = \frac{\varepsilon_g \varepsilon_{gb}}{\varepsilon_g + \varepsilon_{gb}}. \tag{3.3}$$

But, as $\varepsilon_g \gg \varepsilon_{gb}$, Equation 3.3 gives as a result,

$$\rightarrow \varepsilon_g \gg \varepsilon_{gb} \Rightarrow \lim_{\omega \to \infty} \varepsilon \approx \frac{\varepsilon_g \varepsilon_{gb}}{\varepsilon_g} \approx \varepsilon_{gb}. \tag{3.4}$$

Equation 3.4 indicates that at high frequencies, the permittivity of the grain boundaries predominates. This explains why, in the permittivity spectrum, the observed values are lower than those typically expected for a ferroelectric material. In this case, the grain boundary permittivity effectively masks the contribution from the grains, where the dipolar polarization resides, which would otherwise significantly elevate the permittivity. A similar analysis was conducted in Section 2.3 using Equation 2.14, where it was observed that grain boundary conductivity dominates at low frequencies.

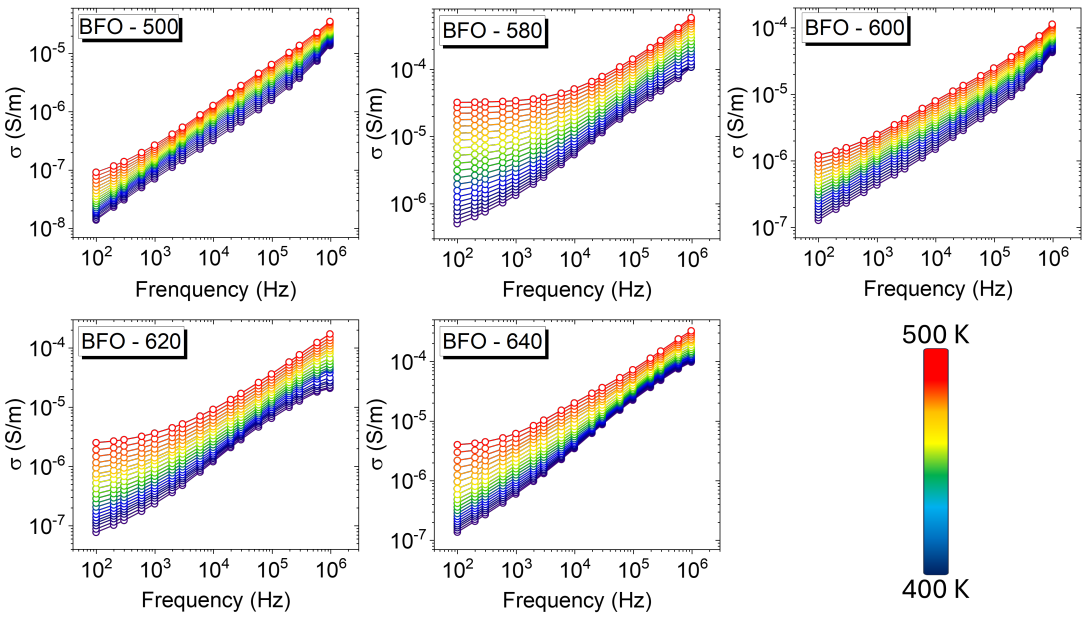

Figure 3.11: Conductivity spectra as a function of the frequency and the temperature. The lines are guides for the eyes.

Given the discussion and review carried out in the paragraph above, Figure 3.11 exhibits the conductivity spectra of the samples. Analyzing the conductivity spectra, it is evident that a well-defined plateau is absent. This observation aligns with the earlier discussion and the relationship to dc conductivity derived from the circuit model.

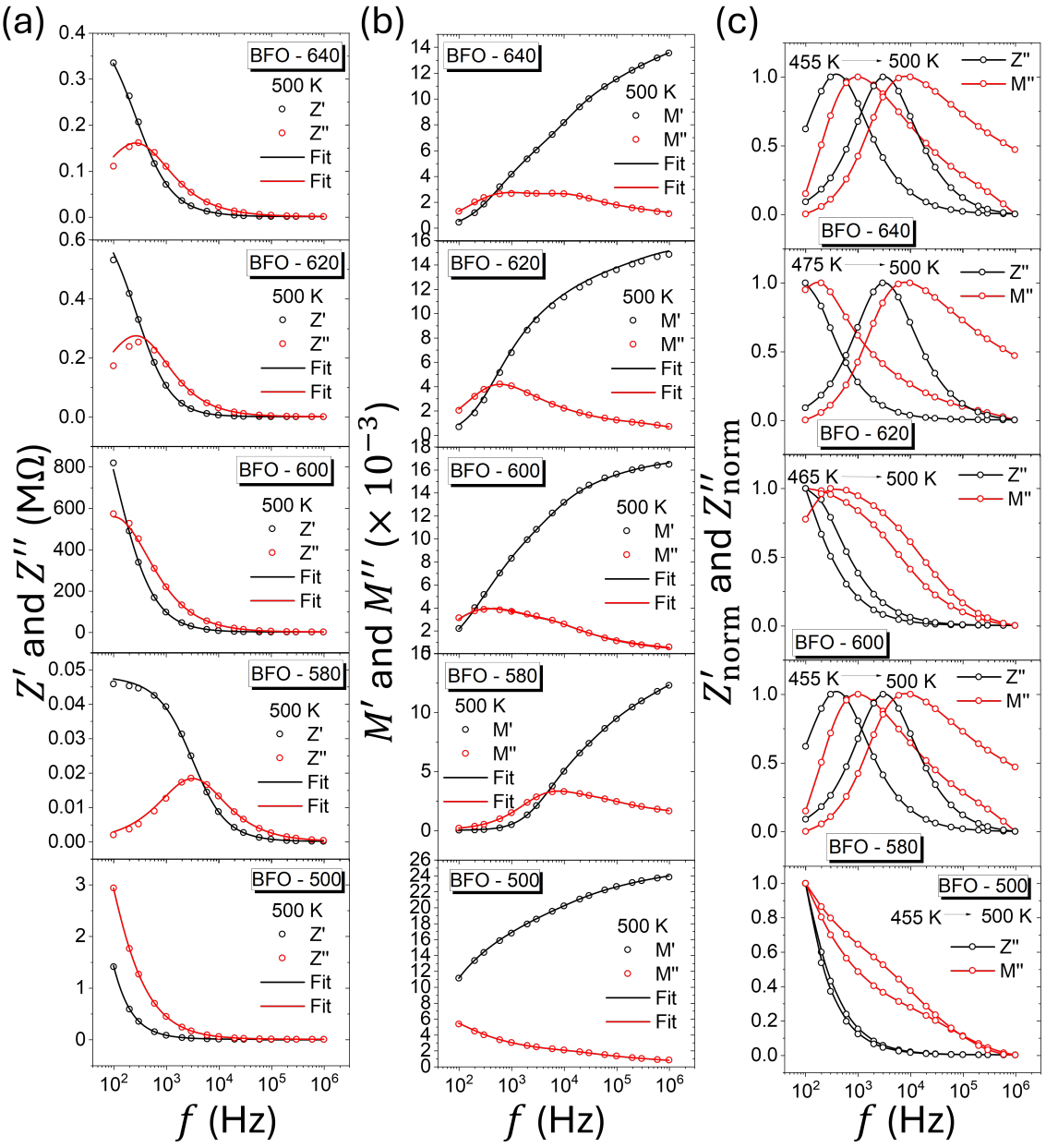

Figure 3.12: (a): Real and imaginary curves of impedance at 500 K, (b): M' and M'' curves at 500 K. The open symbols are correspondent to the experimental data, and the solid lines correspond to the extracted data from fits. (c): Imaginary impedance and modulus normalized curves as functions of frequency and temperature. The lines are guides for the eyes.

Thus, we fitted the real and imaginary parts of the electric impedance, as well as the modulus Z', Z'', M' and M''. The fitted spectra (Figures D.1(a-d)), along with their corresponding fit parameters are provided in Appendix D in Tables D.1, D.2, D.3,

D.4 and D.5. Figure 3.12(a) shows the impedances at 500 K. The most resistive sample, according to the figure, is BFO-600 (ruling out BFO-500[5]), and less resistive is BFO-580. Moreover the processes of relaxation of samples seem to be unique in frequency band from 10^2 to 10^4 Hz.

Upon examining the plots of the real and imaginary curves of the electric modulus at 500 K (Figure 3.12(a)), the noticeable asymmetry suggests the presence of two distinct relaxation processes, associated with the effects of the grain and the grain boundary at low and high frequencies, respectively. Furthermore, the imaginary modulus of BFO-640, shown in Figure 3.12(b), appears to exhibit two local peaks, occurring at 610 Hz and 10^4 Hz, which correspond to the relaxation processes and emphasize the aforementioned effects.

The conclusion drawn in the previous paragraph was based on a symmetry analysis of the impedance curves, along with the observation of some peaks in the electrical modulus curves. It is expected that if two contributions influence the apparent behavior of these curves, corresponding peaks should appear in both the impedance and electrical modulus spectra. However, such peaks were not observed. This discrepancy can be attributed to the differences in the magnitudes of the resistance and capacitance of the material. Specifically, the resistance of the grain boundaries is significantly higher than that of the grains, which leads to an overlap that masks the contribution peak associated with the lower resistance. Conversely, if the capacitance magnitudes of the grains and grain boundaries are similar, the contribution peaks should be observable in the modulus curves. This reasoning is based on the fact that the electric modulus is the reciprocal of the permittivity $\left(M = \frac{1}{\varepsilon^*}\right)$ and that impedance is correlated with resistance[6].

In Figure 3.12(b), we can qualitatively infer, similar to the analysis of the impedance, that BFO-600 exhibits the highest capacitance, while BFO-580 shows the lowest capacitance. This observation is consistent with the relation $\tau = RC$ (where τ is the average relaxation time, R is resistance, and C is capacitance), as the values of R and C commute to determine the relaxation frequency. Additionally, temperature effects on the peaks and relaxation processes can be analyzed, as the average relaxation time is thermally activated. In Figure 3.12(c), the range of conduction can be determined by examining the separation between the normalized curves of imaginary impedance and modulus. Accordingly, Figure 3.12(c) displays the normalized curves of both the imagi-

[5]Throughout the discussion, we exclude the BFO-500 samples due to the coexistence of several secondary phases. This characteristic prevents us from accurately correlating the properties in the graphs to the perovskite behavior, as it is not possible to distinguish the contributions from $BiFeO_3$, **F**, **M**, and **S** with sufficient precision. Although present in small quantities, these observations should also be extended to sample BFO-640, which exhibits prominent **M** growth in its X-ray diffraction patterns.

[6]Equation 2.7, which defines the impedance property, is analogous to Ohm's law and shares the same unit of resistance measurement, Ω. Detailed derivations of these equations and discussions are provided in [14].

nary impedance and modulus, with the temperatures selected based on the displacement of their respective peaks.

The coincidence of normalized curves indicates a possible long-range conductivity, whereas their separation suggests localized conductivity [134, 135]. Based on Figure 3.12(c), none of the samples exhibit coincidence between the normalized curves, indicating that all samples demonstrate short-range conductivity. Notably, the samples with the most pronounced separation between curves are BFO-500 and BFO-600, which are also the most resistive. This observation likely suggests that BFO-600 contains fewer oxygen vacancies and less hopping from Fe^{3+} to Fe^{2+}, resulting in charge carriers being restricted to localized conduction [37, 136, 137].

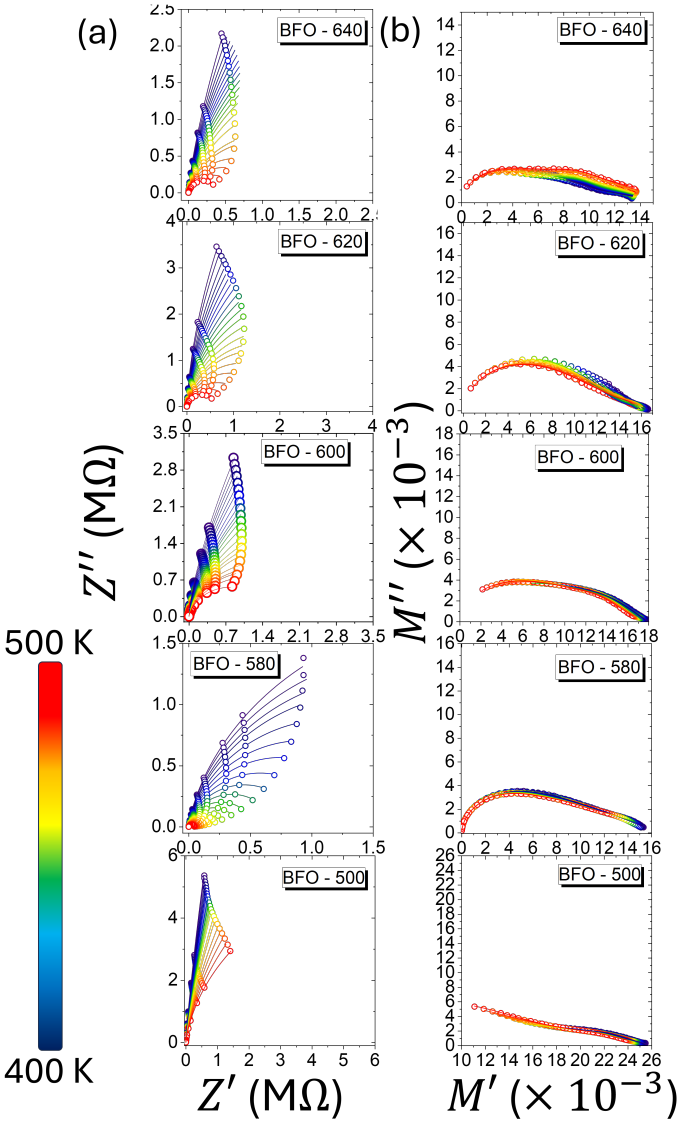

Figure 3.13: (a): Argand-Gauss diagram of electric impedance as function of temperatures, and (b): Argand-Gauss diagram of electric modulus as function of temperature. The points are the experimental data and the solid lines are the fits.

Figures 3.13(a) and (b) illustrate the Argand-Gauss diagrams of the electric impedance and modulus, respectively. When plotted on a linear scale, the Argand-Gauss diagram typically exhibits a semicircular arc. This arc is associated with the resistance (represented by the diameter along the x-axis) and the capacitance (reflected by the radius along the y-axis) [63, 138]. Consequently, the number of arcs in the diagram provides insight into the number of distinct contributions to the system, as characterized by the time constants ($\tau = RC$, where $\tau_g = R_g C_g$ and $\tau_{gb} = R_{gb} C_{gb}$). These contributions, specifically those related to the grain and grain boundary effects, have been already discussed in detail.

In Figure 3.13(a), only a single semicircular arc is observed at a given temperature (T) for all samples, indicating the presence of a single contribution. However, in Figure 3.13(b), two distinct contributions can be clearly identified based on the number of arcs. This observation aligns with the discussions in Section 2.3 and Equation 2.14. Specifically, the grain boundary resistance is significantly higher than that of the grain, while their capacitances remain comparable. This is evident in the Argand-Gauss diagram of the electric modulus, as the modulus is the reciprocal of permittivity, with $C = \varepsilon C_0$.

The comparisons between the values of resistance and capacitance of grains and grain boundaries are presented in Tables D.1, D.2, D.3, D.4, and D.5, located in the appendix D. Figures in Appendix D are plotted on a log-log scale to highlight the accuracy of the fits, while the accompanying insets are displayed in a linear-log scale to facilitate visualization of the relaxation frequency. After performing the fits, the values of R_{gb} and R_g from the aforementioned tables were used to calculate the activation energy as follows.

$$\begin{aligned} \sigma_{g,gb} &= \frac{d}{R_{g,gb} A}, \\ \sigma T &= \sigma_0 e^{-\frac{E_A}{k_B T}}, \\ \ln(\sigma_{g,gb}\, T) &= \ln(\sigma_0) - \frac{E_A}{k_B T}, \end{aligned} \tag{3.5}$$

where $\sigma_{g,gb}$ is the conductivity of grain or grain boundary, T is the absolute temperature, σ_0 is the pre-exponential factor, k_B is Boltzmann constant and E_A is the activation energy that, once linearized, we can estimate through the straight-line slope. Figure 3.14 shows the plots of $\ln(\sigma T)$ versus $1000/T$, their fits, and activation energies estimation of the grain and grain boundary.

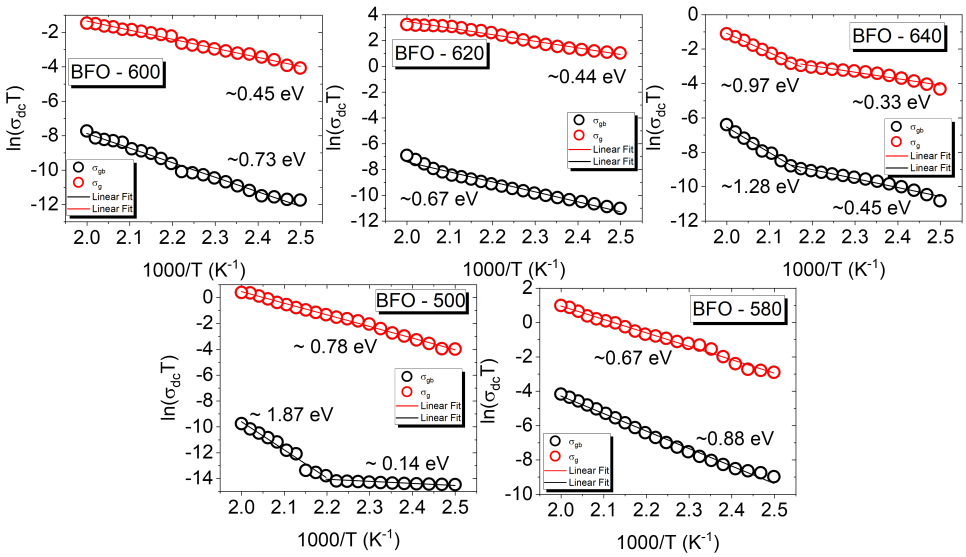

Figure 3.14: Curves of conductivity, fits and estimated activation energy. The black color is correspondent to the grain boundaries, and the color red is correspondent to the grain, and the solid lines are the linear fits.

The values of activation energy are summarized in Table 3.6. It is common to estimate activation energies through impedance spectroscopy measurements, since this is a thermally activated process, and these energies can be associated with some phenomenon that influences the behavior of the curves that we discuss throughout this section. Many authors associate activation energy with an ionization process of oxygen vacancies, as follows. Materials that are crystallized at ambient atmosphere and at high temperatures generate oxygen vacancies, and these vacancies are ionized, leaving conduction electrons, thus forming singly or doubly ionized oxygen vacancies. The energies of these processes are classified so that energies below 0.7 eV are used for singly-ionization work, and energy values between 0.7 and 1.4 are for double-ionization work [14, 48, 134, 135, 139]. However, the discussions about physicochemical principles carried out throughout the section 3.2 allowed us to bring another association of the estimated values of the activation energies.

Materials that are crystallized at ambient atmosphere and high temperatures do indeed generate oxygen vacancies. This process is an attempt to minimize the energy of the system, that is, $\Delta G = \Delta H - T\Delta S$. Defects in solids are formed naturally due to the decrease in free energy (ΔG) and, since the atoms absorb the energy of the crystallization process, the structure becomes more disordered, increasing the entropy of the system (ΔS). Oxygen vacancies are one of the defects associated with our system, and are also the subject of discussion because they are the main charge carriers that influence the electrical behavior in impedance spectroscopy, due to their relaxation time and the frequency range used in the applied electric field. Oxygen vacancies, in $BiFeO_3$, can be located in the interstices of the lattice, in the grain boundaries or on the surface of the solid,

$$\text{null} = V_O^{\cdot\cdot} + O_i'',$$

$$\text{null} = V_O^{\cdot\cdot} + O_{gb}'',$$

$$\text{null} = V_O^{\cdot\cdot} + O_S''.$$

Note, in the above relations, that the vacancy by nature is already electrically charged due to the deficiency of two electrons. The statement used by the authors that the estimated energies are for singly- or doubly-ionization processes for a given temperature variation, results in,

$$V_O^{\cdot\cdot} \xrightarrow{\Delta T} V_O^{\cdot\cdot\cdot} + e', \tag{3.6}$$

$$V_O^{\cdot\cdot} \xrightarrow{\Delta T} V_O^{\cdot\cdot\cdot\cdot} + 2e'. \tag{3.7}$$

Obviously, the deficiency increases to three (singly) or four (doubly) electrons, increasing its effective charge. Although possible, this process may be less likely to occur and "control" the curves obtained in Figure 3.14, being possible and more likely that the energies estimated in these thermally activated processes are associated with the movement of the charge carriers themselves. Figure 3.15 shows, schematically, possible movements of charge carriers when accelerated by the electric force.

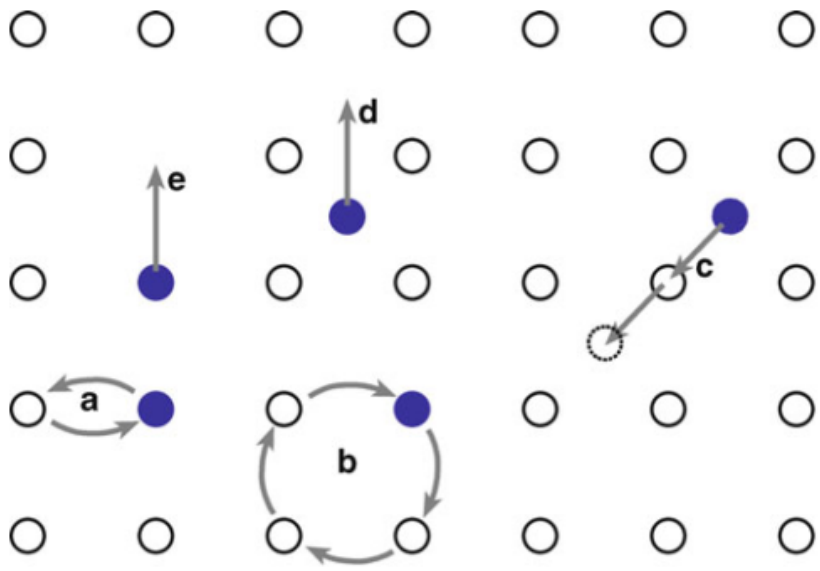

Figure 3.15: Possible movements of charge carriers. (a): by changing equilibrium positions, (b): ring, (c): knock-on, (d): through lattice interstices, and (e): through lattice vacancies. Adapted from [140].

Of the five possible movements, the most likely to occur due to defects are those represented by (d) and (e), movements between vacancies or interstices in the crystal

lattice. The temperature variation of the process (thermal activation) provides more energy to the charge carriers and facilitates conduction through the lattice (mostly ionic conduction), with the energy of each movement corresponding to a specific energy, but which, on average momentum, suggest the values observed in Table 3.6.

Table 3.6: Activation energies of grain and grain boundary of samples. The color red represent the energy for the singly ionization process, and blue to the energies for the doubly ionization process, as categorized by other authors. The value in black (BFO-500 in grain boundaries) is not categorized neither in singly nor in doubly ionization process.

	Activation energy (eV)					
SAMPLES	**BFO-500**	**BFO-580**	**BFO-600**	**BFO-620**	**BFO-640**	
Grain	0.78	0.67	0.45	0.44	0.33	0.97
Grain boundaries	0.14 1.87	0.88	0.73	0.67	0.45	1.28

The samples BFO-500 and BFO-640 exhibited two distinct values of activation energy corresponding to the grain boundaries and the grains. This observation suggests a change in the charge carrier movement mechanism. Among the samples analyzed, both BFO-500 and BFO-640 were found to have the lowest and highest activation energy values. It is important to note that the range of data used for the linear fit was selected based on two criteria: ensuring an adequate number of data points while maintaining a high level of accuracy for the coefficient of determination (R^2). For instance, while the BFO-620 sample appears to exhibit a mechanism change at high temperatures due to data point dispersion, treating this dispersion as a new linear segment would result in segments defined by only three or four data points. This quantity is insufficient to accurately characterize the behavior of a linear trend. Conversely, considering the entire dataset as a single linear segment does not compromise the accuracy of the fit, as evidenced by an R^2 value of approximately 0.973 for the BFO-620 sample.

Figure 3.16(a) shows the dc conductivity of the grain at 400 K and 500 K. Among the samples, BFO-620 exhibited the highest conductivity, while BFO-600 and BFO-640 showed the lowest conductivity values within the grains. Figure 3.16(b) presents the dc conductivity of the grain boundaries at 400 K and 500 K as a function of the crystallization temperature. It is important to reaffirms that the dc conductivity of the grain boundaries represents the overall dc conductivity of the samples. This is because, as the frequency approaches zero, the conductivity function converges to the grain boundaries' conductivity, as discussed in Equation 2.14. The virgin sample (BFO-500) is excluded from this discussion due to the coexistence of secondary phases, which prevents accurate correlation of the conductivity curves to the perovskite phase, as well as BFO-640. Sample BFO-600 demonstrated the lowest dc conductivity at both temperatures, while sample BFO-580 exhibited the highest. Considering that oxygen vacancies are the primary charge

carriers in impedance spectroscopy, this behavior is consistent with predictions from Figure 3.6 and Equation 3.1, on what BFO-600 showed the lowest concentration of ideal oxygen vacancies, whereas BFO-580 had the highest, perfectly aligning with their respective dc conductivity values. Additionally, as discussed in the structural characterization using Raman spectroscopy, the defects are partially influenced by the material's interface and surface, as illustrated in Figure 3.4(b). Reiterating this analysis, BFO-600 exhibited the highest values in both position and band width in the Raman spectra (from deconvolution), which aligns with the expected concentration of defects.

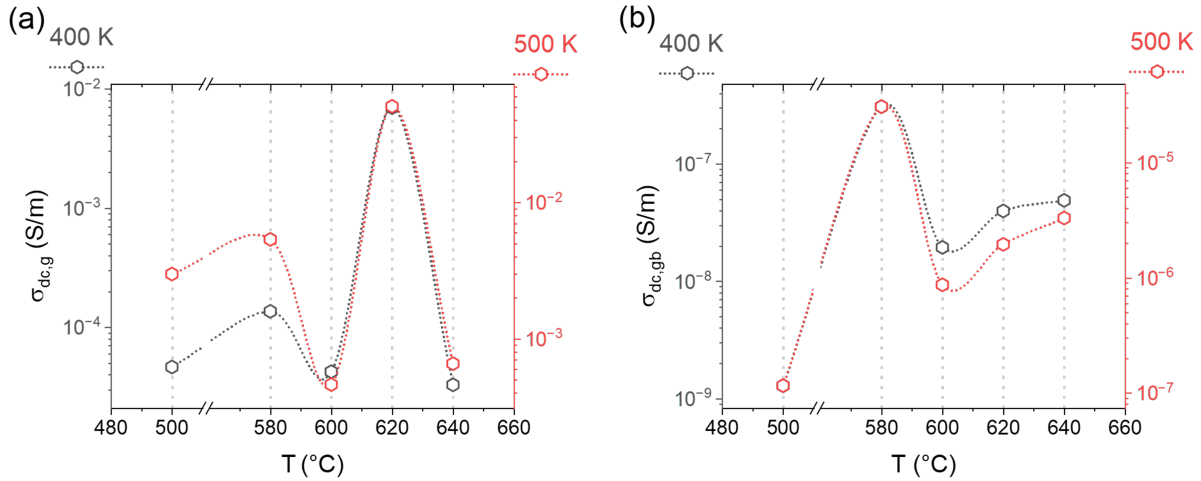

Figure 3.16: IS dc conductivity of samples at 400 K and 500 K. (a): dc conductivity of the grain boundaries ($\sigma_{dc,gb}$), and (b): dc conductivity of the grains ($\sigma_{dc,g}$), both as a function of the crystallization temperature, and the dot-lines are guides for the eyes.

It can be observed that all samples maintained the same behavior and relative relationship with one another at both temperatures. As expected from the electrical behavior of ceramics, the conductivity increased with rising temperature. Furthermore, although sample BFO-500 was excluded from the primary discussion, it is noteworthy that this sample, actually, exhibited the lowest dc conductivity in the grain boundaries (or overall dc conductivity). Additionally, as shown in Figure 3.6(b), BFO-500 also displayed the lowest experimental oxygen vacancy concentration. This observation aligns with its conductivity behavior, even though we are not considering the experimental (oxygen vacancies ratio calculated directly from the O 1s spectra) curve concentrations due to the accuracy.

3.6 Leakage Current Density

For the characterization of the leakage current density, the measurements were conducted in four distinct regions of the samples to analyze the electrical behavior across the entire surface. Each measurement cycle was repeated at least three times, with the

final cycle being recorded for analysis. The measurements were performed under two conditions: in the absence of light (dark) and under green light illumination (λ = 532 nm)[7]. From the data, we tested the models that could be dominant in the electrical behavior, thus, Figure E.1, in Appendix E, shows the hysteresis cycles that it was possible to find a conduction mechanism.

These curves provide a direct evaluation of the leakage current as a function of the electric field, which represents a key limitation for the technological application of $BiFeO_3$. Table 3.7 summarizes the average maximum leakage current values observed in the extreme positive branch of the hysteresis curves under dark conditions, $\langle J_{dark}\rangle$, and green light illumination, $\langle J_{green}\rangle$, for different electrodes. To present an overall behavior, we calculated the average leakage current values corresponding to the number of non-short-circuited hysteresis loops. The values of the leakage current of each electrode are contained in Table E.1.

Table 3.7: Maximum values of the average leakage current ($\langle J\rangle$) given by the positive branch of the J-E hysteresis. $\Delta\langle J\rangle$ represent the relative increase, in percentage, of the average leakage current, when submitted to the green light. Average values of the estimated conductivity in dark ($\langle\sigma_{dark}\rangle$) and under green light ($\langle\sigma_{green}\rangle$), and their relative increase in percentage ($\Delta\langle\sigma\rangle$).

T (°C)	$\langle J_{dark}\rangle$ (10^{-3}A/m^2)	$\langle J_{green}\rangle$ (10^{-3}A/m^2)	$\Delta\langle J\rangle$ (%)	$\langle\sigma_{dark}\rangle$ (10^{-9}S/m)	$\langle\sigma_{green}\rangle$ (10^{-9}S/m)	$\Delta\langle\sigma\rangle$ (%)
640	(3±2)	(17±10)	(491±460)	(0.6±0.3)	(5±3)	(733±570)
620	(25±30)	(41±40)	(64±100)	(10±10)	(17±20)	(70±110)
600	(17±20)	(39±40)	(133±200)	(4±5)	(9±8)	(125±190)
580	(140±80)	(295±160)	(110±90)	(55±40)	(119±70)	(116±100)

To facilitate the analysis of this data, the values from Table 3.7 are presented in Figures 3.17(a), (b), (c), and (d). Samples BFO-600 and BFO-640 exhibited the minimum average leakage current values (see Figure 3.17(a)), indicating a reduced presence of conduction electrons or less electronic mobility, which are the primary variables in this context. In contrast, sample BFO-580 showed the maximum average leakage current value. Although samples BFO-600 and BFO-640 exhibited the lowest leakage current values, we emphasize that sample BFO-640 contained a fraction of a secondary phase. This indicates that the observed properties of this sample, shown in Figure 3.7, are influenced by contributions from the secondary phase, making it impossible to attribute the property exclusively to the perovskite phase, as previously stated. Therefore, when comparing the

[7]It is appropriate to comment that, before measuring definitely one sample, we performed a test measurement where we applied the voltage and kept it increasing until it presents an electric current limit of 10^{-4} A. Above those values, it can be dangerous to the equipment. Anyway, aiming to analyze by comparing samples, their light sensitivity and response to the voltage stimulus, we preferred to fix the electric field on them that resisted the test the least, a range of ±30 kV/cm, as seen in Figure E.1.

results of samples BFO-580, BFO-600, and BFO-620, the largest relative increase was observed in sample BFO-600, in approximately 133%, as shown in Table 3.7(b).

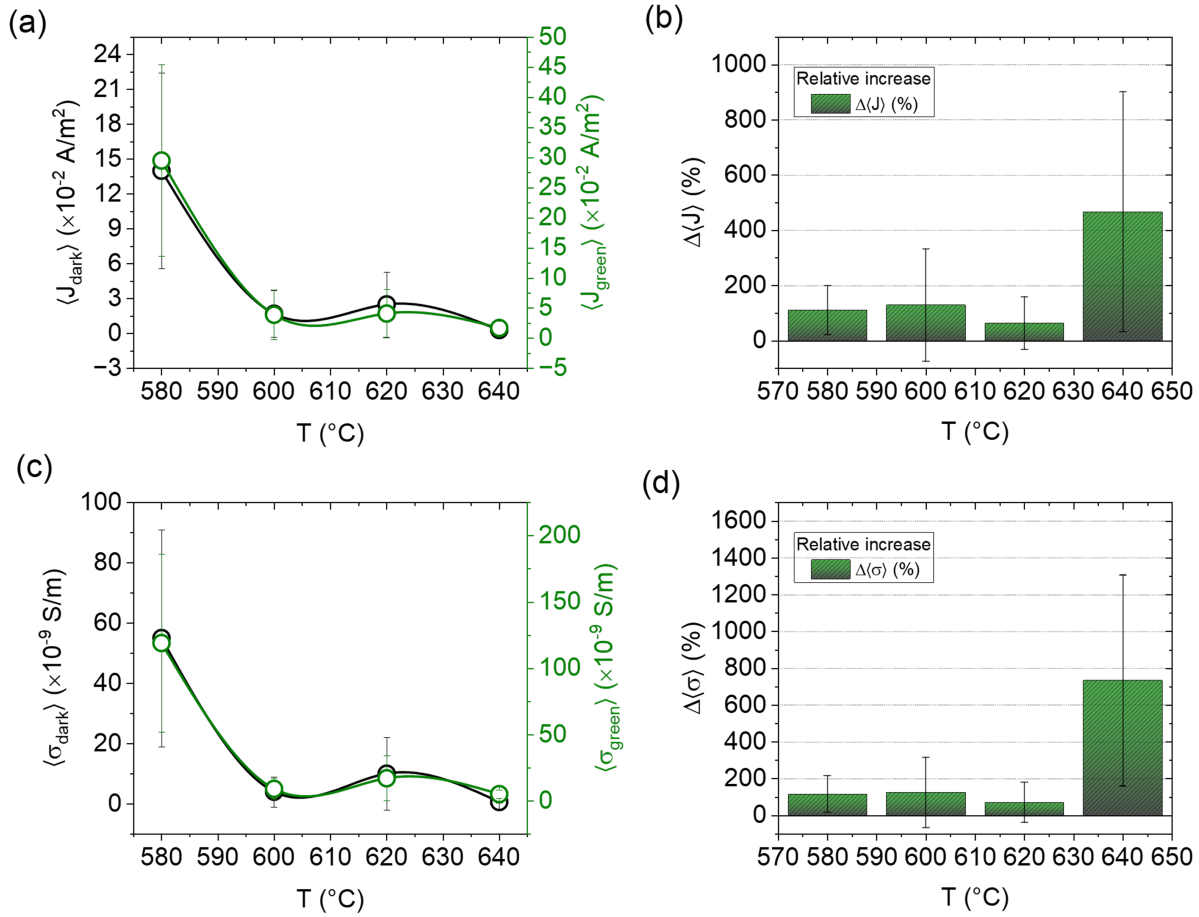

Figure 3.17: Visual representations of values contained in Table 3.7.(a): Average leakage current in dark and under green light conditions as a function of the crystallization temperature. (b): Relative increase of average leakage current between dark and under green light conditions. (c): Average values of the conductivity in dark and under green light conditions as a function of crystallization temperature with their error propagation (given by the linear fit), and (d): the relative increase of average conductivity between dark and under green light conditions. The solid lines in Figures (a) and (c) are guides for the eyes.

To investigate the conduction behavior of the samples and clarify the influences on leakage current, we linearized the curves to determine the slope of each plot. Based on the measurement conditions, we predicted which conduction mechanism was most likely to dominate. Due to the low range of the electric field and the isothermal regime at room temperature, Schottky emission and Poole-Frenkel emission were initially ruled out. Similarly, Fowler-Nordheim tunneling was considered unlikely due to the thickness of the samples, as discussed in Section 2.3. Therefore, Ohmic conduction and the space-charge-limited current (SCLC) mechanisms were tested using the same plot of the y- and x-axes. Figure E.2 presents the log-log plot for all samples. All samples exhibited Ohmic conduction, confirmed by a slope of approximately 1 in the straight-line regions of the

curves. Despite minor fluctuations around the ideal slope, it is reasonable to conclude that the Ohmic conduction mechanism dominates in all samples. To further analyze the data, a linear fit was applied to the curves in the linear plot (corresponding to the same data as in Figure E.2) to estimate conductivity from the slopes and calculate the average conductivity. The fitted curves are presented in Figure E.3 (see Appendix E), and the conductivity values for each electrode are summarized in Table E.1. Similar to the leakage current, the average electric conductivity values and their relative increase as a function of the crystallization temperature are visually represented in Figures 3.17(c) and 3.17(d).

As expected, the conductivity behavior is consistent with the leakage current trends shown in Figures 3.17(a) and (c). Sample BFO-600 exhibited the lowest conductivity values, in approximately 4×10^{-9}S/m under dark conditions and 9×10^{-9}S/m under green light. In contrast, BFO-580 exhibited the highest values of both leakage current and conductivity. Another observation, as seen in Table 3.7 and Figures 3.17(b) and (d), is the relative increase in conductivity between dark and green light conditions.

Under green light illumination, sample BFO-600 stands out by exhibiting an increase in both leakage current and conductivity. The leakage current increased in approximately 133%, while the conductivity increased in approximately 125%. Since the only altered condition was the illumination, we can conclude that electronic mobility remains constant, and the observed changes are due to an increase in charge carrier density. Green light provides sufficient energy to enhance the probability of promoting electrons to the conduction band, a process attributed to excitation through radiation. This leads to an increase in leakage current and conductivity. It is likely that this interaction between light and the material induces a potential difference within the material, generating an electric current and thereby increasing the conduction electrons (or charge carrier density). In other words, these processes are likely related to the photovoltaic effect.

Regarding the relative increase in conductivity, several factors may influence this behavior, including band gap values, decay time of excited particles, recombination centers, and the photovoltaic effect, among others. Assuming the photovoltaic effect as the dominant factor, it can be inferred from the data and discussions presented thus far that BFO-600 exhibits the most optimized electrical properties among the samples, in contrast to BFO-580. Unlike impedance spectroscopy, where oxygen vacancies are the primary charge carriers, the conduction electrons and holes are the main charge carriers influencing the behavior of the curves in this type of measurement. Based on Equation 3.1, it can be concluded that each oxygen vacancy leaves two electrons in the crystal lattice, which bond with the nearest reducing agents, primarily iron, reducing Fe^{3+} to Fe^{2+}. Consequently, it is reasonable to expect that a sample with the lowest concentration of oxygen vacancies also exhibits the lowest concentration of reduced iron, resulting in lower leakage current and conductivity in the J-E curves. Conversely, a higher concentration of oxygen vacancies

would lead to higher iron reduction, leakage current, and conductivity. This conclusion aligns with the observations in Table 3.7. Sample BFO-580, which exhibited the highest concentration of reduced iron, also presented the highest values of leakage current and conductivity, coupled with one of the lowest sensitivities to light. In contrast, sample BFO-600, which showed the lowest concentration of reduced iron, exhibited the lowest values of leakage current and conductivity, along with the highest sensitivity to light.

However much we considered the photovoltaic effect of $BiFeO_3$ the dominant in the increase behavior of leakage current and conductivity, it is necessary a proper photovoltaic measurement to confirm all statement in the paragraph above.

As a final discussion in this section, to clarify and rule out the presence of the Fowler-Nordheim (FN) mechanism in sample BFO-500, as previously discussed in Section 2.3, we plotted the FN plot for this sample, shown in Figure E.4, which is also located in Appendix E. From this figure, representing the data from the selected electrode, it is evident that the behavior does not exhibit a straight-line trend. This observation confirms that the FN mechanism is not dominant in this sample; instead, the electrical behavior is governed by the ohmic mechanism.

3.7 Ultraviolet-Visible Spectroscopy

Although Ultraviolet-Visible Spectroscopy (UV-Vis) is an optical characterization technique for materials, we chose to include this section in this chapter due to the recent discussions regarding the relative increase in electrical properties under green light.

One of the hypotheses proposed in the previous section to explain the relative increase in leakage current and conductivity under green light is that radiation generates a potential difference within the material, leading to an electric current—a phenomenon similar to the photovoltaic effect. However, a necessary condition for the photovoltaic effect to occur is that the energy supplied by the radiation (photon energy) must be greater than the material's band gap. The UV-Vis technique allows us to estimate the band gaps of the films by plotting the data using the Kubelka-Munk function, as discussed in Section 2.4. Figure 3.18 presents the UV-Vis characterizations, plotted through the Kubelka-Munk function.

Table 3.8 summarizes the estimated band gap values derived from the data in Figure 3.18. The band gaps appear to increase almost linearly with the crystallization temperature. However, statistically (considering the dispersion), the band gap values are essentially the same. It was expected that BFO-600 would exhibit a distinct band gap compared to the other samples, consistent with the significant sensitivity to light observed in its behavior. This raises the question: if we can clearly distinguish the relative increase in sensitivity to light under green illumination in the J-E curves, why do we not observe

a similar trend in the band gaps derived from UV-Vis measurements?

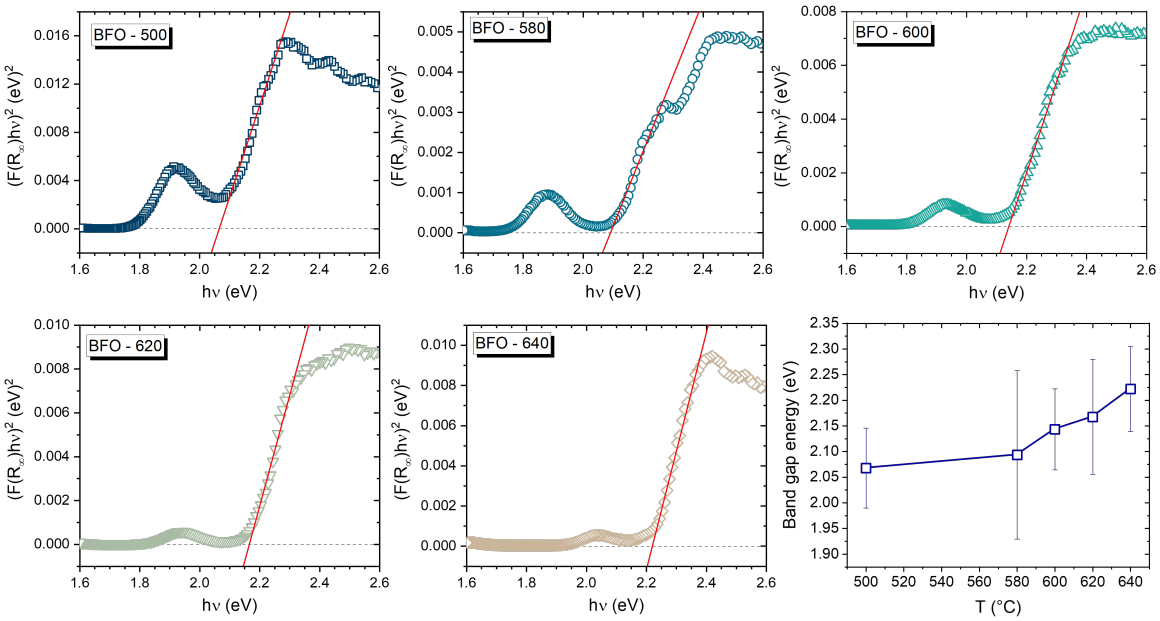

Figure 3.18: UV-Vis spectra plotted based on the Kubelka-Munk function. The open symbols represent the experimental data, and the straight-line is the linear fit to estimate the band gap. In the last figure, the estimated band gap as a function of the crystallization temperature, the deviation was calculated through the fits' accuracy, and the solid line is a guide for the eyes.

The increase in leakage current and conductivity under green light illumination is understandable, as the wavelength used for characterization in the previous section was 532 nm. This corresponds to an energy $E = h\nu = hc/\lambda$ [8], which is approximately 2.33 eV. This energy is very close to the estimated band gap values listed in Table 3.8. However, the band gap is not the only property influencing the photovoltaic effect and its behavior. For charge carriers to contribute to the observed increase in conductivity, they must be excited by the radiation and promoted to the conduction band. The energy required for this promotion is the band gap. Hypothetically, even if all charge carriers absorb the incoming energy and transition to the conduction band, the relaxation time (decay time) of these carriers plays a crucial role. If the relaxation time is too short, these effects might not be fully captured or reflected in the UV-Vis measurements.

To conclude, we must address the intrinsic photovoltaic properties of bismuth ferrite ($BiFeO_3$). Various models propose mechanisms to explain the photovoltaic effect in ferroelectric materials, including surface and interface effects [141], ferroelectric domain contributions [142], spin polarization [143], and bulk effects [144], among others. Additionally, it is well-established that oxygen vacancies, along with other defects, can act as traps, altering the recombination centers of charge carriers and deviating from

[8] E is the photon energy, h is Planck's constant (6.626×10^{-34} m^2kg/s), ν is the wave frequency, and c is the speed of light (299792458 m/s).

Table 3.8: Estimated bandgaps of samples.

Samples	Bandgap (eV)
BFO-640	(2.22 ± 0.08)
BFO-620	(2.17 ± 0.11)
BFO-600	(2.14 ± 0.08)
BFO-580	(2.09 ± 0.16)
BFO-500	(2.07 ± 0.08)

their regular behavior [94]. Assuming that oxygen vacancies are the primary factor responsible for the degradation of the photovoltaic effect[9], BFO-600 has shown the most significant increase in properties under light illumination. This sample also exhibited a lower concentration of oxygen vacancies and iron reduction, as well as fewer interface and surface defects, as indicated by Raman analysis. These observations are consistent with the trends observed in the electrical and optical properties, reinforcing the role of defect minimization in enhancing the photovoltaic performance of $BiFeO_3$ ceramics.

3.8 Piezoresponse Force Microscopy

To investigate the polarization of the samples, we performed the Piezoresponse Force Microscopy (PFM). Figure 3.19 shows the polarized regions of the samples.

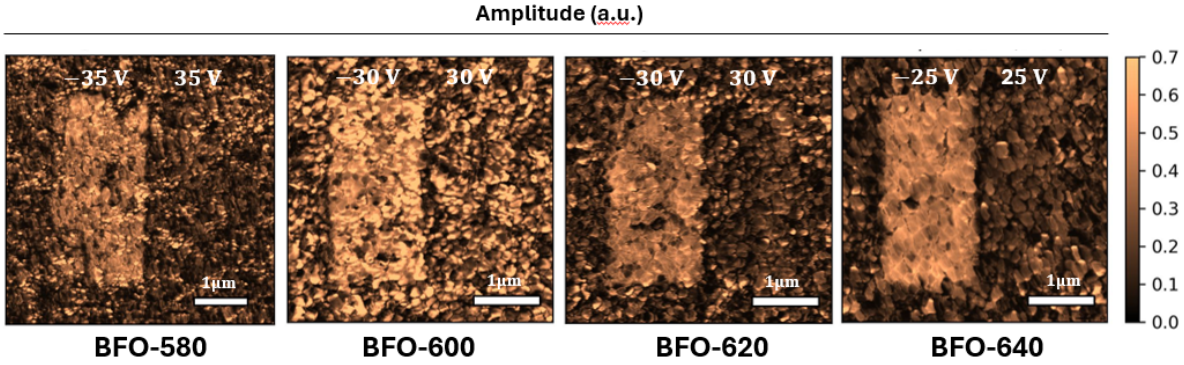

Figure 3.19: Positive and negative poled area of samples. Scale-bar = 1 μm.

We are not including sample BFO-500 in figure because there is not a clear piezoactive region. All samples topography are contained in Appendix F, in Figure F.1. In Figure 3.19, we can clear see and distinguish the polarized region (piezoactive region) in all samples, however, with an asymmetry between the PFM amplitude for the negatively and positively poled areas. BFO-600 has present a less pronounced asymmetry.

[9]In our single-phase samples, there are no significant bismuth vacancies, and iron reduction is generated by oxygen vacancies.

Performing the SS-PFM in local domains, we could record the local ferroelectric hysteresis, in Figure 3.20(a). In figure amplitude vs applied voltage, we observe that the coercive field is decreasing as a function of the crystallization temperature, meanwhile, all samples presented an asymmetry but BFO-600. The coercive fields fluctuate around 40×10^6 V/m (20 V). The values and trending can be analyzed in Figure 3.8(b).

In Figure 3.20(a), the plot of $R\cos(\phi)$ versus the applied voltage shows that the hysteresis loops are tilted. This unusual behavior may indicate that the created domain is unstable, continuing to grow even as the voltage decreases, but shrinking when the voltage polarity is reversed. Among all the samples, BFO-600 exhibited the most stable switched domains. The red lines drawn above the loops indicate the maximum values of the hysteresis. The collected saturation (c) and remnant (d) polarization data, along with their respective trends (line guide for the eyes), are in Figure 3.20(c-d).

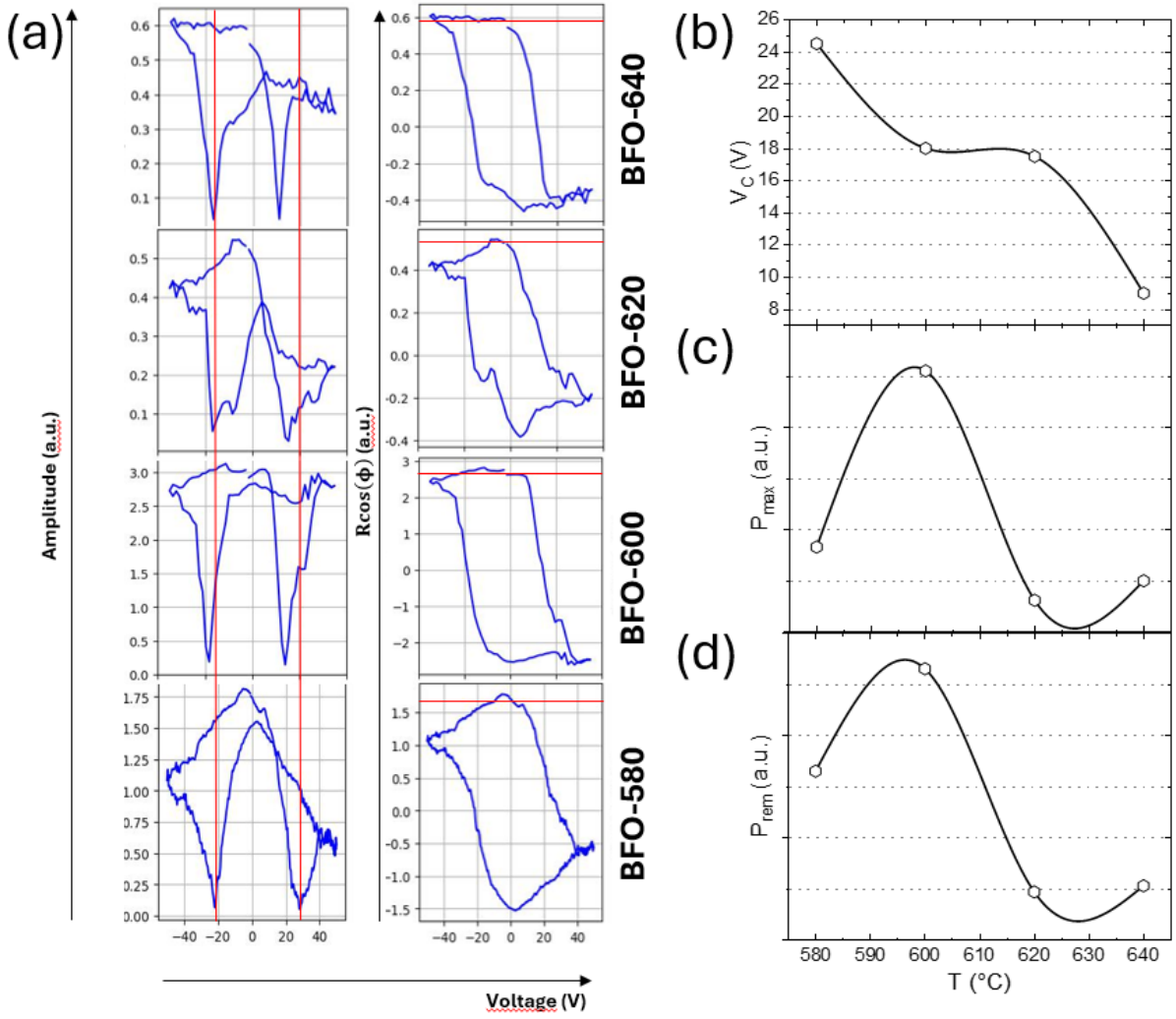

Figure 3.20: (a): Coercive fields and local ferroelectric hysteresis loops of samples, obtained through SS-PFM mode. (b): Values of the coercive voltages (V_C), (c): maximum polarization (saturation, P_{max}), and (d): remnant polarization (P_{rem}) as a function of the crystallization temperature. The solid lines in Figures (b-d) are guides for the eyes.

From the perspective of hysteresis (polarization and coercive fields), several mechanisms influence the relative increase or decrease of these values. However, for a more regular behavior, the coercive field is generally expected to follow the same trend as the saturation and remnant polarization, as illustrated in Figure 2.6, which depicts the "ideal" hysteresis of a single crystal compared to a real polycrystalline one. Interestingly, as shown in Figures 3.20(b-d), the coercive field exhibits a gradual decrease, while both saturation and remnant polarization reach a maximum—contrary to expectations.

To further understand the observations above, we revisit the formation of oxygen vacancy defects, as discussed in Section 3.2. Our analysis of oxygen vacancy concentration curves focused on complex defects. In the system studied here, oxygen vacancies originate from the reduction of iron or from bismuth vacancies, both of which increase with crystallization temperature. This phenomenon is expected, as higher crystallization temperatures provide more thermal energy, facilitating vacancy formation. However, for the $BiFeO_3$ phase to crystallize in an ambient atmosphere, oxygen must enter the structure according to stoichiometry, a process that is enhanced by increasing temperature. In other words, oxygen vacancies formed by non-stoichiometric (free defects) particles can be reduced with increasing temperature. There is a distinction between free and complex vacancies, both of which impact polarization. Free vacancies in ferroelectric materials reduce saturation and remnant polarization by disrupting the cooperative alignment of dipole moments. Additionally, they restrict ferroelectric domain motion, allowing only switching and growth, as free vacancies pin domains, thereby increasing the coercive field. Conversely, complex vacancies affect all three domain mechanisms—switching, nucleation, and growth—leading to a reduction in both polarization and coercive field values. Thus, based on Figures 3.20(b-d), we hypothesize that sample BFO-580 is predominantly influenced by free vacancies, resulting in lower polarization (compared to BFO-600) while maintaining a high coercive field. Sample BFO-600, in contrast, appears to reach an "equilibrium point" between free and complex defects, exhibiting the highest polarization values while maintaining a relatively high coercive field. Beyond this crystallization temperature, the formation of complex defects becomes more dominant, leading to a significant decrease in both polarization and coercive field values.

The above discussion is particularly relevant, as it provides a plausible hypothesis to explain the three curves observed in the defect ratios obtained from the XPS technique (Figure 3.6(b)). Throughout this study, we observed that many characteristic properties of single-phase samples align with the patterns of iron reduction and ideal oxygen vacancy curves. However, the oxygen vacancy curve derived directly from the O 1s spectrum does not appear to correlate well with results from other techniques. As noted earlier and in Section 2.1, defect formation increases with temperature, particularly in the case of complex defects, which is consistent with the OI/OII curve. Regarding the

formation of free defects, higher temperatures promote diffusion, reducing their formation rate. Given the instrument's precision, these free defects were not detected in the O 1s spectrum. However, as reiterated from Equation 3.1, iron—being heavier than oxygen and more easily detectable—undergoes the effects of both types of vacancies, leading to the $Fe^{3+} \Leftrightarrow Fe^{2+}$ reduction process. Between 500 and 580 °C, increasing temperature reduces the formation of free vacancies, though complex defects continue to form. At 600 °C, a peak emerges, suggesting a minimum in defect concentration—interpreted as a "balance point" between free and complex vacancy formation. Beyond this temperature, complex vacancy formation becomes predominant. In summary, from this perspective, the red curve in Figure 3.6 represents complex vacancy formation, the black curve reflects the combined effects of both vacancy types on iron, and the blue curve indicates the oxygen vacancy concentration resulting from the interplay of free and complex vacancies.

Chapter 4

Conclusions

In this study, we conclude that the crystallization temperature in the synthesis of $BiFeO_3$ thin films via the acetate route plays a crucial role in modulating their physical and chemical properties. The selected temperature directly influences the formation, type, and concentration of defects, which in turn impact the material's overall performance. Among these defects, we observed variations in surface and interface defects, point defects (free and complex), and the competition with secondary phases, all of which contribute to the final characteristics of the synthesized thin films. Our results demonstrate that, within the studied temperature range, the optimal crystallization temperature for achieving high-quality $BiFeO_3$ thin films with minimal defects and enhanced functional properties is 600 °C. This conclusion is based on an analysis of the structural, electrical, and optical properties of the synthesized samples. At this specific temperature, the thin film exhibited a substantial reduction in defect density, which was directly correlated with improved material properties compared to samples synthesized at other temperatures. More specifically, the sample prepared at 600 °C showed lower electrical conductivity and leakage currents, which are essential for the stability and reliability of electronic applications. Additionally, the film synthesized at this temperature displayed a pronounced increase in conductivity and electric current under green light illumination, highlighting its potential for optoelectronic applications. Moreover, higher electric polarization values were observed, along with more symmetrical coercive fields, indicating enhanced ferroelectric properties. These improvements suggest that careful control of the crystallization temperature is a key factor in optimizing the functional behavior of $BiFeO_3$ thin films. Therefore, based on the experimental conditions and synthesis process employed in this work, we establish that 600 °C is the most suitable crystallization temperature for producing $BiFeO_3$ thin films with reduced defects and superior physical properties. This study reinforces the importance of temperature modulation in thin-film synthesis and provides valuable insights for future research focused on optimizing the performance of $BiFeO_3$ -based materials in various applications.

Bibliography

[1] D. o. E. United Nations and S. A. S. Development, *Transforming our world: the 2030 agenda for sustainable development*, General Assembly, 2015. [Online]. Available: https://sdgs.un.org/2030agenda.

[2] W. Eerenstein, N. Mathur, and J. F. Scott, "Multiferroic and magnetoelectric materials," *nature*, vol. 442, no. 7104, pp. 759–765, 2006.

[3] J. Ma, J. Hu, Z. Li, and C.-W. Nan, "Recent progress in multiferroic magnetoelectric composites: from bulk to thin films," *Advanced materials*, vol. 23, no. 9, pp. 1062–1087, 2011.

[4] N. A. Spaldin, S.-W. Cheong, and R. Ramesh, "Multiferroics: past, present, and future," *Physics today*, vol. 63, no. 10, pp. 38–43, 2010.

[5] N. A. Spaldin and M. Fiebig, "The renaissance of magnetoelectric multiferroics," *Science*, vol. 309, no. 5733, pp. 391–392, 2005.

[6] F. Jona and G. Shirane, "Ferroelectric crystals," *(No Title)*, 1962.

[7] F. Akasheh, T. Myers, J. D. Fraser, S. Bose, and A. Bandyopadhyay, "Development of piezoelectric micromachined ultrasonic transducers," *Sensors and Actuators A: Physical*, vol. 111, no. 2-3, pp. 275–287, 2004.

[8] K. Kushida and H. Takeuchi, "Piezoelectricity of c-axis oriented pbtio3 thin films," *Applied physics letters*, vol. 50, no. 25, pp. 1800–1801, 1987.

[9] J. F. Scott and C. A. Paz de Araujo, "Ferroelectric memories," *Science*, vol. 246, no. 4936, pp. 1400–1405, 1989.

[10] D. Lee *et al.*, "Multilevel data storage memory using deterministic polarization control," *Advanced Materials*, vol. 24, no. 3, pp. 402–406, 2012.

[11] J.-M. Hu, C.-G. Duan, C.-W. Nan, and L.-Q. Chen, "Understanding and designing magnetoelectric heterostructures guided by computation: progresses, remaining questions, and perspectives," *NPJ Computational Materials*, vol. 3, no. 1, p. 18, 2017.

[12] R. Ramesh and N. A. Spaldin, "Multiferroics: progress and prospects in thin films," *Nature materials*, vol. 6, no. 1, pp. 21–29, 2007.

[13] N. A. Spaldin and R. Ramesh, "Advances in magnetoelectric multiferroics," *Nature materials*, vol. 18, no. 3, pp. 203–212, 2019.

[14] S. P. d. Reis, "Um estudo da influência de defeitos sobre a relaxação dielétrica e outras propriedades físicas relacionadas de filmes finos de bifeo3," 2020.

[15] G. Catalan and J. F. Scott, "Physics and applications of bismuth ferrite," *Advanced materials*, vol. 21, no. 24, pp. 2463–2485, 2009.

[16] S.-H. Baek *et al.*, "The nature of polarization fatigue in bifeo3," *Advanced Materials*, vol. 23, no. 14, pp. 1621–1625, 2011.

[17] M. Bibes and A. Barthélémy, "Towards a magnetoelectric memory," *Nature materials*, vol. 7, no. 6, pp. 425–426, 2008.

[18] N. A. Hill, *Why are there so few magnetic ferroelectrics?* 2000.

[19] T Choi, S Lee, Y. Choi, V Kiryukhin, and S.-W. Cheong, "Switchable ferroelectric diode and photovoltaic effect in bifeo3," *Science*, vol. 324, no. 5923, pp. 63–66, 2009.

[20] T. Gao *et al.*, "A review: preparation of bismuth ferrite nanoparticles and its applications in visible-light induced photocatalyses," *Rev. adv. mater. sci*, vol. 40, no. 2, pp. 97–109, 2015.

[21] B Kundys, M. Viret, D. Colson, and D. O. Kundys, "Light-induced size changes in bifeo3 crystals," *Nature materials*, vol. 9, no. 10, pp. 803–805, 2010.

[22] D Sando *et al.*, "Large elasto-optic effect and reversible electrochromism in multiferroic bifeo3," *Nature communications*, vol. 7, no. 1, p. 10 718, 2016.

[23] M. Alexe and D. Hesse, "Tip-enhanced photovoltaic effects in bismuth ferrite," *Nature communications*, vol. 2, no. 1, p. 256, 2011.

[24] C.-H. Yang, D. Kan, I. Takeuchi, V. Nagarajan, and J. Seidel, "Doping bifeo 3: approaches and enhanced functionality," *Physical Chemistry Chemical Physics*, vol. 14, no. 46, pp. 15 953–15 962, 2012.

[25] J.-G. Park, M. D. Le, J. Jeong, and S. Lee, "Structure and spin dynamics of multiferroic bifeo3," *Journal of Physics: Condensed Matter*, vol. 26, no. 43, p. 433 202, 2014.

[26] I. Sosnowska, T. P. Neumaier, and E. Steichele, "Spiral magnetic ordering in bismuth ferrite," *Journal of Physics C: Solid State Physics*, vol. 15, no. 23, p. 4835, 1982.

[27] F Tyholdt, S Jørgensen, H Fjellvåg, and A. Gunnaes, "Synthesis of oriented bifeo3 thin films by chemical solution deposition: phase, texture, and microstructural development," *Journal of materials research*, vol. 20, no. 8, pp. 2127–2139, 2005.

[28] X. Qi, J. Dho, R. Tomov, M. G. Blamire, and J. L. MacManus-Driscoll, "Greatly reduced leakage current and conduction mechanism in aliovalent-ion-doped bifeo3," *Applied Physics Letters*, vol. 86, no. 6, 2005.

[29] Y. Wang, L Zhou, M. Zhang, X. Chen, J.-M. Liu, and Z. Liu, "Room-temperature saturated ferroelectric polarization in bifeo3 ceramics synthesized by rapid liquid phase sintering," *Applied Physics Letters*, vol. 84, no. 10, pp. 1731–1733, 2004.

[30] R. Palai *et al.*, "β phase and γ-β metal-insulator transition in multiferroic bi fe o 3," *Physical Review B—Condensed Matter and Materials Physics*, vol. 77, no. 1, p. 014 110, 2008.

[31] R Safi and H Shokrollahi, "Physics, chemistry and synthesis methods of nanostructured bismuth ferrite (bifeo3) as a ferroelectro-magnetic material," *Progress in Solid State Chemistry*, vol. 40, no. 1-2, pp. 6–15, 2012.

[32] J. Wu, J. Wang, D. Xiao, and J. Zhu, "Migration kinetics of oxygen vacancies in mn-modified bifeo3 thin films," *ACS Applied Materials & Interfaces*, vol. 3, no. 7, pp. 2504–2511, 2011.

[33] C. Wang *et al.*, "Leakage current of multiferroic (bi0. 6tb0. 3la0. 1) feo3 thin films grown at various oxygen pressures by pulsed laser deposition and annealing effect," *Journal of Applied Physics*, vol. 99, no. 5, 2006.

[34] Q. Xu, M. Sobhan, Q. Yang, F. Anariba, K. P. Ong, and P. Wu, "The role of bi vacancies in the electrical conduction of bifeo 3: a first-principles approach," *Dalton Transactions*, vol. 43, no. 28, pp. 10 787–10 793, 2014.

[35] J. Dho, X. Qi, H. Kim, J. L. MacManus-Driscoll, and M. G. Blamire, "Large electric polarization and exchange bias in multiferroic bifeo3," *ADVANCED MATERIALS-DEERFIELD BEACH THEN WEINHEIM-*, vol. 18, no. 11, p. 1445, 2006.

[36] K. Wang, J.-M. Liu, and Z. Ren, "Multiferroicity: the coupling between magnetic and polarization orders," *Advances in Physics*, vol. 58, no. 4, pp. 321–448, 2009.

[37] J. Wu and J. Wang, "Orientation dependence of ferroelectric behavior of bifeo3 thin films," *Journal of Applied Physics*, vol. 106, no. 10, 2009.

[38] Q. Zhang, D. Sando, and V. Nagarajan, "Chemical route derived bismuth ferrite thin films and nanomaterials," *Journal of Materials Chemistry C*, vol. 4, no. 19, pp. 4092–4124, 2016.

[39] N. Parvathy and R Govindaraj, "Atomic scale insights on the growth of bifeo3 nanoparticles," *Scientific Reports*, vol. 12, no. 1, p. 4758, 2022.

[40] T. M. Gesing *et al.*, "Nano-crystalline precursor formation, stability, and transformation to mullite-type visible-light photocatalysts," *Journal of Materials Science*, vol. 57, no. 41, pp. 19 280–19 299, 2022.

[41] P. Sharma, P. Diwan, and O. Pandey, "Impact of environment on the kinetics involved in the solid-state synthesis of bismuth ferrite," *Materials Chemistry and Physics*, vol. 233, pp. 171–179, 2019.

[42] A. Kirsch, M. M. Murshed, M. Schowalter, A. Rosenauer, and T. M. Gesing, "Nanoparticle precursor into polycrystalline bi2fe4o9: an evolutionary investigation of structural, morphological, optical, and vibrational properties," *The Journal of Physical Chemistry C*, vol. 120, no. 33, pp. 18 831–18 840, 2016.

[43] X.-Z. Chen, Z.-C. Qiu, J.-P. Zhou, G. Zhu, X.-B. Bian, and P. Liu, "Large-scale growth and shape evolution of bismuth ferrite particles with a hydrothermal method," *Materials Chemistry and Physics*, vol. 126, no. 3, pp. 560–567, 2011.

[44] H. Dai, Z. Chen, T Li, R. Xue, and J Chen, "Structural and electrical properties of bismuth ferrite ceramics sintered in different atmospheres," *Journal of superconductivity and novel magnetism*, vol. 26, pp. 3125–3132, 2013.

[45] A Manzoor, A. Afzal, M Umair, A. Ali, M Rizwan, and M. Yaqoob, "Synthesis and characterization of bismuth ferrite (bifeo3) nanoparticles by solution evaporation method," *Journal of Magnetism and Magnetic Materials*, vol. 393, pp. 269–272, 2015.

[46] Y.-j. Zhang *et al.*, "Structural and magnetic properties in bi1- xrxfeo3 (x= 0–1, r= la, nd, sm, eu and tb) polycrystalline ceramics," *Journal of Magnetism and Magnetic Materials*, vol. 322, no. 15, pp. 2251–2255, 2010.

[47] H. Uchida, R. Ueno, H. Funakubo, and S. Koda, "Crystal structure and ferroelectric properties of rare-earth substituted bifeo3 thin films," *Journal of applied physics*, vol. 100, no. 1, 2006.

[48] J. Wu and J. Wang, "Ferroelectric and impedance behavior of la-and ti-codoped bifeo3 thin films," *Journal of the American Ceramic Society*, vol. 93, no. 9, pp. 2795–2803, 2010.

[49] T. Zheng and J. Wu, "Enhanced piezoelectric activity in high-temperature bi 1-x- y sm x la y feo 3 lead-free ceramics," *Journal of Materials Chemistry C*, vol. 3, no. 15, pp. 3684–3693, 2015.

[50] F Mizouri, N Abdelmoula, D Mezzane, and H Khemakhem, "Impedance spectroscopy and conduction mechanism of multiferroic bi0. 8 (ba0. 9ca0. 1) 0.8 fe0. 8 (ti0. 9sn0. 1) 0.8 o3," *Journal of Alloys and Compounds*, vol. 763, pp. 570–580, 2018.

[51] G. Hu, X Cheng, W. Wu, and C. Yang, "Effects of gd substitution on structure and ferroelectric properties of bifeo3 thin films prepared using metal organic decomposition," *Applied Physics Letters*, vol. 91, no. 23, 2007.

[52] A. J. Preethi and M Ragam, "Effect of doping in multiferroic bfo: a review," *Journal of Advanced Dielectrics*, vol. 11, no. 06, p. 2 130 001, 2021.

[53] K. Papadopoulos *et al.*, "Control of physical properties in bifeo3 nanoparticles via sm3+ and co2+ ion doping," *Nanotechnology*, vol. 35, no. 1, p. 015 707, 2023.

[54] A. J. Freitas Cabral, A. Valerio, S. L. Morelhao, N. R. Checca, M. M. Soares, and C. M. Remedios, "Controlled formation and growth kinetics of phase-pure, crystalline bifeo3 nanoparticles," *Crystal Growth & Design*, vol. 20, no. 2, pp. 600–607, 2019.

[55] T. Rojac *et al.*, "Bifeo 3 ceramics: processing, electrical, and electromechanical properties," *Journal of the American Ceramic Society*, vol. 97, no. 7, pp. 1993–2011, 2014.

[56] F. V. de Andrade Borges, "Efeito da substituição de bismuto por samário sobre propriedades físicas de filmes finos de ferrita de bismuto," 2023.

[57] F. E. Freitas, "Propriedades físicas de filmes finos de bifeo3 com variações composicionais em torno da estequiometria," 2022.

[58] F. Minussi, F. Borges, and E. Araújo, "Charge transport and dielectric characteristics of sm x bi1- x feo3 thin films from the perspective of grain and grain boundary properties," *Journal of Physics D: Applied Physics*, vol. 56, no. 35, p. 355 302, 2023.

[59] Y González-Abreu, S. Reis, F. Freitas, J. Eiras, and E. Araujo, "Effects of crystallization kinetics on the dielectric and electrical properties of bifeo 3 films," *Journal of Advanced Dielectrics*, vol. 11, no. 03, p. 2 140 007, 2021.

[60] S. Reis and E. Araujo, "Impact of defects on the electrical properties of bifeo3 thin films," *Ferroelectrics*, vol. 556, no. 1, pp. 70–78, 2020.

[61] S. Reis, F. Freitas, and E. Araújo, "Processing of bifeo3 thin films to control their dielectric response," *Ferroelectrics*, vol. 560, no. 1, pp. 61–69, 2020.

[62] S. P. dos Reis, F. B. Minussi, and E. B. Araújo, "Thermally activated processes and bias field effects on the electrical properties of bifeo3 thin films," *SCIENCE & ENGINEERING*, vol. 2, no. 1, pp. 25–34, 2020.

[63] S. Reis and E. Araujo, "Dielectric relaxation and electrical conductivity of random oriented bifeo3 thin films," *Ferroelectrics*, vol. 545, no. 1, pp. 111–118, 2019.

[64] R. Assink and R. Schwartz, "Proton and carbon-13 nmr investigations of lead zirconate titanate (pb (zr, ti) o3) thin-film precursor solutions," *Chemistry of materials*, vol. 5, no. 4, pp. 511–517, 1993.

[65] H. Rietveld, "Line profiles of neutron powder-diffraction peaks for structure refinement," *Acta Crystallographica*, vol. 22, no. 1, pp. 151–152, 1967.

[66] H. M. Rietveld, "A profile refinement method for nuclear and magnetic structures," *Applied Crystallography*, vol. 2, no. 2, pp. 65–71, 1969.

[67] A. C. Larson and R. B. Von Dreele, "Gsas," *General Structure Analysis System. LANSCE, MS-H805, Los Alamos, New Mexico*, 1994.

[68] B. T. EXPGUI, "A graphical user interface for gsas., 2001, 34," *DOI: https://doi.org/10.1107 S*, pp. 210–213,

[69] P Thompson, D. Cox, and J. Hastings, "Rietveld refinement of debye–scherrer synchrotron x-ray data from al2o3," *Journal of Applied Crystallography*, vol. 20, no. 2, pp. 79–83, 1987.

[70] L. McCusker, R. Von Dreele, D. Cox, D Louër, and P Scardi, "Rietveld refinement guidelines," *Journal of Applied Crystallography*, vol. 32, no. 1, pp. 36–50, 1999.

[71] G. Williamson and W. Hall, "X-ray line broadening from filed aluminium and wolfram," *Acta metallurgica*, vol. 1, no. 1, pp. 22–31, 1953.

[72] A. D. G. Rodrigues and J. C. Galzerani, "Espectroscopias de infravermelho, raman e de fotoluminescência: potencialidades e complementaridades," *Revista Brasileira de ensino de Física*, vol. 34, p. 4309, 2013.

[73] C. J. Letti, "Estudo de nanocompósitos formados por partículas de óxidos de ferro e polímeros por meio da espectroscopia raman," 2013.

[74] C. N. Lima, "Produção e caracterização estrutural, térmica e óptica da liga semicondutora nisb2," 2014.

[75] F. N. Lopes, "Espectroscopia raman aplicada ao estudo de pigmentos em bens culturais: i-pinturas rupestres," Ph.D. dissertation, Universidade de São Paulo, 2005.

[76] H Fukumura, H Harima, K Kisoda, M Tamada, Y Noguchi, and M Miyayama, "Raman scattering study of multiferroic bifeo3 single crystal," *Journal of Magnetism and Magnetic Materials*, vol. 310, no. 2, e367–e369, 2007.

[77] H Fukumura *et al.*, "Observation of phonons in multiferroic bifeo3 single crystals by raman scattering," *Journal of Physics: Condensed Matter*, vol. 19, no. 36, p. 365 224, 2007.

[78] P. Hermet, M. Goffinet, J Kreisel, and P. Ghosez, "Raman and infrared spectra of multiferroic bismuth ferrite from first principles," *Physical Review B—Condensed Matter and Materials Physics*, vol. 75, no. 22, p. 220 102, 2007.

[79] Y Yang, J. Sun, K Zhu, Y. Liu, and L Wan, "Structure properties of bifeo3 films studied by micro-raman scattering," *Journal of Applied Physics*, vol. 103, no. 9, 2008.

[80] D. Rout, K.-S. Moon, and S.-J. L. Kang, "Temperature-dependent raman scattering studies of polycrystalline bifeo3 bulk ceramics," *Journal of Raman Spectroscopy: An International Journal for Original Work in all Aspects of Raman Spectroscopy, Including Higher Order Processes, and also Brillouin and Rayleigh Scattering*, vol. 40, no. 6, pp. 618–626, 2009.

[81] A. Talkenberger *et al.*, "Raman spectroscopic investigations of epitaxial bifeo3 thin films on rare earth scandate substrates," *Journal of Raman Spectroscopy*, vol. 46, no. 12, pp. 1245–1254, 2015.

[82] L. G. d. OLIVEIRA, "Síntese, caracterização estrutural e morfológica da cerâmica ferroelétrica livre de chumbo knanbo3-niobato de sódio e potássio, modificada com molibdênio [k0, 5na0, 5][nb (1-x) mo (x)] o3," 2019.

[83] T. J. Collins, "Imagej for microscopy," *Biotechniques*, vol. 43, no. S1, S25–S30, 2007.

[84] J. Bauerle, "Study of solid electrolyte polarization by a complex admittance method," *Journal of Physics and Chemistry of Solids*, vol. 30, no. 12, pp. 2657–2670, 1969.

[85] M. Verkerk, B. Middelhuis, and A. Burggraaf, "Effect of grain boundaries on the conductivity of high-purity zro2 y2o3 ceramics," *Solid State Ionics*, vol. 6, no. 2, pp. 159–170, 1982.

[86] N. J. Kidner, N. H. Perry, T. O. Mason, and E. J. Garboczi, "The brick layer model revisited: introducing the nano-grain composite model," *Journal of the American Ceramic Society*, vol. 91, no. 6, pp. 1733–1746, 2008.

[87] J. R. Macdonald and M. K. Brachman, "Linear-system integral transform relations," *Reviews of modern physics*, vol. 28, no. 4, p. 393, 1956.

[88] J. R. Macdonald *et al.*, *Impedance spectroscopy: theory, experiment, and applications*. John Wiley & Sons, 2018.

[89] F.-C. Chiu, "A review on conduction mechanisms in dielectric films," *Advances in Materials Science and Engineering*, vol. 2014, no. 1, p. 578 168, 2014.

[90] I. S. Golovina, M. Falmbigl, A. V. Plokhikh, T. C. Parker, C. Johnson, and J. E. Spanier, "Effect of annealing conditions on the electrical properties of ald-grown polycrystalline bifeo 3 films," *Journal of Materials Chemistry C*, vol. 6, no. 20, pp. 5462–5472, 2018.

[91] J. Wang *et al.*, "Microscopic physical origin of polarization induced large tunneling electroresistance in tetragonal-phase bifeo3," *Acta Materialia*, vol. 225, p. 117 564, 2022.

[92] Q. Fan, C. Ma, C. Ma, R. Lu, S. Cheng, and M. Liu, "Manipulating leakage behavior via thickness in epitaxial bazr0. 35ti0. 65o3 thin film capacitors," *Applied Physics Letters*, vol. 116, no. 19, 2020.

[93] H. Schroeder and S. Schmitz, "Thickness dependence of leakage currents in high-permittivity thin films," *Applied physics letters*, vol. 83, no. 21, pp. 4381–4383, 2003.

[94] T. Yang, J. Wei, Y. Guo, Z. Lv, Z. Xu, and Z. Cheng, "Manipulation of oxygen vacancy for high photovoltaic output in bismuth ferrite films," *ACS applied materials & interfaces*, vol. 11, no. 26, pp. 23 372–23 381, 2019.

[95] R. T. R. Thomas and D. D. D. Dube, "Structural, electrical and optical properties of sol–gel processed lead titanate thin films," *Japanese journal of applied physics*, vol. 36, no. 12R, p. 7337, 1997.

[96] A. K. Bain and P. Chand, *Ferroelectrics: Principles and applications*. John Wiley & Sons, 2017.

[97] E. Soergel, "Piezoresponse force microscopy (pfm)," *Journal of Physics D: Applied Physics*, vol. 44, no. 46, p. 464 003, 2011.

[98] D. Damjanovic, "Ferroelectric, dielectric and piezoelectric properties of ferroelectric thin films and ceramics," *Reports on progress in physics*, vol. 61, no. 9, p. 1267, 1998.

[99] S Magonov, "Piezoresponse force microscopy in its applications," *Development NM, editor*, 2019.

[100] R Jona and G Shirane, *Ferroelectric crystals.(1993)*.

[101] S. Jesse, A. P. Baddorf, and S. V. Kalinin, "Switching spectroscopy piezoresponse force microscopy of ferroelectric materials," *Applied physics letters*, vol. 88, no. 6, 2006.

[102] C Terrier, J. Chatelon, and J. Roger, "Electrical and optical properties of sb: sno2 thin films obtained by the sol-gel method," *Thin solid films*, vol. 295, no. 1-2, pp. 95–100, 1997.

[103] J. I. Pankove, *Optical processes in semiconductors*. Courier Corporation, 1975.

[104] D. L. Pavia, G. M. Lampman, G. S. Kriz, J. R. Vyvyan, *et al.*, "Introduction to spectroscopy," 2015.

[105] P. Makuła, M. Pacia, and W. Macyk, *How to correctly determine the band gap energy of modified semiconductor photocatalysts based on uv–vis spectra*, 2018.

[106] S. Landi Jr, I. R. Segundo, E. Freitas, M. Vasilevskiy, J. Carneiro, and C. J. Tavares, "Use and misuse of the kubelka-munk function to obtain the band gap energy from diffuse reflectance measurements," *Solid state communications*, vol. 341, p. 114 573, 2022.

[107] D. Sando, A Barthélémy, and M Bibes, "Bifeo3 epitaxial thin films and devices: past, present and future," *Journal of Physics: Condensed Matter*, vol. 26, no. 47, p. 473 201, 2014.

[108] M. Chen, Z. Shen, S. Tang, W. Shi, D. Cui, and Z. Chen, "Stress effect on raman spectra of ce-doped batio3 films," *Journal of Physics: Condensed Matter*, vol. 12, no. 31, p. 7013, 2000.

[109] D. Tenne *et al.*, "Effect of thermal strain on the ferroelectric phase transition in polycrystalline ba0. 5sr0. 5tio3 thin films studied by raman spectroscopy," *Applied physics letters*, vol. 85, no. 18, pp. 4124–4126, 2004.

[110] Y. I. Yuzyuk, R. Katiyar, V. Alyoshin, I. Zakharchenko, D. Markov, and E. Sviridov, "Stress relaxation in heteroepitaxial (b a, s r) tio 3/(001) mgo thin film studied by micro-raman spectroscopy," *Physical Review B*, vol. 68, no. 10, p. 104 104, 2003.

[111] H. Guo, Z. Chen, B. Cheng, H. Lu, L. Liu, and Y. Zhou, "Structure dynamics of strongly reduced epitaxial batio3- x studied by raman scattering," *Journal of the European Ceramic society*, vol. 25, no. 12, pp. 2347–2352, 2005.

[112] M. R. Islam, M. S. Islam, M. Zubair, H. M. Usama, M. S. Azam, and A. Sharif, "Evidence of superparamagnetism and improved electrical properties in ba and ta co-doped bifeo3 ceramics," *Journal of Alloys and Compounds*, vol. 735, pp. 2584–2596, 2018.

[113] D. Chen, F. Niu, L. Qin, S. Wang, N. Zhang, and Y. Huang, "Defective bifeo3 with surface oxygen vacancies: facile synthesis and mechanism insight into photocatalytic performance," *Solar Energy Materials and Solar Cells*, vol. 171, pp. 24–32, 2017.

[114] V. Sharma, R. K. Ghosh, and B. K. Kuanr, "Investigation of room temperature ferromagnetism in transition metal doped bifeo3," *Journal of Physics: Condensed Matter*, vol. 31, no. 39, p. 395 802, 2019.

[115] S Bharathkumar, M Sakar, S Balakumar, *et al.*, "Versatility of electrospinning in the fabrication of fibrous mat and mesh nanostructures of bismuth ferrite (bifeo 3) and their magnetic and photocatalytic activities," *Physical Chemistry Chemical Physics*, vol. 17, no. 27, pp. 17 745–17 754, 2015.

[116] Y. Zhang *et al.*, "Enhanced magnetic properties of bifeo3 thin films by doping: analysis of structure and morphology," *Nanomaterials*, vol. 8, no. 9, p. 711, 2018.

[117] R. Das, T. Sarkar, and K Mandal, "Multiferroic properties of ba2+ and gd3+ co-doped bismuth ferrite: magnetic, ferroelectric and impedance spectroscopic analysis," *Journal of Physics D: Applied Physics*, vol. 45, no. 45, p. 455 002, 2012.

[118] T. Norby, "A kr öger-vink compatible notation for defects in inherently defective sublattices," *Journal of the Korean Ceramic Society*, vol. 47, no. 1, pp. 19–25, 2010.

[119] T. Soltani and B.-K. Lee, "Enhanced formation of sulfate radicals by metal-doped bifeo3 under visible light for improving photo-fenton catalytic degradation of 2-chlorophenol," *Chemical Engineering Journal*, vol. 313, pp. 1258–1268, 2017.

[120] T. Yamashita and P. Hayes, "Analysis of xps spectra of fe2+ and fe3+ ions in oxide materials," *Applied surface science*, vol. 254, no. 8, pp. 2441–2449, 2008.

[121] M. Kamali, M. E. V. Costa, G. Otero-Irurueta, and I. Capela, "Ultrasonic irradiation as a green production route for coupling crystallinity and high specific surface area in iron nanomaterials," *Journal of cleaner production*, vol. 211, pp. 185–197, 2019.

[122] A. R. Goldman, J. L. Fredricks, and L. A. Estroff, "Exploring reaction pathways in the hydrothermal growth of phase-pure bismuth ferrites," *Journal of Crystal Growth*, vol. 468, pp. 104–109, 2017.

[123] M Thrall, R Freer, C Martin, F Azough, B Patterson, and R. Cernik, "An in situ study of the formation of multiferroic bismuth ferrite using high resolution synchrotron x-ray powder diffraction," *Journal of the European Ceramic Society*, vol. 28, no. 13, pp. 2567–2572, 2008.

[124] C. Xu, Y. Wang, Q. Wang, J. Li, and L. Yan, "Phase transformation and heterojunction nanostructures of bismuth iron oxide," *Journal of Materials Science: Materials in Electronics*, vol. 34, no. 35, p. 2236, 2023.

[125] S Vyazovkin and C. Wight, "Kinetics in solids," *Annual review of physical chemistry*, vol. 48, no. 1, pp. 125–149, 1997.

[126] A. Khawam and D. R. Flanagan, "Solid-state kinetic models: basics and mathematical fundamentals," *The journal of physical chemistry B*, vol. 110, no. 35, pp. 17 315–17 328, 2006.

[127] S. Vyazovkin and C. A. Wight, "Model-free and model-fitting approaches to kinetic analysis of isothermal and nonisothermal data," *Thermochimica acta*, vol. 340, pp. 53–68, 1999.

[128] N. Sbirrazzuoli, "Advanced isoconversional kinetic analysis: insight in mechanisms and simulations. successes and future," *Thermochimica Acta*, vol. 733, p. 179 688, 2024.

[129] A. Kirsch, M. M. Murshed, P. Gaczynski, K.-D. Becker, and T. M. Gesing, "Bi2fe4o9: structural changes from nano-to micro-crystalline state," *Zeitschrift für Naturforschung B*, vol. 71, no. 5, pp. 447–455, 2016.

[130] D. Zhou and D. J. Grant, "Model dependence of the activation energy derived from nonisothermal kinetic data," *The Journal of Physical Chemistry A*, vol. 108, no. 19, pp. 4239–4246, 2004.

[131] A. W. Coats and J. Redfern, "Kinetic parameters from thermogravimetric data," *Nature*, vol. 201, no. 4914, pp. 68–69, 1964.

[132] J. Zhou *et al.*, "Gelation chemistry and phase development of chemical solution deposition-derived sm-doped bifeo3 thin films: the role of sm dopant," *ACS Applied Electronic Materials*, vol. 5, no. 2, pp. 1302–1310, 2023.

[133] A. K. Jonscher, "Dielectric relaxation in solids," *Journal of Physics D: Applied Physics*, vol. 32, no. 14, R57, 1999.

[134] T.-F. Zhang *et al.*, "Oxygen-vacancy-related relaxation and conduction behavior in (pb1-xbax)(zr0. 95ti0. 05) o3 ceramics," *AIP Advances*, vol. 4, no. 10, 2014.

[135] Y. Zhou *et al.*, "Impedance behaviors of nd-doped bifeo3 ceramics with $0.10 \leq x \leq 0.30$," *Journal of Materials Science: Materials in Electronics*, vol. 33, no. 33, pp. 25 475–25 487, 2022.

[136] X. Xiao *et al.*, "Greatly reduced leakage current in bifeo3 thin film by oxygen ion implantation," *Journal of Physics D: Applied Physics*, vol. 40, no. 18, p. 5775, 2007.

[137] V. Palkar and R Pinto, "Bifeo 3 thin films: novel effects," *Pramana*, vol. 58, pp. 1003–1008, 2002.

[138] J. R. Macdonald and W. B. Johnson, "Fundamentals of impedance spectroscopy," *Impedance spectroscopy: theory, experiment, and applications*, pp. 1–20, 2018.

[139] B. Deka and S Ravi, "Study of impedance spectroscopy and electric modulus of pbti1–xfexo3 (x= 0.0–0.3) compounds," *Journal of Alloys and Compounds*, vol. 720, pp. 589–598, 2017.

[140] C. Carter, *Ceramic materials: science and engineering*, 2007.

[141] B. A. Gregg, *Excitonic solar cells*, 2003.

[142] M.-M. Yang, A. Bhatnagar, Z.-D. Luo, and M. Alexe, "Enhancement of local photovoltaic current at ferroelectric domain walls in bifeo3," *Scientific Reports*, vol. 7, no. 1, p. 43 070, 2017.

[143] S. D. Ganichev and W. Prettl, "Spin photocurrents in quantum wells," *Journal of physics: Condensed matter*, vol. 15, no. 20, R935, 2003.

[144] S. Basu *et al.*, "Photoconductivity in bifeo3 thin films," *Applied Physics Letters*, vol. 92, no. 9, 2008.

Appendix A

Raman spectroscopy's attachments

Table A.1: Parameters of Raman spectra fits in samples BFO-620 and BFO-640. The parameters in red indicate that it was not possible to estimate the values.

Sample	Peak	X-center	FHWM	Area	Height
BFO-640	1	< 100	-	-	-
	2	**141.50**	29.50	264865.99	5715.96
	3	**173.89**	15.39	67259.53	2782.14
	4	**231.09**	42.08	45272.07	684.84
	5	**271.97**	37.72	57782.00	975.06
	6	**300.26**	28.62	45465.74	1011.16
	7	**344.70**	51.88	71602.15	878.55
	8	**372.18**	15.50	8693.41	357.07
	9	**420.66**	59.57	44863.53	479.47
	10	**472.86**	26.94	11798.90	278.85
	11	**527.57**	70.65	51026.07	459.78
	12	**570.62**	3.21	1151.27	228.31
BFO-620	1	**102.40**	80.54	513206.91	4056.68
	2	**141.56**	31.75	246038.68	4933.36
	3	**173.53**	12.80	45954.12	2285.50
	4	**226.55**	113.17	178136.40	1002.03
	5	**260.69**	56.10	71216.39	808.14
	6	**304.71**	95.02	135865.60	910.27
	7	**347.93**	29.37	23562.13	510.81
	8	**374.07**	7.95	4811.25	385.24
	9	**420.35**	68.93	65607.36	605.96
	10	**468.18**	8.61	2258.54	166.89
	11	**520.33**	65.21	42852.78	418.35
	12	**566.38**	2.04	483.76	151.16

Table A.2: Parameters of Raman spectra fits in samples BFO-500, BFO-580 and BFO-600. The parameters in red indicate that it was not possible to estimate the values.

Sample	Peak	X-center	FHWM	Area	Height
BFO-600	1	< 100	-	-	-
	2	**142.44**	36.92	141623.71	2614.73
	3	**174.75**	19.66	39701.66	1285.34
	4	**223.87**	78.43	133709.55	1085.37
	5	**265.00**	40.85	36807.44	573.55
	6	**302.78**	61.35	99821.27	1035.87
	7	**340.00**	18.29	9825.71	341.92
	8	**362.57**	42.02	33906.73	513.71
	9	**418.00**	82.20	108892.05	843.34
	10	**438.00**	6.47	449.45	44.21
	11	**518.19**	52.99	38569.36	463.34
	12	**574.65**	26.23	5296.75	128.54
BFO-580	**1**	< 100	-	-	-
	2	**141.98**	32.36	160346.95	3154.53
	3	**172.66**	15.27	35583.89	1483.62
	4	**229.04**	84.53	54662.08	411.69
	5	**269.51**	84.53	54662.08	411.69
	6	**301.62**	34.37	29565.38	545.75
	7	**340.40**	29.81	19918.97	425.36
	8	**371.09**	19.32	8066.45	265.80
	9	**421.82**	94.14	51521.83	348.40
	10	**474.49**	30.79	8539.58	176.57
	11	**521.45**	53.43	33196.32	395.50
	12	**595.98**	3.50	1466.10	266.42
BFO-500	**None**	-	-	-	-

Appendix B

SEM's attachments

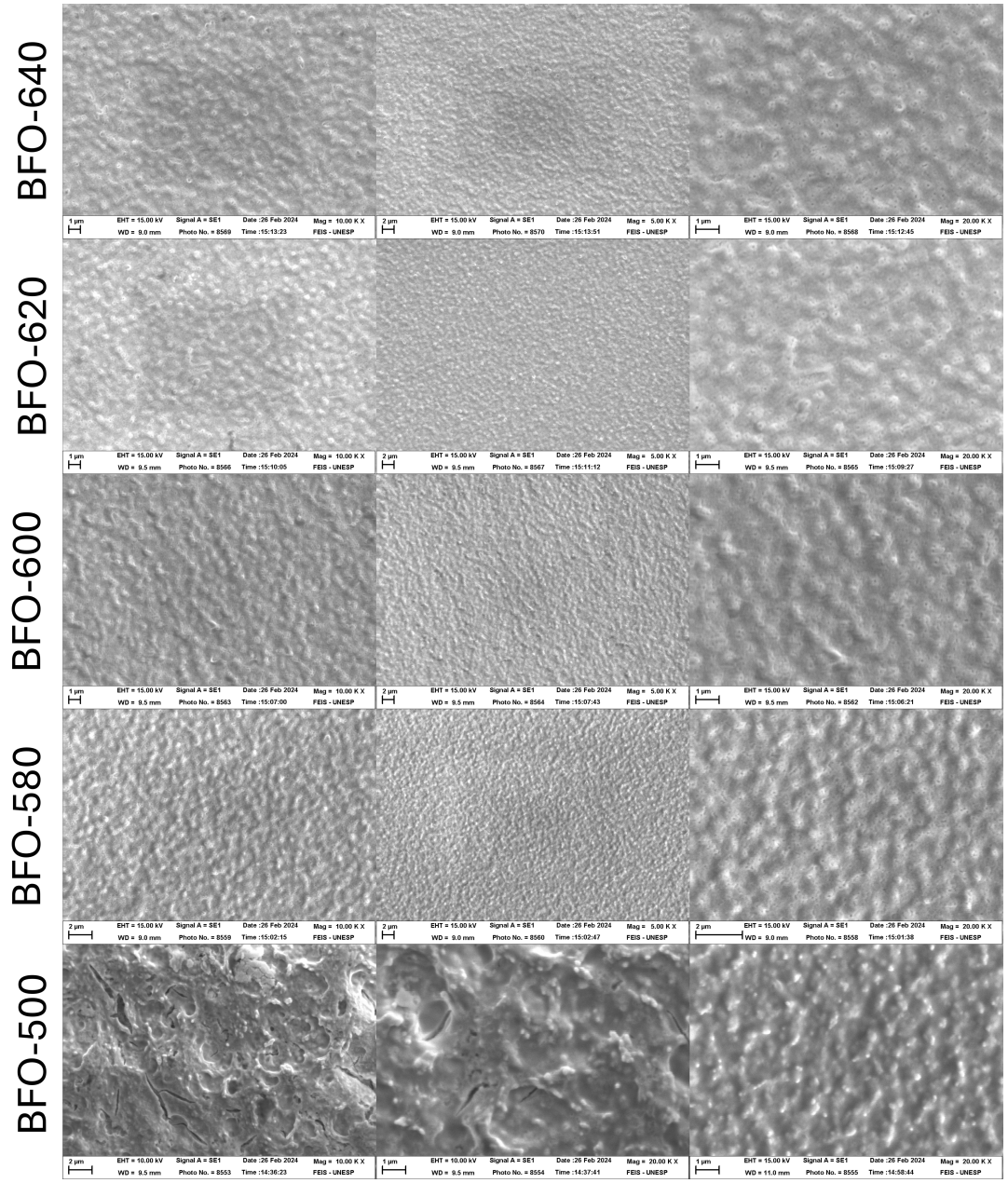

Figure B.1: Microscopic images of samples in three different regions.

Kinetic reaction studies' attachments

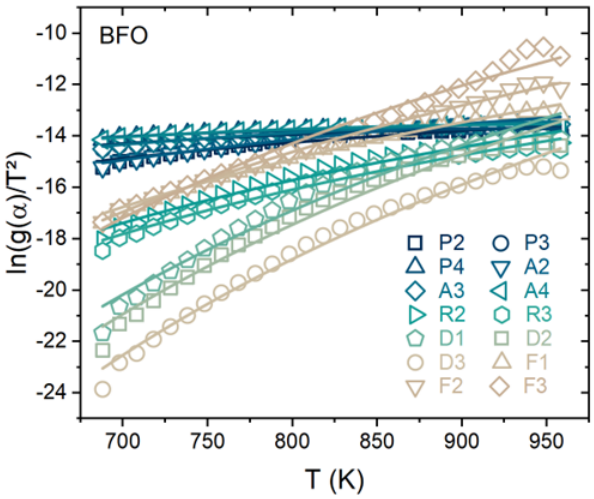

Figure C.1: Experimental data converted to $\ln[g(\alpha)/T^2]$ using each of the models shown in Table 3.5 and respective fits with the Coats-Redfern approximation.

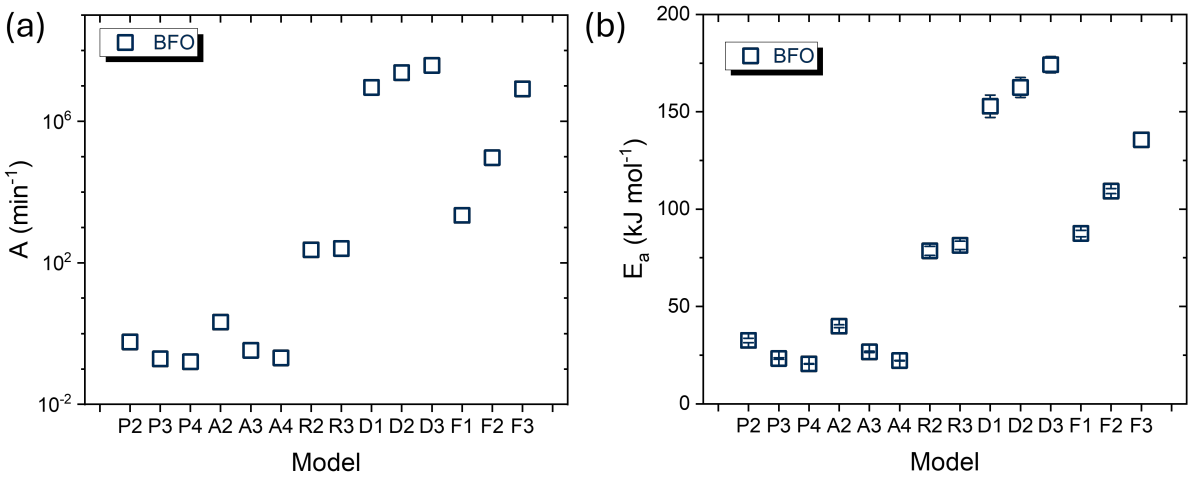

Figure C.2: (a): Pre-exponential constant and (b): activation energies obtained with each kinetic model for the studied BFO thin films. Error bars are the fit residuals.

Appendix D

Impedance Spectroscopy's attachments

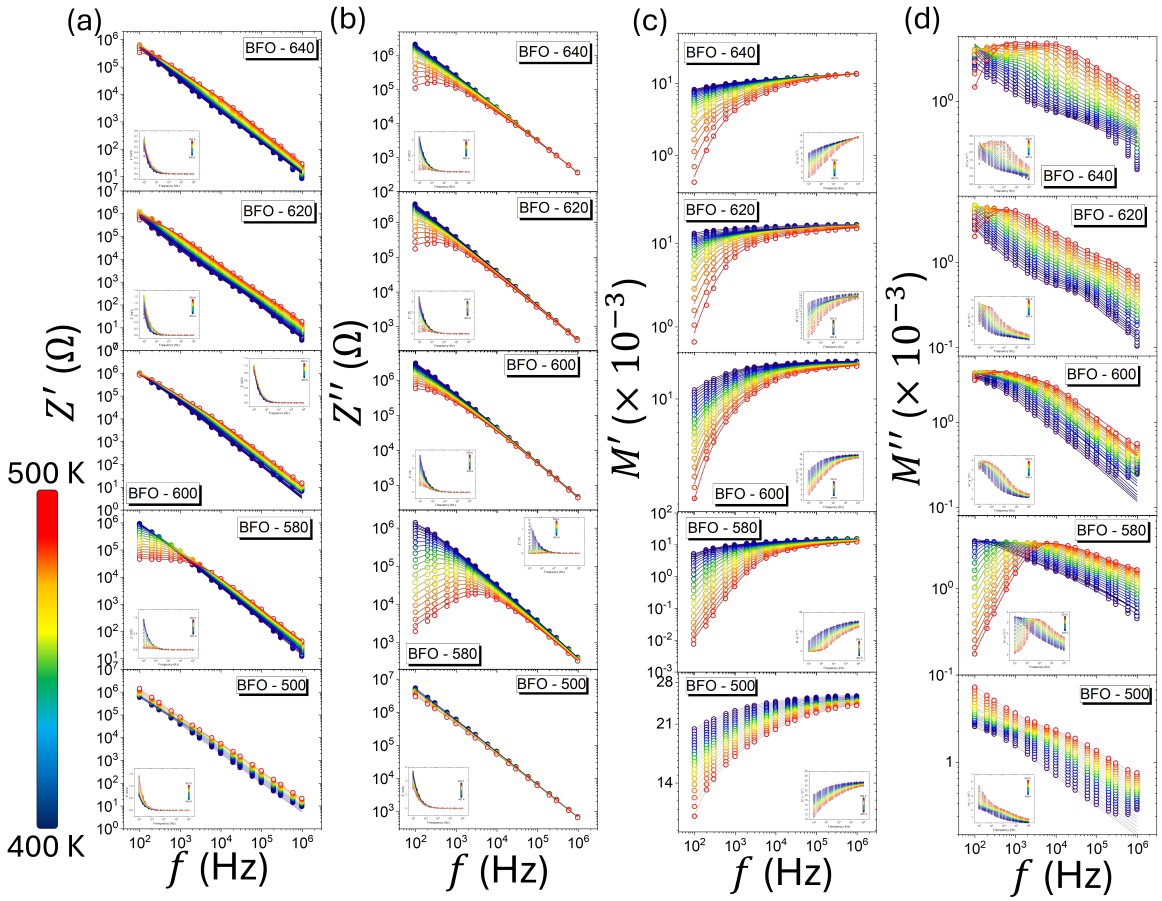

Figure D.1: Spectra adjustment of (a) real and (b) imaginary electric impedance (Z' and Z'', respectively), and (c) real and (d) imaginary electric modulus (M' and M'', respectively). The open symbols are the experimental data and the solid lines are the adjustments.

Table D.1: Impedance spectroscopy parameters of BFO-500.

T (K)	A (nSHz^{-n})	n	R_{gb} (GΩ)	C_{gb} (nF)	R_g (kΩ)	f_g (kHz)
400	4.16	0.71	1.14	2.37	31.64	0.49
405	4.40	0.71	1.14	2.38	31.13	0.50
410	4.91	0.70	1.12	2.38	21.05	0.65
415	5.31	0.70	1.11	2.38	16.17	0.79
420	5.69	0.71	1.09	2.38	12.11	0.99
425	6.01	0.71	1.07	2.38	9.67	1.17
430	6.44	0.71	1.05	2.38	6.96	1.44
435	7.01	0.71	1.02	2.37	4.95	1.84
440	7.39	0.71	0.99	2.38	3.92	2.46
445	7.94	0.71	0.97	2.38	3.38	3.12
450	8.14	0.71	0.96	2.39	3.02	3.66
455	8.67	0.71	0.65	2.39	2.51	4.31
460	9.12	0.71	0.51	2.39	2.12	4.97
465	9.85	0.71	0.44	2.39	1.78	5.81
470	10.2	0.72	0.12	2.39	1.50	6.81
475	10.9	0.72	0.10	2.39	1.20	8.35
480	11.2	0.72	0.05	2.39	1.03	9.86
485	11.9	0.72	0.04	2.39	0.79	12.30
490	12.4	0.72	0.02	2.39	0.64	14.37
495	12.9	0.72	0.02	2.38	0.51	16.10
500	12.0	0.74	0.01	2.36	0.49	16.70

Table D.2: Impedance spectroscopy parameters of BFO-580.

T (K)	A (nSHz^{-n})	n	R_{gb} (MΩ)	C_{gb} (nF)	R_g (kΩ)	f_g (kHz)
400	3.88	0.68	4.78	0.37	10.80	0.22
405	3.53	0.70	3.85	0.36	9.78	0.27
410	4.28	0.70	3.48	0.37	9.30	0.31
415	4.70	0.68	3.11	0.37	6.79	0.40
420	4.80	0.69	2.47	0.37	4.55	0.65
425	5.01	0.69	1.97	0.37	2.95	1.02
430	5.23	0.69	1.57	0.37	2.38	1.47
435	5.45	0.70	1.21	0.37	2.18	2.14
440	5.68	0.70	0.94	0.37	1.97	2.92
445	5.92	0.71	0.72	0.37	1.66	4.05
450	6.12	0.71	0.55	0.36	1.46	5.67
455	6.31	0.72	0.44	0.36	1.33	7.41
460	6.62	0.72	0.31	0.36	1.12	9.73
465	7.03	0.72	0.24	0.36	0.88	12.97
470	7.37	0.73	0.18	0.36	0.71	17.32
475	7.56	0.73	0.14	0.35	0.64	21.40
480	7.76	0.74	0.11	0.35	0.57	25.88
485	8.11	0.74	0.09	0.35	0.49	31.01
490	8.67	0.74	0.07	0.35	0.37	39.09
495	9.05	0.74	0.06	0.35	0.30	48.66
500	9.09	0.75	0.05	0.34	0.27	56.61

Table D.3: Impedance spectroscopy parameters of BFO-600.

T (K)	A (nSHz^{-n})	n	R_{gb} (MΩ)	C_{gb} (nF)	R_g (kΩ)	f_g (kHz)
400	2.81	0.58	75.6	0.34	34.67	0.37
405	3.23	0.57	73.6	0.34	30.08	0.41
410	3.55	0.57	64.3	0.34	21.99	0.55
415	3.99	0.56	61.2	0.35	18.97	0.60
420	4.25	0.57	45.4	0.35	16.12	0.74
425	4.26	0.58	35.1	0.35	15.51	0.83
430	4.83	0.57	28.1	0.35	13.77	0.96
435	5.16	0.57	22.7	0.35	12.38	1.13
440	5.50	0.57	19.1	0.35	11.16	1.32
445	5.74	0.58	17.2	0.35	10.12	1.55
450	6.89	0.57	16.2	0.36	9.19	1.82
455	6.14	0.58	10.2	0.36	6.13	3.04
460	6.59	0.58	7.73	0.36	5.65	3.51
465	6.28	0.59	5.79	0.36	5.21	3.98
470	6.85	0.59	5.05	0.36	4.79	4.51
475	7.43	0.59	4.53	0.36	4.41	5.06
480	6.22	0.62	3.14	0.36	4.36	5.16
485	7.98	0.60	2.90	0.36	3.82	5.39
490	8.49	0.60	2.72	0.36	3.67	6.03
495	11.7	0.58	2.51	0.37	3.26	6.81
500	8.46	0.62	1.69	0.36	3.19	7.01

Table D.4: Impedance spectroscopy parameters of BFO-620.

T (K)	A (nSHz^{-n})	n	R_{gb} (MΩ)	C_{gb} (nF)	R_g (Ω)	f_g (kHz)
400	0.638	0.70	37.00	0.36	210.87	29.68
405	0.750	0.70	32.60	0.37	200.68	31.19
410	0.905	0.69	26.60	0.38	185.50	33.54
415	1.02	0.68	22.70	0.38	168.46	36.42
420	1.13	0.68	19.80	0.39	151.81	39.83
425	1.23	0.68	17.00	0.39	135.12	43.29
430	1.29	0.69	14.50	0.38	116.92	46.57
435	1.36	0.69	12.30	0.38	99.24	49.63
440	1.46	0.69	10.40	0.38	84.20	52.22
445	1.55	0.69	8.90	0.38	71.29	53.69
450	1.67	0.69	7.90	0.37	59.75	63.49
455	1.81	0.69	6.25	0.37	49.51	73.41
460	2.08	0.69	5.25	0.37	42.89	86.14
465	2.48	0.68	4.40	0.36	40.40	108.20
470	3.03	0.66	3.74	0.36	35.03	140.45
475	3.56	0.65	3.30	0.36	32.02	185.80
480	4.59	0.64	2.62	0.37	30.68	246.14
485	5.32	0.63	2.03	0.37	30.44	298.20
490	5.65	0.64	1.43	0.38	30.16	305.65
495	6.08	0.65	1.03	0.38	29.95	309.50
500	6.64	0.65	0.75	0.38	28.96	316.88

Table D.5: Impedance spectroscopy parameters of BFO-640.

T (K)	A (nSHz^{-n})	n	R_{gb} (MΩ)	C_{gb} (nF)	R_g (kΩ)	f_g (kHz)
400	1.05	0.81	30.10	0.41	44.71	0.22
405	1.05	0.82	21.40	0.40	34.26	0.31
410	1.07	0.82	16.70	0.40	28.80	0.39
415	1.10	0.82	13.80	0.40	24.64	0.50
420	1.15	0.82	11.80	0.40	21.31	0.63
425	1.21	0.82	10.30	0.40	19.08	0.78
430	1.32	0.81	9.40	0.40	17.78	0.91
435	1.45	0.81	8.20	0.40	16.99	1.04
440	1.64	0.80	7.61	0.40	16.38	1.16
445	1.92	0.79	7.00	0.40	15.76	1.29
450	2.25	0.78	6.46	0.41	15.08	1.42
455	2.72	0.76	5.92	0.41	14.16	1.58
460	3.24	0.75	5.34	0.41	13.01	1.78
465	3.96	0.74	4.56	0.41	11.68	2.03
470	4.58	0.73	3.44	0.41	8.96	2.77
475	5.69	0.72	2.24	0.41	6.66	3.87
480	6.62	0.71	1.99	0.41	5.37	4.97
485	6.86	0.71	1.31	0.40	4.22	6.48
490	7.62	0.71	0.96	0.40	3.22	8.75
495	8.64	0.70	0.68	0.40	2.63	11.00
500	8.52	0.72	0.45	0.39	2.24	12.88

Appendix E

J-E studies' attachments

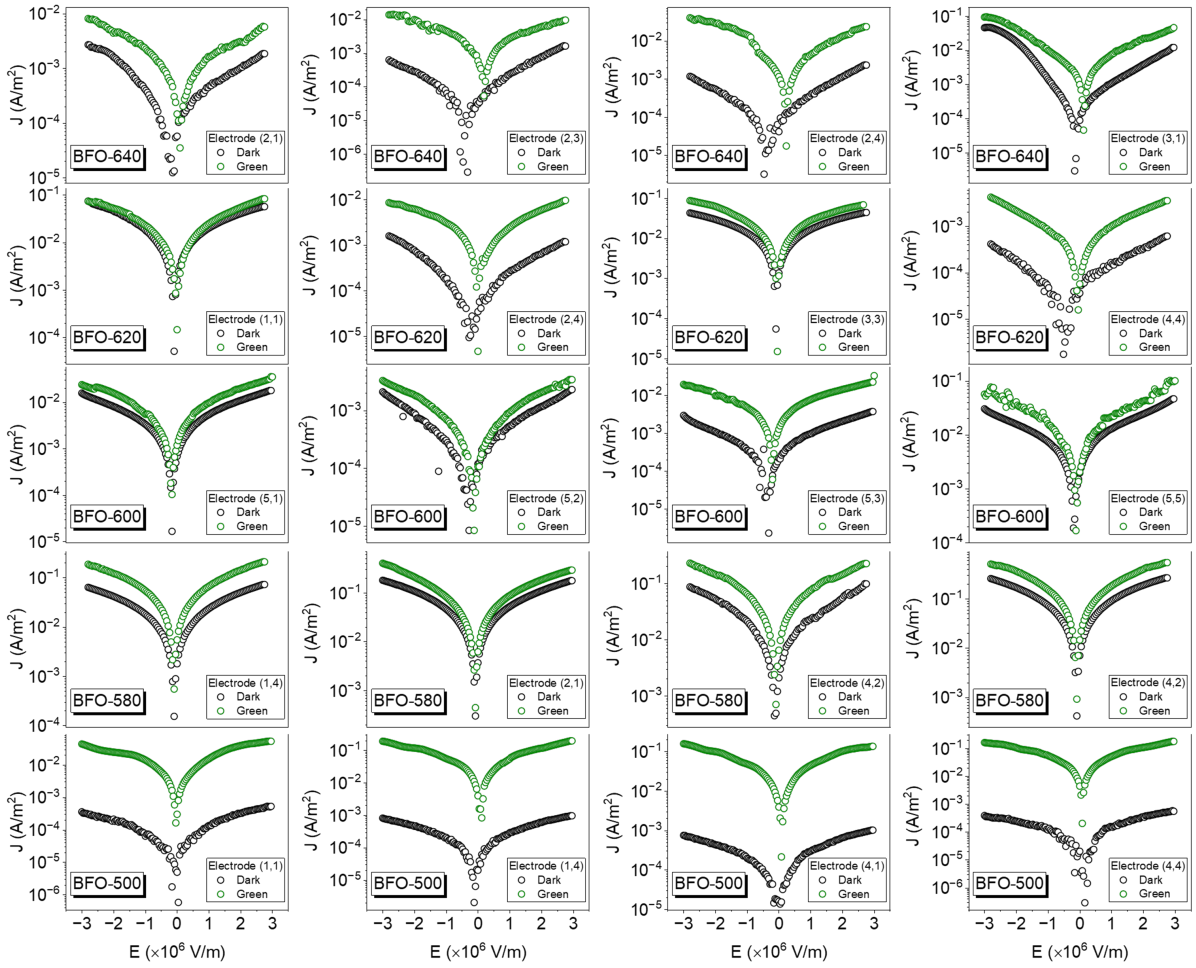

Figure E.1: Hysteresis loops J-E of samples.

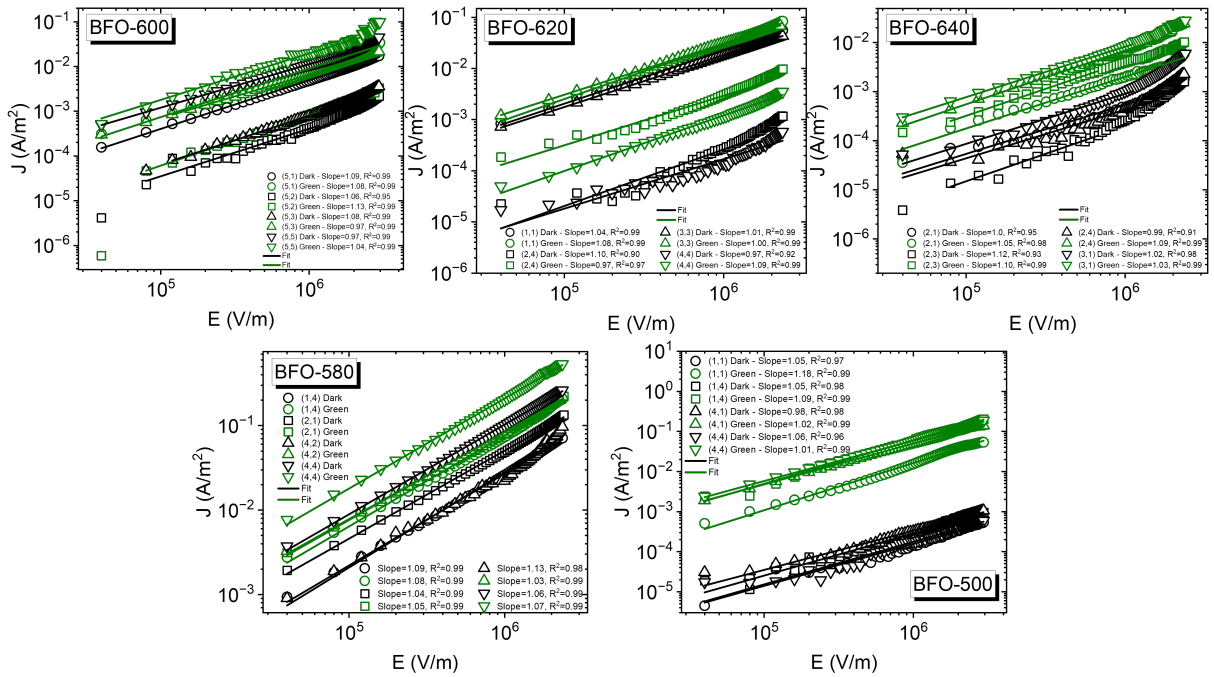

Figure E.2: Log-log plot of the positive branch of hysteresis cycles, jointly the linear fit to confirm the conduction mechanism. Color black represent the dark condition, and green color represent the condition under the green light measurements.

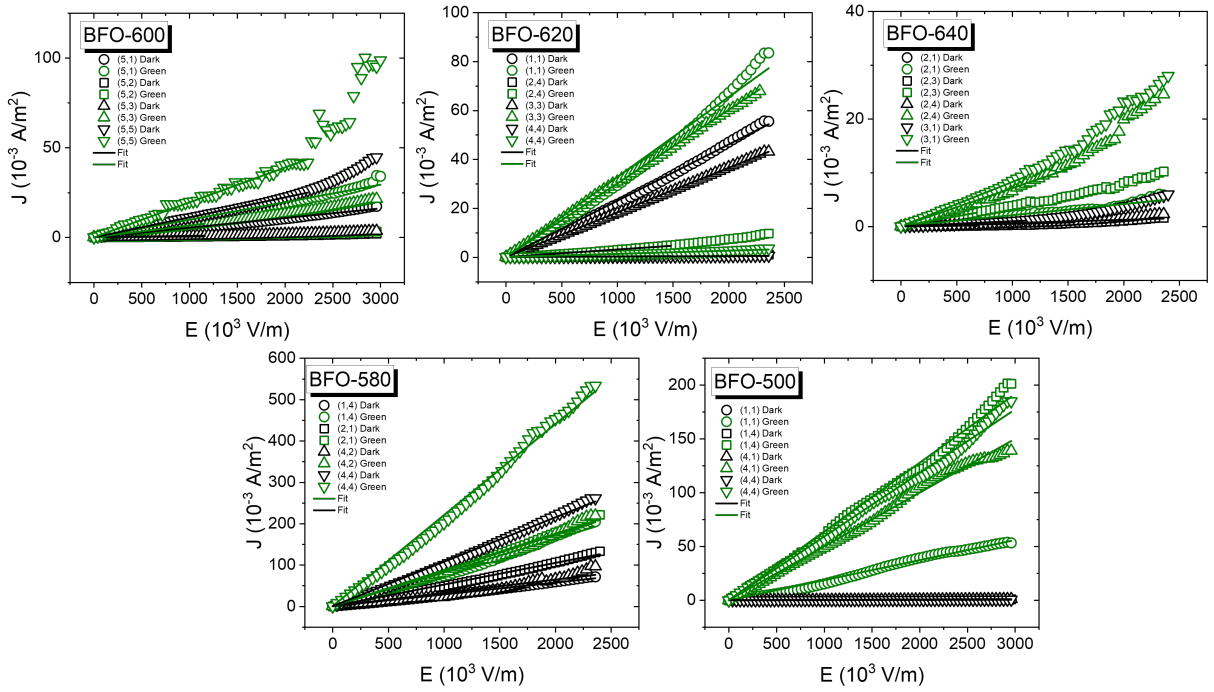

Figure E.3: Straight-line fit of curves in linear plot.

Table E.1: Values of the leakage current (J) at the maximum applied electric field and the estimated conductivity (σ) in the Ohmic region for each electrode. "Elec." is the abbreviation for electrode; thus, the numbers in parentheses indicate the locator vector of the electrode, as demonstrated in Figure 2.4. The term "T" represents the crystallization temperature of the samples.

T (°C)	Elec.	J_{dark} ($\times 10^{-3}$A/m^2)	J_{green} ($\times 10^{-3}$A/m^2)	σ_{dark} ($\times 10^{-9}$S/m)	σ_{green} ($\times 10^{-9}$S/m)
640	(2,1)	1.79	5.84	0.61	2.07
	(2,3)	1.60	10.23	0.19	3.73
	(2,4)	2.27	24.54	0.48	7.11
	(3,1)	5.95	28.00	0.95	8.26
620	(1,1)	55.54	83.57	23.02	32.70
	(2,4)	1.17	9.70	0.29	3.09
	(3,3)	43.10	67.89	18.25	30.11
	(4,4)	0.58	3.5	0.19	1.31
600	(5,1)	17.27	34.02	5.36	9.78
	(5,2)	2.18	3.31	0.41	0.80
	(5,3)	3.56	21.39	0.77	6.55
	(5,5)	44.66	98.71	11.12	19.45
580	(1,4)	71.03	204.35	28.60	81.50
	(2,1)	133.42	221.64	52.40	87.70
	(4,2)	96.17	218.08	32.20	86.20
	(4,4)	261.05	533.37	107.40	220.00

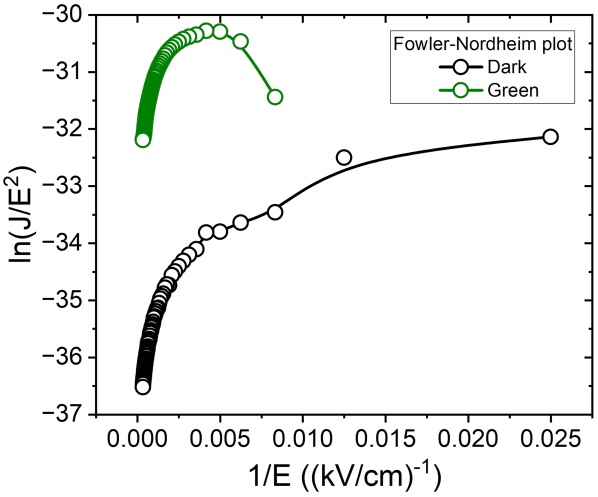

Figure E.4: Fowler-Nordheim plot of the representative electrode of sample BFO-500. The solid lines are guides for the eyes.

Appendix F

PFM's attachments

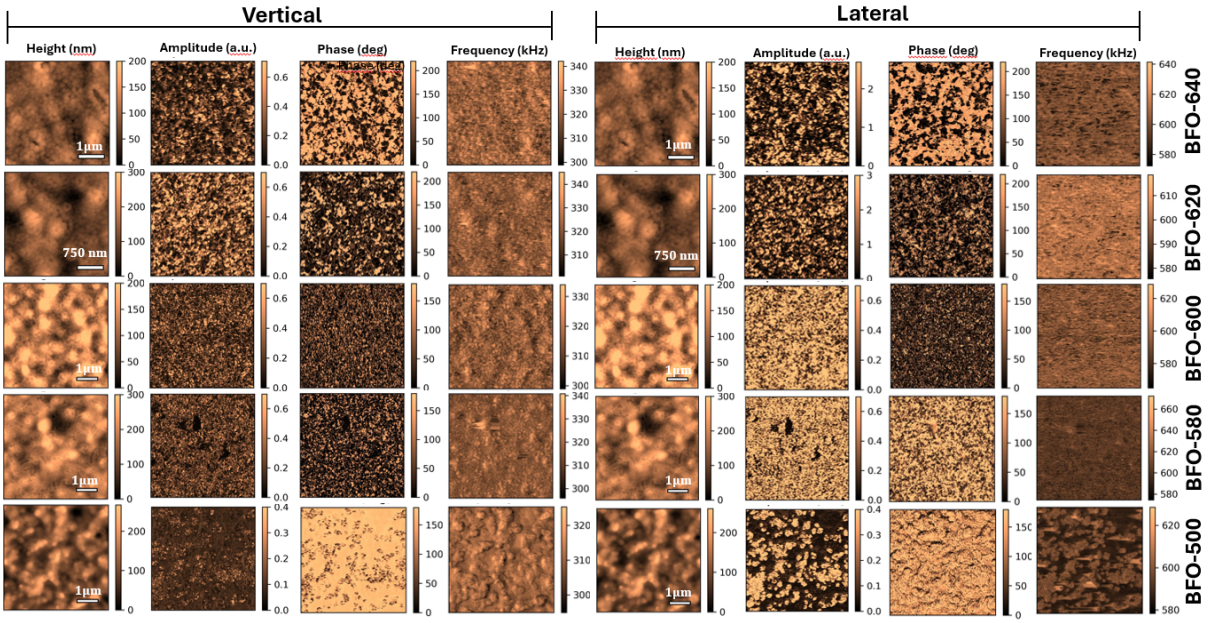

Figure F.1: Topography of samples collected through PFM technique.